Influence of wind conditions on wind turbine loads and measurement of turbulence using lidars

Ameya R. Sathe

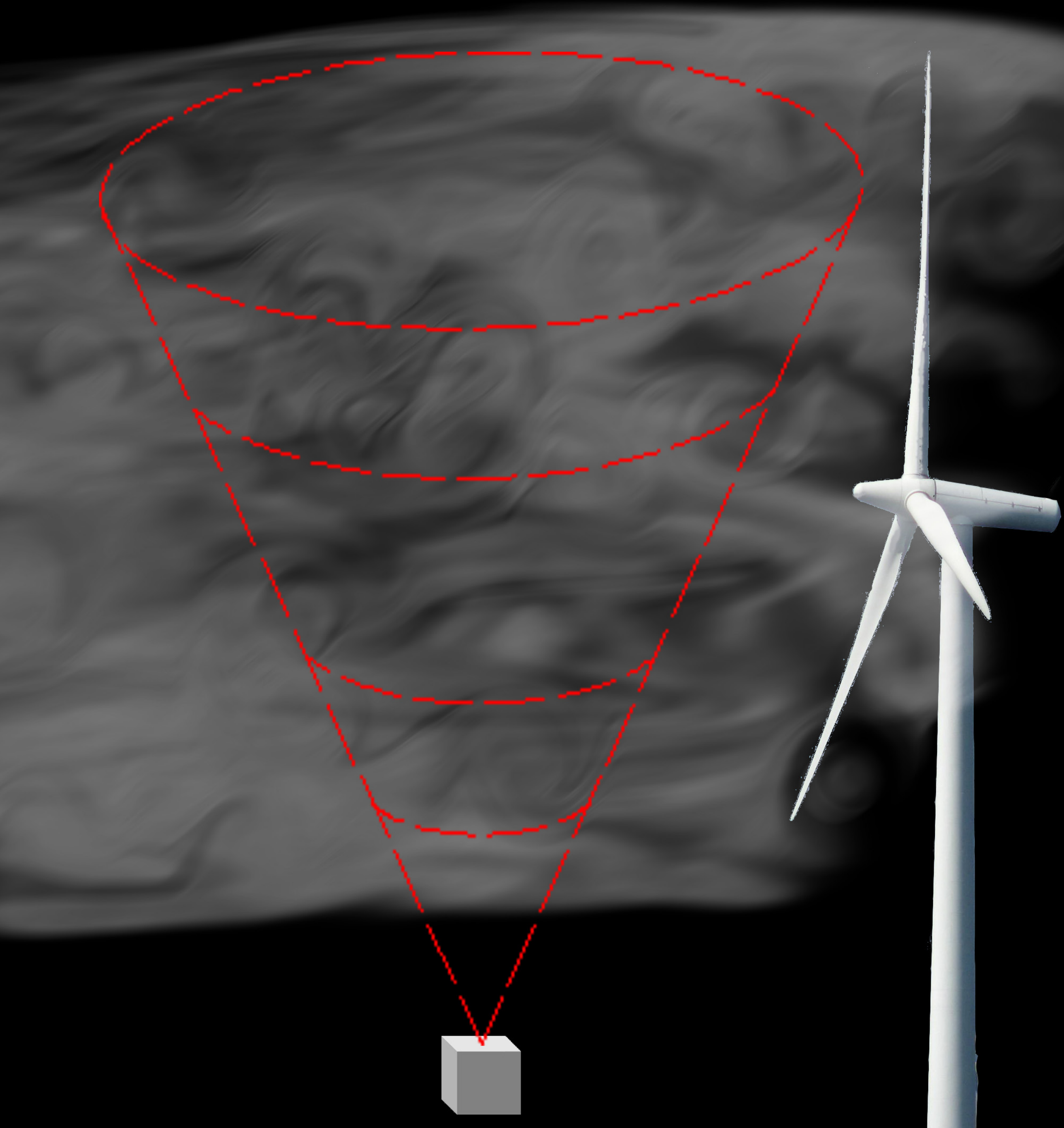

Influence of wind conditions on wind turbine loads and measurement of turbulence using lidars

Influence of wind conditions on wind turbine loads and measurement of turbulence using lidars

PROEFSCHRIFT

ter verkrijging van de graad van doctor
aan de Technische Universiteit Delft,
op gezag van de Rector Magnificus prof. ir. K.C.A.M. Luyben,
voorzitter van het College voor Promoties,
in het openbaar te verdedigen
op vrijdag 2 maart 2012 om 12.30 uur
door

Ameya Rajiv SATHE

Master of Technology in Hydrology, Indian Institute of Technology
Roorkee, India
geboren te Mumbai, India

Dit proefschrift is goedgekeurd door de promotoren:

Prof. dr. G.J.W. van Bussel
Prof. dr. J. Mann

Copromotor Dr. ir. W.A.A.M. Bierbooms

Samenstelling promotiecommissie:

Rector Magnificus	voorzitter
Prof. dr. G.J.W van Bussel	Technische Universiteit Delft, promotor
Prof. dr. J. Mann	Technical University of Denmark, promotor
Dr. ir. W.A.A.M. Bierbooms	Technische Universiteit Delft, copromotor
Prof. dr. H. Russchenberg	Technische Universiteit Delft
Prof. dr. A.A.M. Holtslag	Wageningen Universiteit
Dr. D. Lenschow	National Center for Atmospheric Research, USA
Dr. J. Højstrup	Romowind Denmark
Prof. dr. D.G. Simons	Technische Universiteit Delft, reservelid

The research described in this thesis forms part of the project PhD@SEA which is substantially funded under the BSIK-programme (BSIK03041) of the Dutch Government and supported by the consortium WE@SEA

Published and distributed by:
DUWIND Delft University Wind Energy Research Institute
ISBN 978-90-76468-00-6
Printed by Wöhrmann Print Service, Zutphen, The Netherlands

Typeset by the author with the LaTeX Documentation System.
Author email: `amsat@dtu.dk`

Dedicated to my mother, my wife, my brother and late maternal grandfather

Acknowledgements

So many people have contributed directly or indirectly to the completion of this PhD thesis that if I write in detail the contribution of everyone then this in itself would be an autobiography. Nevertheless I would like to mention as many as possible.

First and foremost I thank my supervisor from Risø DTU, Jakob Mann, for his sustained high quality guidance. I don't know why but I have always believed that a student is only as good as his teacher. It could perhaps be because of one wonderful learning experience that I have had with a teacher during my Bachelor studies. After having a great learning experience with Jakob, my belief has just grown stronger. Without his sustained guidance and support I could not have finished my PhD. It is evident from the fact that I wrote three journal articles and one conference paper with him. I also thank him for introducing me to the fascinating world of turbulence.

Delft University is where it all began for me. Hadn't it been for the opportunities provided by my supervisors Wim Bierbooms and Gerard van Bussel from Delft, I could not have established strong ties with Risø DTU. I thank Wim and Gerard for the sustained moral support that they have provided me throughout my PhD. I also thank Wim for his efforts in supervising me during the initial phase of my PhD. In the midst of my PhD I got interested in lidar turbulence research, and it meant that the original goals of my PhD had to be modified considerably. Therefore I express my gratitude towards Wim and Gerard for giving me immense freedom and letting me pursue my field of interest.

In Indian culture we are not accustomed to saying 'Thank you' to family members, since it makes us feel that we are not close to each other. Hence, I will not use this word in acknowledging my family. My mother has been a tremendous source of inspiration whenever I felt that I was wavering in my goals. The values that she has instilled in me since my childhood has certainly helped me to finish my PhD. The struggles that she has experienced in her life, but the ease with which she has raised us, has always made me feel that the problems in my PhD were minuscule, and gave me a lot of strength. My wife has been a tremendous source of support for me in the last two years. The care and love with which she has emotionally supported me has helped me immensely to finish my PhD. My late maternal grandfather has been an embodiment of discipline. On many occasions when the task demanded discipline I drew inspiration from him. He still inspires me in my life. I value my brother's contribution because he took care of my mother and maternal grandfather during the entire duration of my PhD. On many occasions when help was needed in the family he was always there. At times he has sacrificed his own ambitions for the sake of the family, and that has directly helped me to focus on my PhD.

Out of the five years I worked on my PhD, I spent about 1.5 years at Risø DTU. I had never imagined that my experience at Risø would be so rewarding. At first I would like to thank Sven-Erik Gryning and Alfredo Peña for guiding me in atmospheric stability and wind profile analysis. Working with them was the beginning of my wonderful learning experiences at Risø. I am grateful to Alfredo for virtually giving me a private scientific writing course. I could myself notice a step change in the quality of my scientific writing skills after having written the first article with him and Sven-Erik. I thank Mike Courtney for giving me opportunity to work in two interesting and challenging projects, ‘Upwind’ and ‘Safewind’. The constant support and encouragement that Mike gave me in the last year is highly appreciated. Sharing the office space with him and Rozenn Wagner at Risø was a fun-filled experience. I also thank Abhijit Chougule, who incidentally is a PhD student of Jakob at Risø, for having interesting discussions on the fascinating topic of turbulence. We exchanged several ideas and continue learning from each other. I thank Torben Larsen for helping me get acquainted with the turbulence input in HAWC2. I thank Gunner Larsen for having interesting discussions on the load calculations. For my stay at Roskilde, I thank Claus and Lis Jensen, Marete and Finn Hansen, Kjeld Christiansen and Lizzie Kummel, and Eva and Peter Jensen. I highly appreciate the warmth and affection that they have given me and my wife. Because of them we hardly felt that we were thousands of kilometers away from our home in India. Particularly the support that Claus and Lis has given us is simply unforgettable.

In my times at Delft, I have had many wonderful moments. At first I would like to thank Thanasis Barlas, Busra Akay and Jaume Betran for making my time in Delft memorable. The wonderful dinners and the philosophical discussions that we had together are now etched in my memories. I thank Thanasis also for helping me with understanding the structure of the aero-elastic simulation tool HAWC2. I thank Eeke Mast for the nice time I had while sharing the office with her, where I have also had many interesting discussions about life in general. I thank Thanasis, Eeke and Frans, Claudia and Bertin, and Jaume and Joanna for coming all the way to India to attend my wedding. The wonderful memories during my wedding will always stay with me. For Matlab doubts in the initial period of my PhD I express my thanks to Carlos Ferreira, who suggested me some simple and elegant techniques of data processing. Dick Veldkamp helped me in the load calculations, particularly in getting familiarized with the aero-elastic simulation tool Flex5. Rarely I have come across people who are so honest and sincere in helping others, and Dick is one amongst them. Eventually I did not use Flex5 in my thesis, but I would like to extend my heartfelt gratitude to Dick for all the help that he provided me. I thank my ex-Master student Andrea Venora for performing a nice job in his thesis. His thirst for knowledge and aptitude for fine details always kept me on my toes in my work, when I was supervising his thesis. With Gijs van Kuik I had some nice philosophical discussions, and I thank him for that. I feel calm and happy simply by talking to him. Amongst others in the wind energy section I also thank Turaj Ashuri, Teodor Chiciudean, Ben Geurts and Erika Echavarria for the fun times in Delft. Last but certainly not the least I thank Sunil and Shweta Kulkarni for the wonderful and memorable times in Amsterdam. They are one of the friends who I can count on during tough times.

The PhD project has been carried out under the We@Sea program, BISK-03041, and sponsored by the Dutch Ministry of Economic affairs. The data from the Offshore Wind farm Egmond aan Zee (OWEZ) were kindly made available by NoordZeewind under the Research Program WE@Sea. The data from Horns Rev were kindly provided by Vattenfall A/S and DONG energy A/S as part of the 'Tall Wind' project, which is funded by the Danish Research Agency, the Strategic Research Council, Program for Energy and Environment (Sagsnr. 2104-08-0025). Funding from the EU project, contract TREN-FP7EN-219048 'NORSEWinD' is acknowledged. The resources provided by the EU FP6 UpWind project (Project reference 019945 SES6) and by the Center for computational wind turbine aerodynamics and atmospheric turbulence funded by the Danish Council for Strategic Research grant no. 09-067216 is highly appreciated.

Summary

Variations in wind conditions influence the loads on wind turbines significantly. In order to determine these loads it is important that the external conditions are well understood. Wind lidars are well developed nowadays to measure wind profiles upwards from the surface. But how turbulence can be measured using lidars has not yet been investigated. This PhD thesis deals with the influence of variations in wind conditions on the wind turbine loads as well as with the determination of wind conditions using wind lidars.

Part I of the thesis focuses on analysis of diabatic wind profiles, turbulence, and their influence on wind turbine loads. The diabatic wind profiles are analyzed using the measurements from two offshore sites, one in the Dutch North Sea, and the other in the Danish North Sea. Two wind profile models are compared, one that is strictly valid in the atmospheric surface layer, and the other that is valid for the entire boundary layer. The second model is much more complicated in comparison to the first. It is demonstrated that at heights more than 50 m above the surface, where modern wind turbines usually operate, it is advisable to use a wind profile model that is valid in the entire boundary layer. The influence of diabatic wind profiles under steady winds on the fatigue damage at the blade root is also demonstrated using the aero-elastic simulation tool Bladed. Furthermore, detailed analysis of the combined influence of diabatic wind profile and turbulence on the blade root flap-wise and edge-wise moments, tower base fore-aft moment, and the rotor bending moments at the hub is carried out using the aero-elastic simulation tool HAWC2. It is found that the tower base fore-aft moment is influenced by diabatic turbulence and a rotor bending moment at the hub is influenced by diabatic wind profiles. The blade root loads are influenced by diabatic wind profiles and turbulence, which results in averaging of the loads, i.e. the calculated blade loads using diabatic wind conditions and those calculated using neutral wind conditions are approximately the same. The importance of obtaining a site-specific wind speed and stability distribution is also emphasized since it has a direct influence on wind turbine loads. In comparison with the IEC standards, which generalize the wind conditions according to certain classes of wind speeds, the site-specific wind conditions are demonstrated to give significantly lower fatigue loads. There is thus a potential in reducing wind turbine costs if site-specific wind conditions are obtained. In this regard we then are faced with measurement challenges.

The current industry standard for the measurement of wind speed is either the cup or the sonic anemometer. Both instruments require a meteorological mast to be

mounted at the measurement site. For measuring the wind profile the instruments need to be mounted at several heights on the mast. To install a mast and set up these instruments is quite expensive, especially at offshore sites, where the cost of foundation increases significantly. Besides, there are problems with the flow distortion that have to be taken care of. In order to overcome these problems it would be ideal to have a remote sensing instrument that measures wind speed. Wind lidars are capable of doing that albeit with a price.

Part II of the thesis deals with detailed investigations of the ability of wind lidars to perform turulence measurements. Modelling of the systematic errors in turbulence measurements is carried out using basic principles. Two mechanisms are identified that cause these systematic errors. One is the averaging effect due to the large sample volume in which lidars measure wind speeds, and the other is the contribution of all components of the Reynolds stress tensor. Modelling of turbulence spectra as measured by a scanning pulsed wind lidar is also carried out. We now understand in detail the distribution of turbulent energy at various wavenumbers, when a pulsed wind lidar measures turbulence. The lidar turbulence models have been verified with the measurements at different heights and under different atmospheric stabilities. Finally, a new method is investigated that in principle makes turbulence measurements by lidars possible. The so-called six beam method uses six lidar beams to avoid the contamination by all components of the Reynolds stress tensor. The theoretical calculations carried out demonstrates the potential of this method. In order to avoid averaging due to volume sampling, a different analysis method is required, which has not been investigated in this thesis.

To summarize the entire thesis, it can be said that more work is required to ascertain the influence of atmospheric stability on wind turbine loads. In particular, comparing with the load measurements will go a long way in consolidating the understanding gained from the analysis in this thesis. If lidars are able to measure turbulence, there is a tremendous potential for performing site-specific wind turbine design and making the class based design of the IEC standards obsolete.

Samenvatting

Variaties in windcondities hebben een belangrijke invloed op de belastingen van windturbines. Om deze belastingen nauwkeurig te kunnen bepalen is het van belang dat de externe wind condities goed bekend zijn. Wind lidars zijn zeer geschikt om vanaf het oppervlak wind profielen te meten. Maar hoe turbulentie gemeten kan worden met behulp van wind lidars was nog niet onderzocht. Dit proefschrift behandelt zowel de invloed van variaties in windcondities op de belastingen van windturbines alsmede het meten van windcondities met behulp van wind lidars.

Deel I van dit proefschrift concentreert zich op de structuur en de turbulentie van diabatische windprofielen en hun invloed op windturbine belastingen. De diabatische windprofielen zijn bepaald aan de hand van metingen op twee locaties buitengaats, een in de Nederlandse Noordzee en de andere in de Deense Noordzee. Twee analytische modellen voor het windprofiel zijn met elkaar vergeleken, waarvan de een alleen geldig is in de oppervlaktelaag en de ander de gehele grenslaag beschrijft. Dit tweede model is daardoor complexer dan het eerste. Voor hoogtes van meer dan 50 m boven het oppervlak, relevant voor moderne windturbines, is het windprofiel dat geldig is voor de gehele grenslaag het meest gepast. Allereerst is de invloed van het diabatische windprofiel op de vermoeiingsschade bij de bladwortel bepaald voor constante windsnelheden met behulp van het windturbine ontwerppakket Bladed. Verder is een uitvoerige analyse uitgevoerd, met het windturbine simulatiepakket HAWC2, van de gecombineerde invloed van het diabatische windprofiel en turbulentie op de windturbine belastingen. Uit deze analyse blijkt dat het moment bij de torenvoet benvloed wordt door de diabatische turbulentie en de buigmomenten bij de rotornaaf worden benvloed door het diabatische windprofiel. De belastingen bij de bladwortel worden zowel door het diabatische windprofiel als door de diabatische turbulentie benvloed. Dit resulteert in een uitmiddeling van de belastingen bij de bladwortel zodat de berekende belastingen volgens diabatische windcondities ongeveer gelijk zijn aan die volgens neutrale windcondities. Ook blijkt dat het van groot belang is om de windsnelheids-en stabiliteits-verdeling van de specifieke locatie te gebruiken, omdat dit een directe invloed heeft op de windturbine belastingen. De locatie specifieke windcondities geven namelijk een significant lagere vermoeiingsbelastingen dan de IEC norm. Deze norm generaliseert windcondities tot bepaalde windsnelheidsklassen. Als de locatie specifieke wind gegevens beschikbaar zijn biedt dat een mogelijkheid om de kostprijs van windturbines te verlagen. De uitdaging zit dan in het uitvoeren van gedetailleerde metingen om deze wind condities te bepalen.

Momenteel wordt voor windmetingen standaard een cup- of een sonische anem-

ometer gebruikt. Voor beide instrumenten is een meetmast ter plaatse nodig. De anemometers dienen op verschillende hoogten geplaatst te worden om een windprofiel te kunnen meten. Het plaatsen van een meetmast inclusief instrumentatie is erg kostbaar. Met name geldt dit buitengaats omdat de kosten voor de fundering dan aanzienlijk toenemen. Verder dient rekening gehouden te worden met verstoring van de stroming door de meetmast. Een remote sensing instrument zou ideaal zijn om deze problemen het hoofd te bieden. Wind lidars zijn daartoe gedeeltelijk in staat.

Deel II van deze dissertatie onderzoekt of het mogelijk is om turbulentie te meten met behulp van wind lidars. Uitgaande van de basisprincipes van het meten met wind lidars zijn de systematische fouten in de turbulentie metingen bepaald. Er zijn twee belangrijke redenen gevonden voor het optreden van systematische fouten bij dergelijke metingen. Systematische fouten worden veroorzaakt doordat een wind lidar de snelheden over een groot gebied meet en middelt. De tweede oorzaak van systematische fouten is de bijdrage van de componenten van de Reynolds spanningstensor aan de gemeten turbulentie. Met behulp van een scanning-pulsed wind lidar zijn tevens de turbulentie spectra gemeten. Resultaat van dit onderzoek is ondermeer dat nu in detail begrepen wordt hoe de energie van de turbulentie over de verschillende golfgetallen is verdeeld als turbulentie wordt gemeten met een pulserende wind lidar. Deze lidar turbulentie modellen zijn geverifieerd met metingen op diverse hoogtes en voor verschillende atmosferische stabiliteitscondities. Ten slotte is een nieuwe methode onderzocht waarmee het in principe mogelijk wordt om met lidars turbulentie te meten. Deze zogenaamde "six beam" methode gebruikt zes lidar bundels om de fouten te vermijden ten gevolge van alle componenten van de Reynolds spanningstensor bij de bepaling van de turbulentie. De uitgevoerde berekeningen tonen de mogelijkheden van deze methode. Om gebiedsmiddeling te voorkomen is een andere analyse methode nodig; dit is in dit proefschrift niet onderzocht.

Samenvattend kan gesteld worden dat meer onderzoek vereist is om de precieze invloed van de atmosferische stabiliteit op windturbine belastingen te bepalen. Het zal geruime tijd vergen, zeker voor wat betreft het uitvoeren van gedetailleerde metingen en het vergelijking met gemeten belastingen, om de verkregen kennis in dit proefschrift te consolideren een aan te vullen. Zodra lidars in staat zijn om turbulentie goed te meten is er een uitstekende mogelijkheid om optimale locatiespecifieke windturbines te ontwerpen, veel gunstiger dan de huidige op de IEC norm gebaseerde standaard windturbine ontwerpen.

Contents

Chapter 1

Introduction

Energy is vital for the existence of humanity. With tremendous progress in science and technology in the last centuries, and the ever-growing world population, energy needs keep increasing. Fortunately, humans have developed ingenious ways of extracting energy from natural resources. Unfortunately some of that ingenuity has created problems that were not existing before, and we are forced to find solutions to those man-made problems. Coal fired power plants, for example, satisfy much of the energy demands of the society, but they produce unwanted carbon dioxide (CO_2) that has lead to global warming. The same can also be said for the energy extracted from oil and gas. One alternative to such sources of energy is the wind in the atmosphere. A major drawback of wind energy is that it can only be harnessed when the wind blows, and that for economic reasons, only within a certain range of wind speeds. This could perhaps be one of the reasons as to why wind energy has not blossomed into a major source of energy, despite dating back centuries to the time of old Persian wind mills.

The maximum theoretical efficiency of the wind energy extraction was calculated by the German Physicist, Albert Betz in 1919, and was found to be 59.3% [Burton et al., 2001]. Considering the mechanical and electrical efficiency of different components of the wind turbine, the overall efficiency is much less. Research in wind energy did not receive much attention until the oil crisis in the 1970s. In the early 1980s there was a tremendous growth in the development of wind energy, mainly in North America. Hundreds of wind turbines were installed in a short period of time. Subsequent major problems with many wind turbines led to a dramatic fall in installed wind energy capacity. However, the research continued unabated in Northern Europe, especially Denmark. As the world began clamouring over the cause of the climate change, interest in renewable energy surged and in the last decade there has been unprecedented growth in the number of wind turbines, both, onshore and offshore. As a consequence the scientific challenges of optimizing wind energy are ever-increasing. The latest international standards for the design of wind turbines, both, onshore and offshore have been drafted by the IEC [IEC, 2005a,b]. All over the world development of wind farms takes place using the IEC compliant wind turbines.

The IEC [2005a,b] standards prescribe a set of input wind conditions, which the wind turbines have to withstand during their lifetime of approximately 20 years. Wind turbines are designed to withstand fatigue and extreme loads. The focus of this thesis is fatigue loads only. Wind profiles and turbulence are very important for wind turbines since they influence the power production and fatigue loads. Wind profiles are described in the standards using the power law with a fixed value of the shear exponent (0.2 for onshore sites and 0.11 for offshore sites). Turbulence is described by either the Mann [1994] or the Kaimal et al. [1972] model. All wind inputs are prescribed for neutral conditions only.

The power law wind profile is an empirical model with no physical basis, but the convenience of being defined by one parameter only. A more physical representation of the wind profile is based on Prandtl's mixing length theory [Prandtl, 1932], which leads to a logarithmic wind profile. Research on diabatic wind profiles has been carried out since 1950s with the advent of Monin-Obukhov similarity theory [Monin and Obukhov, 1954]. Surprisingly, despite years of research on diabatic wind profiles (particularly for meteorological studies) the IEC [2005a] standard still prescribes the empirical power law wind profile model. In this thesis, diabatic wind profiles are studied at two offshore sites.

The Mann [1994] model of turbulence was a major contribution in the field of micrometeorology in describing the anisotropic turbulence spectral tensor. Up until then for wind turbine applications the two-point turbulence statistics were described using the empirical Kaimal et al. [1972] spectra in combination with some coherence model, e.g. [Davenport, 1961], or the von Kármán [1948] isotropic spectral tensor model. The elegance of using the Mann [1994] model is that the description of the three-dimensional turbulent structure is captured by only three model parameters, $\alpha\epsilon^{2/3}$, which is a product of the spectral Kolmogorov constant α and the rate of viscous dissipation of specific turbulent kinetic energy to the two-thirds power $\epsilon^{2/3}$, a length scale (wavelength of the eddy corresponding to the maximum spectral energy) L_M and an anisotropy parameter Γ. The IEC [2005a] standard define these model parameters for neutral conditions only. In this thesis the Mann [1994] model is also fitted to measurements under diabatic conditions and used to describe the associated turbulence.

In recent years interest in estimating wind turbine loads under diabatic conditions has been growing. In this thesis the diabatic wind profiles and turbulence are used as input wind conditions and fatigue load calculations are carried out using the aero-elastic simulation tool HAWC2. The influence of wind speed and stability distributions at different sites is also investigated.

The wind conditions that are prescribed in the IEC [2005a] standard are divided according to three classes. These classes are defined based on certain generic characteristics of the terrain and wind conditions. Thus the load calculations for a given wind turbine and a site are carried out according to the chosen class based on site characteristics. In reality description of a site based on three classes is very crude, and it would be ideal if site-specific wind conditions are obtained. Moreover, the IEC [2005b] standard for offshore wind turbines recommend using site-specific wind conditions, if measurements are available. Amongst other parameters we then need to measure wind profiles and turbulence. Ground-based remote sensing devices like lidars and sodars provide a huge opportunity in this regard. In meteorology, the use of lidars for wind speed measurements has been a subject of research since the 1960s. For wind energy applications, its use has picked up only in the second half of the last decade [Courtney et al., 2008]. As of today lidars are capable of measuring mean wind speeds quite reliably as compared to the cup anemometers [Courtney et al., 2008, Peña et al., 2009, Smith et al., 2006], and IEC standards are being revised to incorporate them as a standard instrument for the measurement of wind profiles. However, using the current measurement configuration their use in the measurement of turbulence is still questionable [Mann et al., 2009, Sjöholm et al., 2009]. This motivated detailed investigations of the ability of lidars to measure turbulence.

1.1 Thesis objectives

At the start of this PhD project the global research objective was to characterize the inflow wind conditions and analyze their influence on wind turbine loads at an offshore site. There have been only a few measurement campaigns offshore that could measure wind profiles at greater heights. At the first Dutch offshore wind farm, Egmond aan Zee, a meteorological mast was erected in 2005 with a height of about 116.5 m above the mean sea level. The mast is instrumented at three levels, 21, 70 and 116 m in three directions, with several instruments like the cup and sonic anemometers [Kouwenhoven, 2007]. Knowledge of the offshore wind profiles at greater heights was lacking and this provided a wonderful opportunity to measure wind profiles and test models. With time the research objective grew in its scope and was revised to also incorporate research on turbulence measurements using wind lidars. The measurement campaigns carried out using state-of-the-art lidars at the Danish National Wind Turbine Test Center, Høvsøre, provided a great opportunity to understand how lidars measure turbulence. With the heavily instrumented meteorological mast at Høvsøre at different heights, a wonderful opportunity was provided to use the measured wind profiles and turbulence under diabatic conditions and calculate wind turbine loads using the aero-elastic simulation tool HAWC2. This knowledge has been particularly lacking at the start of the PhD project.

In order to carry out the research in a structured manner the following research questions are devised. The answers to these research questions are then combined to form this PhD thesis.

1. How are diabatic wind profiles characterized?
2. Are wind turbine loads influenced by atmospheric stability?
3. Can wind lidars measure turbulence?
4. How do pulsed wind lidars measure turbulence spectra?
5. How would it be possible for wind lidars to measure turbulence?

1.2 Structure of the thesis

This PhD thesis is written as a compilation of four journal and two conference articles. Two journal and two conference articles are already published, whereas the remaining two journal articles have been submitted for publication. The structure of this thesis is such that it is divided into two parts. Part one consists of analysis of diabatic wind profiles, turbulence and their influence on wind turbine loads. Part two consists of investigation of turbulence measurements using wind lidars.

1.2.1 Part I

This part is composed of chapters 2 – 4.

Chapter 2 – Offshore wind profiles In this chapter the first research question posed in section 1.1 is answered. The measurements from two offshore sites in the North Sea are used in combination with two wind profile models, one that is valid in the atmospheric surface layer, and the other that is valid for the entire boundary layer. Atmospheric stability is also characterized at these sites, and various stability distributions are obtained. It is demonstrated that for characterizing the wind profiles at greater heights it is important to use those models, which in principle are valid for the entire boundary layer. This chapter is composed of a journal article published by Sathe et al. [2011a].

Chapter 3 – Influence of diabatic wind profiles on wind turbine loads In this chapter part of the second research question posed in section 1.1 is answered. A hypothetical wind turbine is used for load calculations using the aero-elastic simulation tool Bladed. The wind conditions are considered to be steady and diabatic wind profiles are used as input wind conditions. It is demonstrated that with the use of diabatic wind profiles the fatigue damage is different from that obtained considering only the neutral wind profile. The influence of site specific stability distribution is also considered. From the results of this analysis an impetus is thus provided to perform full scale load calculations considering turbulent winds. This chapter is composed of a conference article published by Sathe and Bierbooms [2007].

Chapter 4 – Influence of atmospheric stability on wind turbine loads This is also related to the second research question posed in section 1.1. The NREL 5 MW reference wind turbine is used for load calculations. Diabatic wind profiles and turbulence are used as input wind conditions. It is demonstrated that atmospheric stability has limited influence on wind turbine loads and the definitions of the input wind conditions are very conservative. This provides an impetus to obtain site-specific input wind conditions. The influence of site specific wind speed and stability distributions is also demonstrated. This chapter is composed of a journal article submitted by Sathe et al. [2011b] to 'Wind Energy'.

1.2.2 Part II

This part is composed of chapters 5 – 7.

Chapter 5 – Measurement of second-order turbulence statistics using wind lidars In this chapter the third research question posed in section 1.1 is answered. Modelling of the systematic errors in turbulence measurements by wind lidars is carried out. Two sources of errors are identified in the turbulence measurements by lidars. Comparison of the model and the measurements is carried out under all atmospheric stabilities. It is demonstrated that the model agrees with the measurements quite well under all stabilities. This chapter is composed of a journal article published by Sathe et al. [2011c].

Chapter 6 – Measurement of turbulence spectra using a scanning pulsed wind lidar In this chapter the fourth research question posed in section 1.1 is answered. Modelling of the turbulence spectra as measured by a scanning pulsed wind lidar is carried out. Comparison of the model with the measurements has demonstrated that we now theoretically understand the distribution of turbulent energy with respect to the wavenumbers as measured by a scanning pulsed wind lidar. It also provides an impetus to perform modelling of gusts as measured by lidars. This chapter is composed of a journal article by Sathe and Mann [2011] that is accepted for publication in the 'Journal of Geophysical Research'.

Chapter 7 – How can wind lidars measure turbulence? A preliminary investigation In this chapter part of the fifth research question posed in section 1.1 is answered. In order to avoid the systematic errors in turbulence measurements as described in chapters 5 and 6 a new method based on using six lidar beams is investigated. Theoretical calculations are carried out, which demonstrate that the new method has the potential that makes turbulence measurements using lidars possible. The optimization of the six beam configuration is carried out based on minimizing the random errors in the turbulence measurements. This chapter is a conference article published by Sathe et al. [2011d].

1.2.3 Conclusions

Chapter 8 – Conclusions and future work In this chapter individual conclusions from chapters 2 – 7 are stated and combined to form overall conclusions. Several recommendations for future work are proposed that can be treated as individual research topics.

Part I

Diabatic wind profiles, turbulence and their influence on wind turbine loads

Chapter 2

Offshore wind profiles

In this chapter atmospheric stability and wind profile models are analyzed at two offshore sites in the North Sea. The first site is Egmond aan Zee in the Dutch North Sea and the second site is Horns Rev in the Danish North Sea. The IEC [2005a] standard prescribes the power law wind profile defined by a shear exponent. There are two issues with this model. The first is that it is an empirical model with no physical basis, and the second is that no consideration to atmospheric stability is given. A more physical model of the wind profile is the logarithmic law that is a function of friction velocity u_* and aerodynamic roughness length z_0. It is derived from the local wind shear equation $\partial u/\partial z = u_*/\kappa z$, where u is the mean wind speed, κ is the von Kármán constant and z is the height. Atmospheric stability is characterized in the form of Monin-Obukhov length L. Under diabatic conditions the local wind shear is also a function of the stability parameter z/L. The $\phi_m(z/L)$ function, which is used to correct the wind profile model for stability effects, is very different under unstable conditions as compared to stable conditions. We thus obtain different expressions for the logarithmic wind profile under diabatic conditions. Strictly speaking this model is only applicable to the atmospheric surface-layer, which is approximately the lowermost 10% of the atmospheric boundary layer.

Modern wind turbines operate in the surface layer and well beyond it. There is thus a need to model the wind profile that is valid for the entire boundary layer. In the article that follows this introduction we analyze two different wind profile models and compare it with the measurements. One is the standard surface-layer model and the second is the Gryning et al. [2007] model that is valid for the entire boundary layer. The merits and demerits of each of them are described in detail. Atmospheric stability is also analyzed at the two offshore sites with a view to describing the climatology at these sites.

WIND ENERGY
Wind Energ. 2011; **14**:767–780

RESEARCH ARTICLE

Comparison of the atmospheric stability and wind profiles at two wind farm sites over a long marine fetch in the North Sea

Ameya Sathe[1,2], Sven-Erik Gryning[2] and Alfredo Peña[2]

[1] TU Delft, 2629 HS, Delft, The Netherlands
[2] Wind Energy Division, Risø DTU, 4000, Roskilde, Denmark

ABSTRACT

A comparison of the atmospheric stability and wind profiles using data from meteorological masts located near two wind farm sites in the North Sea, Egmond aan Zee (up to 116 m) in the Dutch North Sea and Horns Rev (HR; up to 45 m) in the Danish North Sea, is presented. Only the measurements that represent long marine fetch are considered. It was observed that within a long marine fetch, the conditions in the North Sea are dominated by unstable [41% at Egmond aan Zee Offshore Wind Farm (OWEZ) and 33% at HR] and near-neutral conditions (49% at OWEZ and 47% at HR), and stable conditions (10% at OWEZ and 20% at HR) occur for a limited period. The logarithmic wind profiles with the surface-layer stability correction terms and Charnock's roughness model agree with the measurements at both sites in all unstable and near-neutral conditions. An extended wind profile valid for the entire boundary layer is compared with the measurements. For the tall mast at Egmond aan Zee, it was found that for stable conditions, the scaling of the wind profiles with respect to boundary-layer height is necessary, and the addition of another length scale parameter is preferred. At the lower mast at HR, the effect was not noticeable. Copyright © 2011 John Wiley & Sons, Ltd.

KEYWORDS
atmospheric stability; Obukhov length; wind profiles; boundary-layer height

Correspondence
Ameya Sathe, Section Wind Energy, TU Delft, Kluyverweg 1, 2629 HS Delft, The Netherlands.
E-mail: A.R.Sathe@tudelft.nl

Received 5 May 2010; Revised 1 January 2011; Accepted 3 January 2011

1. INTRODUCTION

This study is important for wind energy applications since wind profiles have a significant influence on power production and loads on turbines. The International Electrotechnical Commission standard[1] suggests the use of either a logarithmic profile without the diabatic correction term or an empirical power law with the power exponent depending on wind speed only, although it also depends on roughness, height and atmospheric stability.[2] Lange *et al.*[3] demonstrated the importance of using diabatic wind profiles for power production calculations, and Sathe and Bierbooms[4] demonstrated the same for simple load calculations considering only steady winds.

The study of the diabatic wind profile started from a pioneering work on a similarity theory[5] [Monin–Obukhov similarity theory (MOST)] where the dimensionless wind shear depends on a dimensionless stability parameter. The advent of MOST led to the experimental research on the empirical similarity relations between the dimensionless wind shear and the atmospheric stability such as those derived from the Kansas experiment.[6] The conditions for which the similarity relations from Businger *et al.*[6] are derived depict flat and homogeneous terrain satisfying the assumptions of MOST to the best possible extent.

The applicability of MOST to marine conditions is not obvious since the sea roughness length depends on wind speed, which traditionally is represented by the Charnock's relation.[7] Studies have further shown its dependence on fetch[8] and wave age[9] among others. Numerous studies of wind profiles have been conducted in the past over the land and the sea, resulting in various suggestions on the empirical relation between the non-dimensional wind shear and stability.[10–12] Experimental verification over the sea is still a challenge. Walmsley[13] studied the wind profile over the sea using data from Sable Island and concluded that the thermal stratification effect is quite significant. van Wijk *et al.*[14] studied the wind profile over the North Sea and found better agreement with measurements when the diabatic correction was applied than with the logarithmic profile. Coelingh *et al.*[15] studied the wind profiles in the Dutch North Sea using measurements (up to 75 m) from various platforms and found that the conditions are mainly unstable and that surface-layer theory agreed well with the measurements. Recently, Lange *et al.*[16] studied the advection effects (warm air from the land toward sea) on wind profiles and suggested a correction term for the traditional diabatic wind profile. Motta and Barthelmie[17] compared measurements at different offshore sites in the Baltic Sea and verified the validity of the diabatic wind profile. Gryning *et al.*[18] proposed a new model of wind profile for the entire boundary layer based on the assumption that the friction velocity varies linearly with height. The wind profiles were also studied using lidars,[19] and a new method was proposed to depict marine wind profiles in a non-dimensional form.[20] Using the lidar observations, a modified wind profile based on the theory from Gryning *et al.*[18] is suggested for the marine boundary layer in Peña *et al.*[21]

The goal of this work is twofold. First is to compare the climatology at two sites in the North Sea in terms of daily, seasonal and overall stability distribution. Second is to investigate the wind profile, based on two mixing-length models. The first is the surface-layer wind profile, and the second is the extended model of Gryning *et al.*[18] that characterizes the wind profile in the entire boundary layer. Section 2 describes the theoretical background on wind profiles. Section 3 describes the data used for the validation of wind profile models. Section 4 describes the results of the atmospheric stability and wind profile analysis. Finally, Section 5 provides a discussion.

2. THEORETICAL BACKGROUND

In the surface layer, the diabatic wind profile is given as

$$u = \frac{u_{*0}}{\kappa}\left[\ln\left(\frac{z}{z_0}\right) - \psi_m(z/L)\right] \tag{1}$$

where u_{*0} is the friction velocity near the ground, $\kappa = 0.4$ is the von Kármán constant, z is the height, z_0 is the aerodynamic roughness length, L is the Obukhov length and $\psi_m(z/L)$ is the empirical stability function. We use the ψ_m relation from Businger *et al.*[6] for stable conditions and that from Grachev *et al.*[12] for unstable conditions, where L is given as

$$L = -\frac{{u_{*0}}^3 T}{\kappa g \overline{w'\theta_v'}} \tag{2}$$

Here, T is the absolute temperature, θ_v is the virtual potential temperature and $\overline{w'\theta_v'}$ is the virtual kinematic heat flux. Over the sea, z_0 can be approximated by Charnock's relation:

$$z_0 = \alpha \frac{u_{*0}^2}{g} \tag{3}$$

where α is the Charnock parameter ($\alpha = 0.0144$ is used in this analysis based on Gryning *et al.*[2]) and g is the acceleration due to gravity.

Gryning *et al.*[18] extended the wind profile for the entire boundary layer, based on the assumption that the length scale is an inverse summation of three length scales

$$\frac{1}{l} = \frac{1}{L_{\mathrm{SL}}} + \frac{1}{L_{\mathrm{MBL}}} + \frac{1}{L_{\mathrm{UBL}}} \tag{4}$$

where L_{SL}, L_{MBL} and L_{UBL} are the length scales of the surface, middle boundary and upper boundary layers, respectively. The justification of using the inverse summation is not given in Gryning *et al.*,[18] but it could be explained if we assume that the wind profile in the entire boundary layer is a linear sum of wind profiles in the surface, middle boundary and upper boundary layers. The derivation of the extended wind profiles is given in Gryning *et al.*,[18] and only the final forms are shown here. These are

$$U = \frac{u_{*0}}{\kappa}\left[\ln\left(\frac{z}{z_0}\right) + \frac{z}{L_{\mathrm{MBL}}} - \frac{z}{z_i}\left(\frac{z}{2L_{\mathrm{MBL}}}\right)\right] \tag{5}$$

for neutral conditions,

$$U = \frac{u_{*0}}{\kappa}\left[\ln\left(\frac{z}{z_0}\right) - \psi_m(z/L) + \frac{z}{L_{\mathrm{MBL}}} - \frac{z}{z_i}\left(\frac{z}{2L_{\mathrm{MBL}}}\right)\right] \tag{6}$$

for unstable conditions and

$$U = \frac{u_{*0}}{\kappa}\left[\ln\left(\frac{z}{z_0}\right) - \psi_m(z/L)\left(1 - \frac{z}{2z_i}\right) + \frac{z}{L_{\mathrm{MBL}}} - \frac{z}{z_i}\left(\frac{z}{2L_{\mathrm{MBL}}}\right)\right] \tag{7}$$

for stable conditions, where z_i is the height of the planetary boundary layer. z_i is assumed to be climatologically proportional to u_{*0} under neutral conditions as

$$z_i = c\frac{u_{*0}}{|f_{\mathrm{c}}|} \tag{8}$$

where f_{c} is the Coriolis parameter and c is a proportionality constant. For a neutral homogeneous terrain, Peña *et al.*[23] estimated $c = 0.15$ from the re-analysis of the Leipzig wind profile. Considering that the conditions over the sea are nearly homogeneous, the same value of c is used in this work. However, under diabatic conditions, there is no agreement on diagnostic expressions for z_i.[24] In the absence of measurements, it is expected that the climatological z_i decreases as the conditions become more stable. Hence, $c = 0.14$ is used for stable conditions and $c = 0.13$ for very stable conditions as in Peña *et al.*[21] The mean value of z_i obtained during neutral conditions is also applied for unstable conditions in accordance with Peña *et al.*[25] The z_i estimated using the sound detection and ranging and the radio acoustic sounding system[26] has been found to be close to that of the aerosol analysis.

A new scaling parameter in equations (5)–(7) is L_{MBL}. Gryning *et al.*[18] used Rossby number similarity to equate the geostrophic wind with equations (5)–(7) at $z = z_i$. However, this results in the dependence of L_{MBL} on the uncertain resistance law constants A and B. L_{MBL} can also be fitted to equations (5)–(7) using the measurements, and an empirical formulation can be devised.[18]

The traditional way of depicting a wind profile is by plotting the non-dimensional wind speed (u/u_{*0}) against the non-dimensional height (z/z_0). Over sea, z_0 is not a constant, and the traditional representation is inadequate in a statistical evaluation, since the individual non-dimensional wind profiles vary with z_0 and L. Following Peña *et al.*,[20] the neutral wind profiles are depicted in a non-dimensional form as

$$\frac{u}{u_{*0}} + \frac{1}{\kappa}\ln\left[1 + 2\frac{\Delta u_{*0}}{\overline{u_{*0}}} + \left(\frac{\Delta u_{*0}}{\overline{u_{*0}}}\right)^2\right] = \frac{1}{\kappa}\ln\left(\frac{z}{\overline{z_0}}\right) \tag{9}$$

where for each stability class, $\overline{u_{*0}}$ is the mean friction velocity, Δu_{*0} is the fluctuation of the friction velocity, and $\overline{z_0} = \alpha\overline{u_{*0}}^2/g$ is the mean roughness length. Thus, under neutral conditions, the theoretical non-dimensional profiles match with the non-dimensional height scaled with $\overline{z_0}$. Under diabatic conditions, the appropriate ψ_m function is subtracted from the non-dimensional height in equation (9). A major advantage of this approach is that the wind profiles for a given non-dimensional stability, z_0/L, collapse onto a single profile. This approach can be used with the extended wind profiles, equations (5)–(7), by adding appropriate terms to the non-dimensional height. Thus, the variability of marine wind profiles can be observed with respect to stability.

3. DATASETS

Figure 1 shows the locations of the two offshore sites in the North Sea separated by a distance of about 400 km:

- A 116 m tall meteorological mast located at about 18 km from the coast of Egmond aan Zee, the Netherlands, coordinates 52°36′22.9″N, 4°23′22.7″E [henceforth referred to as the Egmond aan Zee Offshore Wind Farm (OWEZ)], used as the reference for the first Dutch offshore wind farm. The depth of water is approximately 20 m
- A 62 m tall met mast located at about 18 km from the coast of Jutland, Denmark, used as the reference of the large offshore wind farm HR I, located at coordinates 55°31′09″N, 7°47′15″E

Figure 2 shows that at OWEZ, the sector that is not influenced by the wakes of the turbines is 135–315°, and at HR, it is 180–360° and 0–90°. Figure 3 shows that the dominant wind directions are between 180–300° at OWEZ and 180–330° at HR. In order to avoid coastal effects and the internal boundary layer from the land–sea interaction, the sector 225–315° was chosen in this analysis for both sites.

3.1. OWEZ

The site comprises 36 Vestas V90 turbines. Meteorological measurements are taken at three levels: 21, 70 and 116 m. The analysis was carried out using the 10 min mean measurements between July 2005 and December 2008. Mierij Meteo cup anemometers (KNMI Anemometer model 018, KNMI, De Bilt, The Netherlands) is placed on booms in three directions to

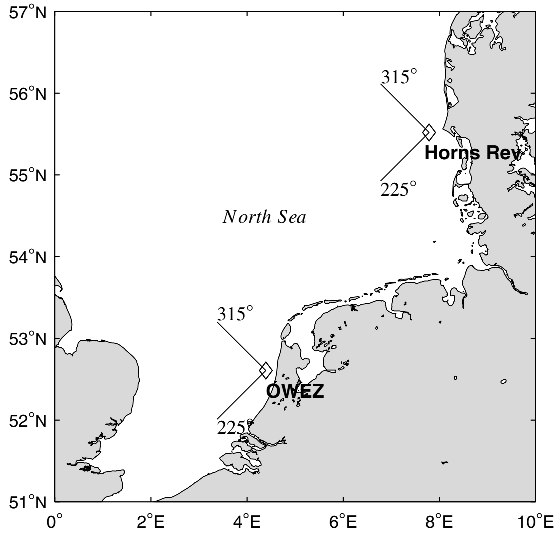

Figure 1. Location of the OWEZ and Horns Rev (HR) meteorological masts in the North Sea and the sectors used in the analysis.

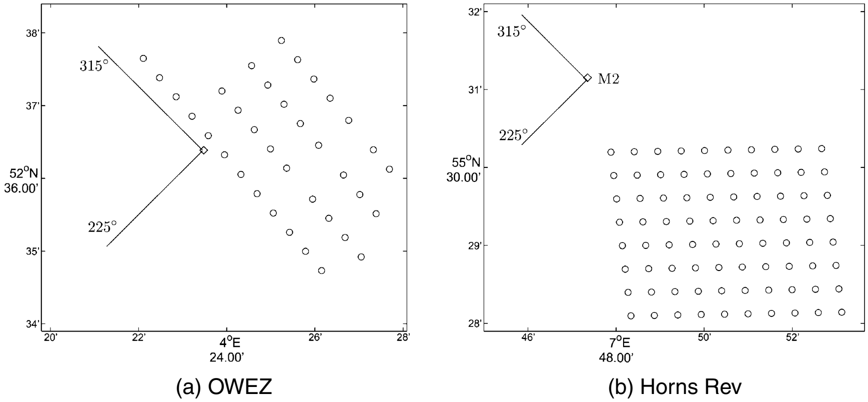

(a) OWEZ (b) Horns Rev

Figure 2. Location of the met masts (in diamonds) with respect to the wind farms. The wind turbines are represented as circles.

avoid direct mast shade effects on measurements. Wind vanes are also placed in those directions. A combined temperature–humidity sensor is also available at each height. The water temperature is measured at 3.8 m below the mean sea level. Ideally, the temperature difference at the air–sea interface is required for the stability analysis.[27] However, because of the lack of sea surface temperature (SST), the water measurements are considered to represent the SSTs (henceforth, the sea water temperature at -3.8 m will be referred as OWEZ SST). The location of the mast has been chosen such that it ensures free stream wind speed in the dominant south-west direction [see Figures 2(a) and 3(a)]. In order to select a particular cup anemometer and wind vane, preliminary checks are applied to avoid mast effects on measurements (details are given in Sathe[28]). Only observations of wind speeds greater than 4 m s^{-1} were used in the analysis.

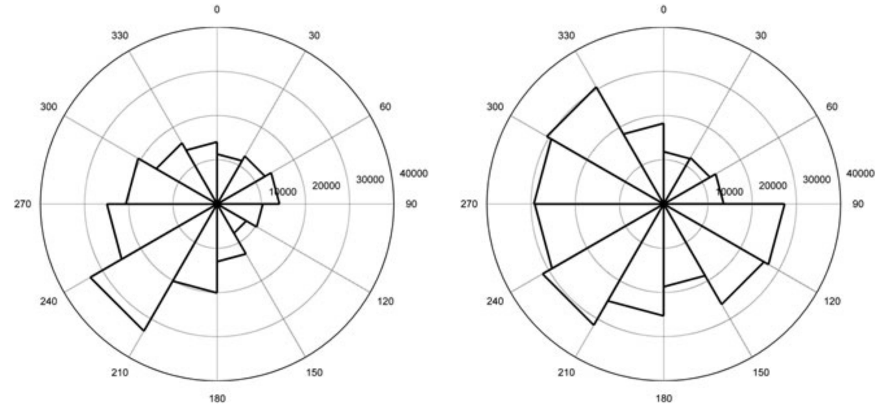

(a) OWEZ

(b) Horns Rev

Figure 3. Wind rose from observations at 21 m at OWEZ and 43 m at HR. The numbers inside the circles are the number of 10 min observations.

3.2. HR

The measurements at HR are described in Peña *et al.*[21] Here, we use 10 min mean measurements (met mast M2) of wind speed at 15, 30 and 45 m, air temperature at 13 m and water temperature at 4 m below mean sea level. Peña *et al.*[21] compared satellite measurements of SSTs to the water temperatures at HR and found no significant bias. Hence, the water temperature at -4 m was used directly and will be referred to as HR SST. Relative humidity at 13 m was used to convert the air temperatures to virtual temperatures. The period available for the analysis is between April 1999 and December 2006. Only observations of wind speeds greater than 4 m s^{-1} were used in the analysis.

4. RESULTS

The study is divided into two parts: statistics of atmospheric stability and validation of wind profile models. MOST is based on the assumptions of homogeneous, stationary conditions and constant fluxes. It is thus confined to the surface layer. Non-stationarities in the data are checked following Lange *et al.*[16] Usually, the height of the surface layer is about 60–100 m during unstable and neutral conditions and less than about 30 m during stable conditions.[23] Preliminary checks applied at OWEZ revealed that if a filter based on surface-layer height is applied, then only 5% of the available measurements are usable. The study of climatology with such limited data is not of much use. Hence, no filter was applied to the data based on the surface-layer height. Such checks were not necessary at HR since measurements up to only 45 m were used. The data availability at both sites is given in Table I. Seven stabilities were used to classify the observations (see Table II) as given in Gryning *et al.*[18] Sathe[28] attempted to reason the choice of using a particular stability classification (e.g. that in Coelingh *et al.*[15] and Motta and Barthelmie[17] is different from the one in Gryning *et al.*[18]). It was concluded that when a continuous description in terms of L is not feasible, the classification in Table II is appropriate.

Table I. Data availability at OWEZ and HR.

	OWEZ (%)	HR (%)
Total available data		
Wind direction, < 225 or > 315°	63	64
Wind direction, > 225 and < 315°	37	36
Data within the selected wind directions (225–315°)		
Filtered data	28	18
Available data	72	82

Table II. Classification of atmospheric stability according to Obukhov length intervals.

Very stable	$10 \leq L \leq 50$ m
Stable	$50 \leq L \leq 200$ m
Near-neutral stable	$200 \leq L \leq 500$ m
Neutral	$\mid L \mid \geq 500$ m
Near-neutral unstable	$-500 \leq L \leq -200$ m
Unstable	$-200 \leq L \leq -100$ m
Very unstable	$-100 \leq L \leq -50$ m

Estimation of L is not straightforward. High-frequency wind and temperature measurements can be directly used in the eddy covariance method. However, because of the lack of high-frequency temperature measurements, this is not possible at OWEZ. At HR, no high-frequency measurements are available for the chosen period of analysis. Several methods can be used to estimate L from the mean observations:[3]

- Profile methods—Different profile methods are available in the literature.[17,29,30] All methods require the use of the wind profile equation (1). Its use is quite debatable, since it is strictly valid in the surface layer only. Moreover, the higher the measurements, the higher the uncertainty. Thus, its use is justified only if the measurements are available within the first few meters (up to 10 m) for all stability conditions. The lowest measuring height at OWEZ and HR are 21 and 15 m, respectively. Our preliminary study showed that fluxes derived using this method tend to overpredict the wind profile significantly under stable conditions at OWEZ, and hence, it was not employed in the analysis.
- Gradient Richardson number ($\mathrm{Ri_g}$) method—Measurements at two different levels in the atmosphere are required to estimate $\mathrm{Ri_g}$. It can be shown that z/L and therefore ψ_m become dependent on the inverse of the square of the wind speed difference between the two levels ($1/\Delta u^2$). High accuracy of wind speed measurements is therefore required to measure fluxes. Hence, this method is not used in the analysis.
- Bulk Richardson number ($\mathrm{Ri_b}$) method—Grachev and Fairall[31] provide the dependence of $\mathrm{Ri_b}$ on the stability parameter z/L. The empirical constants to convert $\mathrm{Ri_b}$ into z/L for unstable and stable conditions were derived using measurements over the ocean. The method has been used in recent studies.[3,20,21] Moreover, it requires wind speed measurements at one height only to estimate L. Hence, this method was used in the analysis. Observations of wind speed and air temperature at 21 and 15 m at OWEZ and HR, respectively, were used in conjunction with the SST to estimate $\mathrm{Ri_b}$.

  Since the $\mathrm{Ri_b}$ method is sensitive to temperature measurements, the calibrations are checked at both sites. The temperature measurements at OWEZ are accurate up to $\pm 0.1°$C (confidential calibration reports) and at HR up to $\pm 0.354°$C.[32] Following Vincent *et al.*,[33] an uncertainty analysis for L is carried out, where it was found that the combined uncertainty of L increases rapidly as the difference in virtual potential air and sea surface temperatures is reduced. Thus, L is most uncertain in neutral conditions, and as the atmosphere becomes more stable or unstable, the uncertainty in L reduces.

4.1. Statistics of atmospheric stability

The statistics are presented as daily, monthly and overall distributions of L. The SSTs at OWEZ are corrected by subtracting 0.82°C. Without this correction, the measured non-dimensional wind profiles at OWEZ have a significant offset compared to the theoretical wind profiles [equation (9)] under all conditions, even at the lowest measurement height. A combination of satellite and *in situ* measurements from the European Centre for Medium-Range Weather Forecasts Re-analysis interim dataset was used for comparison with the OWEZ SSTs for a period between July 2005 and October 2008. It is found that there is an offset of 0.82°C at OWEZ. A comparison of SST at HR with the ECMWF, as well as satellite measurements, did not show a significant offset, in agreement with Peña *et al.*[21]

Figure 4 shows the daily variation in atmospheric stability for the two sites in the North Sea; no pronounced daily variation is found at OWEZ and HR. Only marine sectors are analysed (Figure 1).

Figure 5 shows the seasonal variation of atmospheric stability at both sites. There is a clear seasonal component of atmospheric stability at both sites, being more prominent at HR. There is a marked increase of unstable conditions during the summer months and an increase of stable conditions during the winter months. The peak of unstable conditions is found in late summer (August/September), whereas the peak in the stable conditions occurs in winter (February). The statistics for the month of December at OWEZ are not shown because of the limited number of data. The monthly data availability is shown in Table III.

It is observed that for December, the usable data are as low as 1% of the total number of records. It is also noticed that the use of unequal numbers of observations in each month weights the results toward the summer.

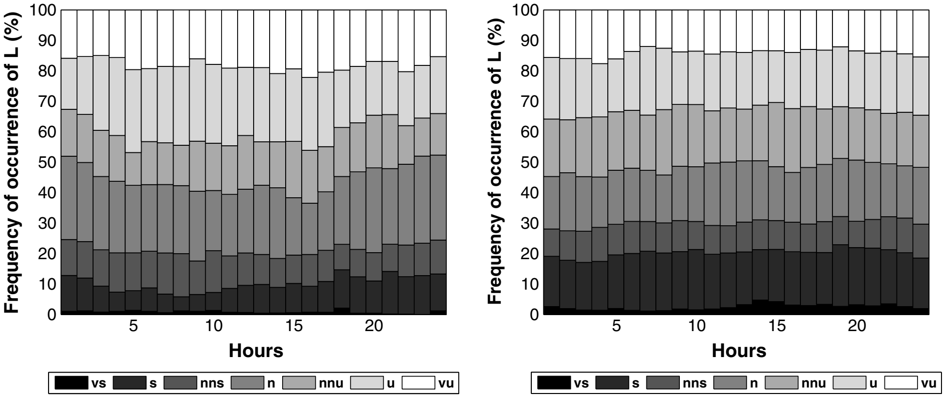

(a) OWEZ (b) Horns Rev

Figure 4. Daily variation of atmospheric stability between 225 and 315°. vs, very stable; s, stable; nns, near-neutral stable; n, neutral; nnu, near-neutral unstable; u, unstable; vu, very unstable.

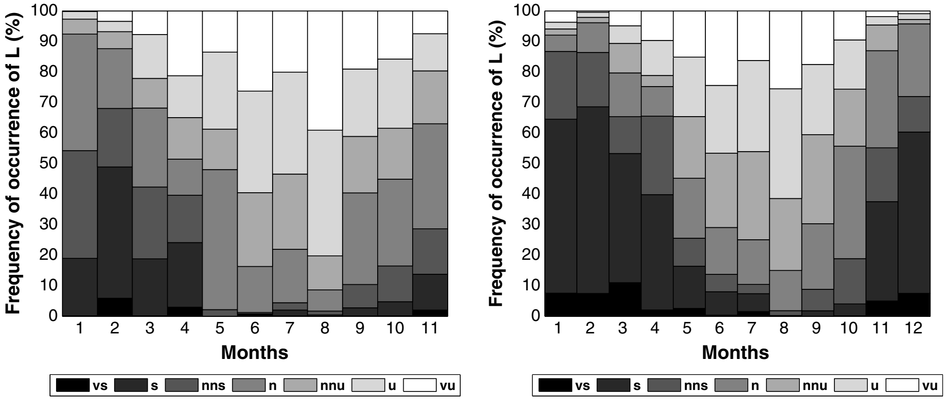

(a) OWEZ (b) Horns Rev

Figure 5. Seasonal variation of atmospheric stability between 225 and 315°. vs, very stable; s, stable; nns, near-neutral stable; n, neutral; nnu, near-neutral unstable; u, unstable; vu, very unstable.

Figure 6 shows the variation of atmospheric stability with wind speed. At both sites, there is an increase of neutral conditions with increasing wind speeds. However, at HR there is a sudden increase of near-neutral stable conditions at certain wind speeds—18, 19 and 20 m s^{-1}. This increase is also observed but to a lesser degree at OWEZ. There are many values of L within the range of 400–500 m, where the spikes are observed. Lowering of the threshold (from 500 to 400 m, Table II) for the neutral interval results in a substantial increase in the number of neutral conditions for those wind speeds, and no spikes are observed. Stability classification is rather sensitive to those values of L that are in the edges of the interval.

Figure 7 shows the variation of atmospheric stability with wind direction. A systematic increase in the number of unstable conditions and a decrease of stable conditions are observed at both sites as the wind direction changes from south-west to north-west, indicating that the air generally is colder for northerly wind directions. The result is also in agreement with an independent investigation carried out at HR.[34]

Table III. Monthly data availability of 10 min observations at OWEZ and HR in the long marine fetch sector (225–315°).

Month	Total available data; percentage of the whole period		Percentage of data removed by the filter		Percentage of usable data	
	OWEZ	HR	OWEZ	HR	OWEZ	HR
January	6	4	1	1	5	3
February	6	7	2	1	4	6
March	8	5	3	1	5	4
April	7	4	2	1	5	3
May	4	11	1	2	3	9
June	9	14	3	2	6	12
July	14	13	5	2	9	11
August	14	13	4	2	10	11
September	12	11	3	2	9	9
October	11	11	2	2	9	9
November	6	4	1	1	5	3
December	3	3	2	1	1	2

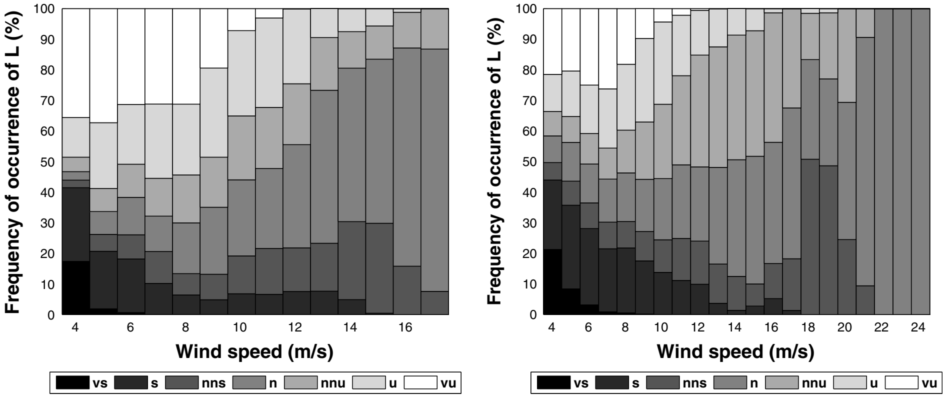

(a) OWEZ (b) Horns Rev

Figure 6. Variation of atmospheric stability with respect to wind speed between 225 and 315°. vs, very stable; s, stable; nns, near-neutral stable; n, neutral; nnu, near-neutral unstable; u, unstable; vu, very unstable.

Figure 8 shows the overall distribution of atmospheric stability for the two sites. In general, the conditions are mainly neutral and unstable. This is also in conformity with the observations of Coelingh *et al.*[15] for the Dutch part and of Floors[34] for the Danish part of the North Sea. There are more unstable conditions at OWEZ [Figure 8(a)] than at HR [Figure 8(b)] and in general less stable conditions at OWEZ as compared with that at HR.

4.2. Comparison of the non-dimensional wind profiles

Figure 9 shows the comparison of the non-dimensional wind profiles at both sites. The measurements are divided into seven stability classes (Table II), and a mean (theoretical and measured) profile is plotted for each stability class. The mean observed parameters are given in Table IV.

The theoretical profiles are computed using equation (9). The stability correction is added to equation (9) using equation (1) for non-neutral conditions. They agree with the measurements very well at both sites in unstable and neutral conditions, particularly at OWEZ. This result is quite significant since there is an ongoing debate on the use of diabatic wind profile, equation (1), in wind energy. A recent study[21] has indicated (using a different dataset) that equation (1) can be used for the marine unstable and neutral conditions even beyond the surface layer, and the wind profiles at OWEZ and HR conform with these findings (Figure 9).

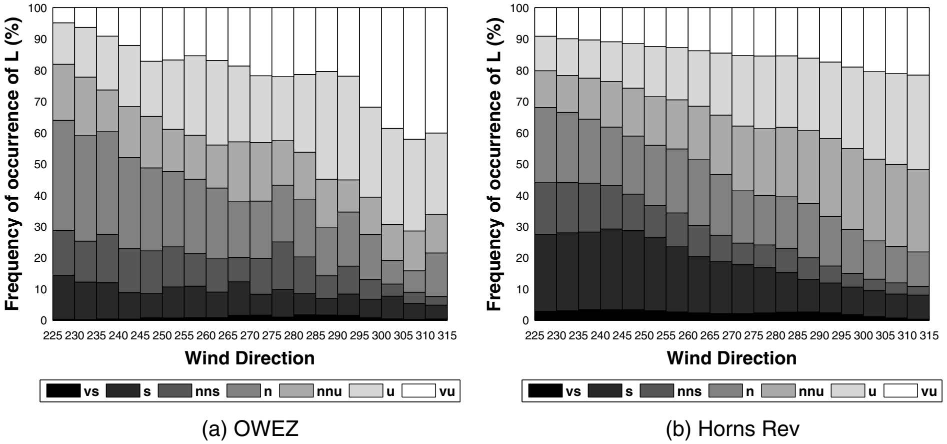

(a) OWEZ

(b) Horns Rev

Figure 7. Variation of atmospheric stability with wind direction. vs, very stable; s, stable; nns, near-neutral stable; n, neutral; nnu, near-neutral unstable; u, unstable; vu, very unstable.

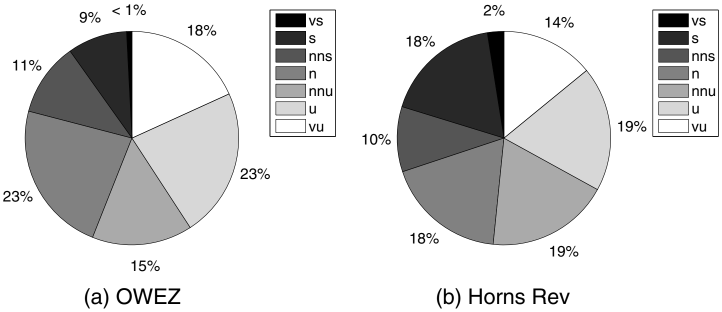

(a) OWEZ

(b) Horns Rev

Figure 8. Overall distribution of atmospheric stability between 225 and 315°. vs, very stable; s, stable; nns, near-neutral stable; n, neutral; nnu, near-neutral unstable; u, unstable; vu, very unstable.

At OWEZ, equation (1) significantly overpredicts the stable wind profile with increasing height. Scaling with z_i reduces the wind shear at greater heights.[21] At HR, such an overprediction is not observed, since the comparison is made at low measurement heights (up to 45 m) only. In the model of Gryning,[18] the wind speed profile also depends on z_i and L_{MBL}. Peña *et al.*[21] argued that L_{MBL} over the sea is quite large, and hence, its influence can be neglected. This results in scaling the wind profile under stable conditions with z_i only, whereas the unstable and neutral wind profiles conform with those from surface-layer theory [equation (1)]. In our preliminary study, L_{MBL} was fitted to the OWEZ measurements according to equations (5)–(7), and it was found that L_{MBL} is very large for unstable and neutral conditions in accordance with Peña *et al.*,[21] whereas for stable conditions, L_{MBL} could not be neglected. Gryning *et al.*[18] further showed that L_{MBL} depends on the resistance law constants A and B. In this analysis, the values for A and B from Peña *et al.*[25] were used to estimate the influence of L_{MBL} on the wind profiles in conjunction with z_i. The A, B, z_i and L_{MBL} values used to obtain the extended wind profiles for stable conditions [equation (7)] are given in Table V.

Figure 10 shows the extended stable wind profiles using equations (1), (7) and (9) at OWEZ. It is observed that the theoretical profile has a slightly better agreement with the measured profile when the combined effect of z_i and L_{MBL} is considered than assuming only the effect of z_i. Both approaches agree better with the observations than with the surface-layer theory. Table VI shows the root mean square error (RMSE) between the stable wind profile models and

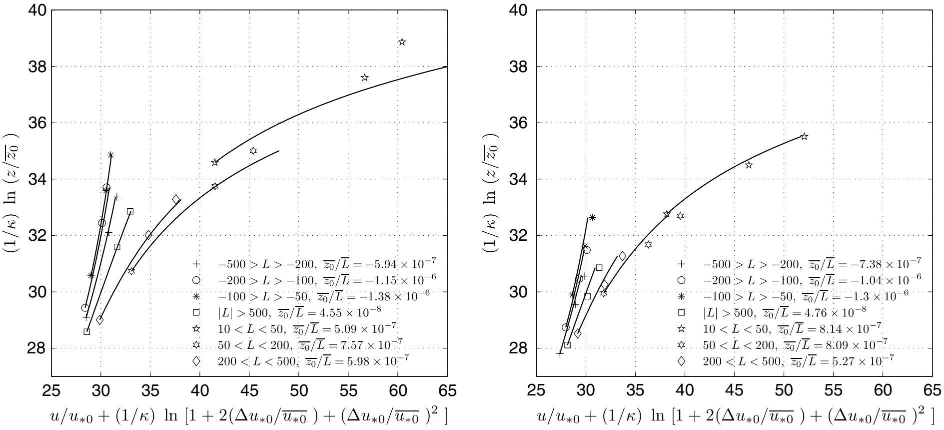

(a) OWEZ

(b) Horns Rev

Figure 9. Non-dimensional wind profiles between 225 and 315° at the two sites in the North Sea. Measurements are shown by different markers and equation (9) in solid lines.

Table IV. Mean observed parameters between 225 and 315° at OWEZ and HR in each stability class used for plotting the wind profiles according to equation (9).

	$\overline{L}$ (m)	$\overline{u_{*0}}$ (m s^{-1})	No. of profiles	$\overline{z_0}$ (m)
OWEZ				
Very unstable	−74	0.26	3959	1.02×10^{-4}
Unstable	−140	0.33	4913	1.61×10^{-4}
Near-neutral unstable	−311	0.36	3303	1.85×10^{-4}
Neutral	$\|L\| = 4999$	0.39	5013	2.27×10^{-4}
Near-neutral stable	321	0.36	2416	1.92×10^{-4}
Stable	128	0.26	1960	9.62×10^{-5}
Very stable	41	0.12	133	2.06×10^{-5}
HR				
Very unstable	−73	0.26	7775	9.62×10^{-5}
Unstable	−146	0.32	10,436	1.53×10^{-4}
Near-neutral unstable	−299	0.39	10,278	2.21×10^{-4}
Neutral	$\|L\| = 4116$	0.37	10,083	1.96×10^{-4}
Near-neutral stable	316	0.34	5441	1.66×10^{-4}
Stable	117	0.25	9800	9.41×10^{-5}
Very stable	38	0.14	1297	3.05×10^{-5}

Table V. Mean parameters used for the stable wind profiles between 225 and 315° according to equation (7) at OWEZ.

	Near-neutral stable	Stable	Very stable
L (m)	321	128	41
A	1.5	1.5	1.6
B	5.2	5.2	5.2
z_i (m)	205	117	49
L_{MBL} (m)	866	283	69

the observations at OWEZ. At each height, and for each stability class, the RMSE is calculated from all 10 min observations. It is found that as the height increases, the RMSE decreases either using z_i only or a combination of z_i and L_{MBL} for the extended wind profile model [equation (7)] as compared to the standard surface-layer theory [equation (1)]. The

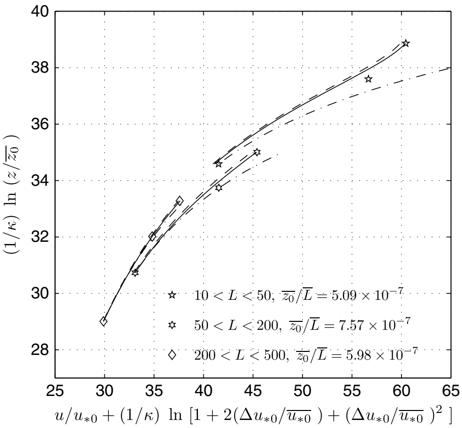

Figure 10. Extended wind profiles between 225 and 315° at OWEZ showing the influence of z_i and L_{MBL} under stable conditions. The dashed line shows the influence of z_i only, and the solid line shows the combined effect of z_i and L_{MBL}. The dash-dot line shows the traditional surface-layer theory [equation (1)], and the markers are the measurements.

Table VI. Root mean square error in m s^{-1} between the theoretical profiles and the observations (225–315°) at OWEZ .

	21 m	70 m	116 m
Near-neutral stable			
Equations (5)–(7)	0.02	1.46	2.62
Equations (5)–(7), neglecting L_{MBL}	0.03	1.47	2.62
Equation (1)	0	1.47	2.66
Stable			
Equations (5)–(7)	0.08	2.5	4.35
Equations (5)–7), neglecting L_{MBL}	0.13	2.62	4.39
Equation (1)	0	2.36	5.71
Very stable			
Equations (5)–(7)	0.48	5.91	9.22
Equations (5)–(7), neglecting L_{MBL}	0.62	6.06	9.24
Equation (1)	0	8.48	21.97

approach of using z_i only slightly underpredicts the wind profile. Similar comparisons are not required at HR since the measurements are up to 45 m only, and therefore, the effect on L_{MBL} is small. The stable surface-layer profiles already compared well with the measurements at HR [Figure 9(b)].

4.3. Comparison of the wind speed power spectra

Power spectra of 10 min observations of the horizontal wind speed is derived to illustrate how related are the two sites in terms of the wind climate. HR and OWEZ lie in the North Sea separated by approximately 400 km. It is therefore likely that if the two sites are similar in wind climatology, storm events and weather systems show up at both sites on the spectra on the order of hours. Mesoscale and microscale phenomena associated with coastal effects will show up in the spectra at high frequencies.

Figure 11 shows the wind spectra comparison based on 10 min measurements. The observations at 21 and 15 m are used at OWEZ and HR, respectively. All wind directions are used. The period of comparison is between July 2005 and October 2006, since continuous measurements are mostly available during this period. For the periods where the data are missing, mean wind speed is used at respective sites. The spectra at OWEZ and HR compare quite well at frequencies of the order of hours. At high frequencies (of the order of minutes), the spectral energy at OWEZ is greater than that at HR. OWEZ is to a large degree surrounded by land as compared with HR (Figure 1), and hence, an increase in mesoscale variability

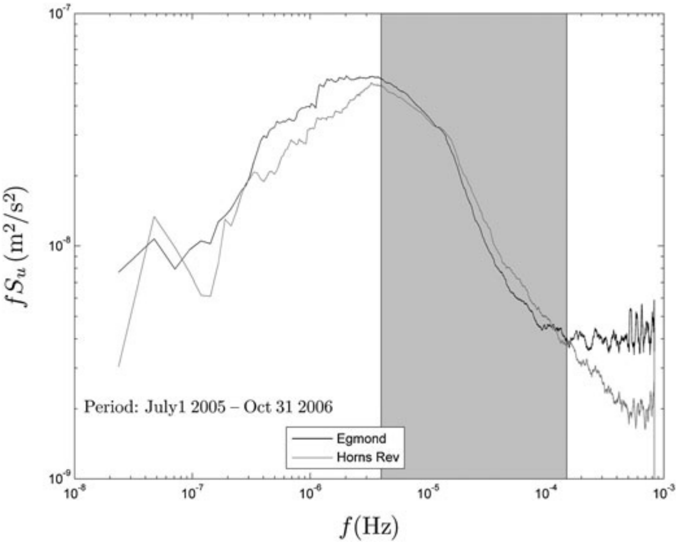

Figure 11. Comparison of the pre-multiplied horizontal wind speed power spectra between OWEZ (Egmond) and HR. The gray patch shows the timescales of the order of hours. Data from all wind directions are used.

is expected. Furthermore, at high frequencies, the wakes generated by the turbines contribute to the increase in spectral energy at OWEZ because of the proximity of the wind turbines as compared with that at HR. The spectral energy at OWEZ is higher than at HR likely because the meteorological mast at OWEZ is closer to and has a large wind sector covered by the wind farm as compared with that at HR (Figure 2). The poor comparison at very low frequencies (order of months) results from the very small number of estimates of the power density.

5. DISCUSSION AND CONCLUSION

Atmospheric stability and wind profile climatology are compared over a long marine fetch at the two sites in the North Sea separated by about 400 km. It is observed that within a long marine fetch, atmospheric stability in the North Sea is dominated by unstable and neutral conditions. Very stable conditions occur rarely ($<$ 1 and 2% at OWEZ and HR, respectively). This result is in agreement with the previous analysis of Coelingh *et al.* for the Dutch part[15] and of Floors[34] for the Danish part of the North Sea. There are differences in the climatology at the two locations within the North Sea. At OWEZ, more unstable conditions are observed as compared with that at HR and vice versa for stable conditions.

There is no significant daily variation of atmospheric stability conditions at both sites, but the heat capacity of water causes a seasonal variation. For high wind speeds, near-neutral conditions are more dominant. A systematic increase of unstable conditions from the south-west to north-west direction at both sites is observed. A different stability classification has also been suggested previously,[15,17] and its use would increase the number of stable conditions considerably. In the future, it would be interesting to arrive at a firm criterion to classify L. Currently, the criterion for selecting the intervals of L is only based on previous research experience.

Non-dimensional wind profiles have been compared at both sites, and the measurements agree well with the surface-layer theory in unstable and neutral conditions. For stable conditions, surface-layer theory overpredicts the wind speed with increasing heights at OWEZ. This is not observed at HR likely because of lower measurement heights. In order to assess the influence of z_i on the wind profile, the theory from Gryning *et al.*[18] is used at OWEZ. This introduces a new parameter, L_{MBL}. The comparison of the theoretical profiles with the observations at OWEZ, scaled with z_i only and a combination of z_i and L_{MBL}, shows better agreement (see Table VI) than that of traditional surface-layer theory. Under stable conditions, the wind profiles should definitely be scaled by z_i, and preferably, L_{MBL} might be applied as another scaling parameter. A comparison of the wind speed spectrum at both sites revealed that the low-frequency events (of the order of hours) are comparable. This provides a link between the two sites and shows that the two sites are quite similar.

This analysis will aid the wind farm developers to estimate the power production of wind turbines. The influence on the loads of the wind turbines is still a research question. This study is limited to the long marine fetch sector only (225–315°). A separate study is required to account for coastal effects and wind turbine wakes.

ACKNOWLEDGEMENTS

The data from the Offshore Wind farm Egmond aan Zee (OWEZ) were kindly made available by NoordZeewind as part of the PhD project under the Research Program WE@Sea. The data from Horns Rev were kindly provided by Vattenfall A/S and DONG energy A/S as part of the 'Tall Wind' project, which is funded by the Danish Research Agency, the Strategic Research Council, Program for Energy and Environment (Sagsnr. 2104-08-0025). Funding from the EU project, contract TREN-FP7EN-219048 'NORSEWinD' is also acknowledged. The authors also want to thank Claire Vincent from Risø DTU for clarifying the uncertainty analysis in the estimation of L.

REFERENCES

1. IEC. Wind turbines—design requirements. *IEC 61400-1*, International Electrotechnical Commission, 2005.
2. Gryning S-E, van Ulden P, Larsen RE. Dispersion from a continuous ground-level source investigated by a K model. *Quarterly Journal of the Royal Meteorological Society* 1983; **109**: 355–364.
3. Lange B, Larsen S, Højstrup J, Barthelmie R. Importance of thermal effects and sea surface roughness for offshore wind resource assessment. *Journal of Wind Engineering and Industrial Aerodynamics* 2004; **92**: 959–988. DOI: 10.1016/j.jweia.2004.05.005.
4. Sathe A, Bierbooms W. Influence of different wind profiles due to varying atmospheric stability on the fatigue life of wind turbines. *Journal of Physics: Conference Series* 2007; **75**: 012056. DOI: 10.1088/1742-6596/75/1/012056.
5. Monin AS, Obukhov AM. Basic laws of turbulent mixing in the atmosphere near the ground. *Trudy Akademiia Nauk SSSR Geofizicheskogo Instituta* 1954; **24**: 163–187.
6. Businger JA, Wyngaard JC, Izumi Y, Bradley EF. Flux–profile relationships in the atmospheric surface layer. *Journal of the Atmospheric Sciences* 1971; **28**: 181–189.
7. Charnock H. Wind stress over a water surface. *Quarterly Journal of Royal Meteorological Society* 1955; **81**: 639–640.
8. Kahma KK, Calkoen CJ. Reconciling discrepancies in the observed growth of wind-generated waves. *Journal of Physical Oceanography* 1992; **22**: 1389–1405.
9. Johnson HK, Højstrup J, Vested HJ, Larsen SE. On the dependence of sea surface roughness on wind waves. *Journal of Physical Oceanography* 1998; **28**: 1702–1716.
10. Dyer AJ. A review of flux–profile relationships. *Boundary-Layer Meteorology* 1974; **7**: 363–372. DOI: 10.1007/BF00240838.
11. Högstrom U. Nondimensional wind and temperature profiles in the atmospheric surface layer. *Boundary-Layer Meteorology* 1988; **42**: 55–78.
12. Grachev AA, Fairall CW, Bradley EF. Convective profile constants revisited. *Boundary-Layer Meteorology* 2000; **94**: 495–515.
13. Walmsley JL. On theoretical wind-speed and temperature profiles over the sea with applications to data from Sable Island, Nova Scotia. *Atmosphere-Ocean* 1988; **26**: 203–233.
14. van Wijk AJM, Beljaars ACM, Holtslag AAM, Turkenburg WC. Evaluation of stability corrections in wind speed profiles over the North Sea. *Journal of Wind Engineering and Industrial Aerodynamics* 1990; **33**: 551–566.
15. Coelingh JP, van Wijk AJM, Holtslag AAM. Analysis of the wind speed observations over the North Sea. *Journal of Wind Engineering and Industrial Aerodynamics* 1996; **61**: 51–69.
16. Lange B, Larsen S, Højstrup J, Barthelmie R. The influence of thermal effects on the wind speed profile of the coastal marine boundary layer. *Boundary-Layer Meteorology* 2004; **112**: 587–617.
17. Motta M, Barthelmie RJ. The influence of non-logarithmic wind speed profiles on potential power output at Danish offshore sites. *Wind Energy* 2005; **8**: 219–236.
18. Gryning SE, Batchvarova E, Brümmer B, Jørgensen H, Larsen S. On the extension of the wind profile over homogeneous terrain beyond the surface layer. *Boundary-Layer Meteorology* 2007; **124**: 251–268. DOI: 10.1007/s10546-007-9166-9.

19. Peña A, Hasager CB, Gryning SE, Courtney M, Antoniou I, Mikkelsen T. Offshore wind profiling using light detection and ranging measurements. *Wind Energy* 2009; **12**: 105–124. DOI: 10.1002/we.283.
20. Peña A, Gryning SE. Charnock's roughness length model and non-dimensional wind profiles over the sea. *Boundary-Layer Meteorology* 2008; **128**: 191–203.
21. Peña A, Gryning SE, Hasager CB. Measurement and modelling of the wind speed profile in the marine atmospheric boundary layer. *Boundary-Layer Meteorology* 2008; **129**: 479–495. DOI: 10.1007/s10546-008-9323-9.
22. Garratt JR. Review of drag coefficients over oceans and continents. *Monthly Weather Review* 1977; **105**: 915–929.
23. Peña A, Gryning SE, Mann J, Hasager CB. Length scales of the neutral wind profile over homogeneous terrain. *Journal of Applied Meteorology and Climatology* 2010; **49**: 792–806. DOI: 10.1175/2009JAMC2148.1.
24. Seibert P, Beyrich F, Gryning SE, Joffre S, Rasmussen A, Tercier P. Review and intercomparison of operational methods for the determination of the mixing height. *Atmospheric Environment* 2000; **34**: 1001–1027.
25. Peña A, Gryning SE, Hasager CB. Comparing mixing-length models of the diabatic wind profile over homogeneous terrain. *Theoretical and Applied Climatology* 2010; **100**: 325–335. DOI: 10.1007/s10546-008-9323-9.
26. Emeis S, Münkel C, Vogt S, Müller WJ, Schäfer K. Atmospheric boundary-layer structure from simultaneous SODAR, RASS, and ceilometer measurements. *Atmospheric Environment* 2004; **38**: 273–286. DOI: 10.1016/j.atmosenv.2003.09.054.
27. Fairall CW, Bradley EF, Godfrey JS, Wick GA, Edson JB. Cool skin and warm layer effects on sea surface temperature. *Journal of Geophysical Research* 1996; **101**: 1295–1308.
28. Sathe A. Project site data—OWEZ data analysis. *We@Sea Report*, Technical University Delft, 2009.
29. Holtslag AAM. Estimates of diabatic wind speed profiles from near-surface observations. *Boundary-Layer Meteorology* 1984; **29**: 225–250.
30. Berkowicz R, Prahm LP. Evaluation of the profile method for the estimation of the surface fluxes of momentum and heat. *Atmospheric Environment* 1982; **16**: 2809–2819.
31. Grachev AA, Fairall CW. Dependence of the Monin–Obukhov stability parameter on the bulk Richardson number over the ocean. *Journal of Applied Meteorology* 1996; **36**: 406–414.
32. Sørensen PB. Wake effect east of the Horns Rev offshore wind farm. *Technical Report* 209918, Elkraft System. Elsam Engineering, 2005.
33. Vincent CL, Pinson P, Giebel G. Wind fluctuations over the North Sea. *International Journal of Climatology* 2010. DOI: 10.1002/joc.2175.
34. Floors R. Analysis of diabatic flow modification in the internal boundary layer. *Master's Thesis*, Wageningen University, March 2010.

Chapter 3

Influence of diabatic wind profiles on wind turbine loads

In chapter 2 we analyzed wind profiles that are one of the main inputs in load calculations. There is some overlap of the theory described in this paper and that described in chapter 2. One way to reducing wind turbine costs is to optimize the design. Load calculations are an integral part of the design process and are currently performed based on the IEC [2005a] standard. The description of the input wind field in this standard is based on several models or empirical results that are built on many different assumptions. The overall result is that the load calculations are performed in a non-optimum environment. This necessitates the use of large safety factors that results in excessive use of materials thus increasing the costs significantly. There are opportunities to optimize the load calculations by describing the input wind field in a more realistic manner.

In this chapter load calculations are performed using the aer-elastic simulation tool Bladed. The standard surface-layer diabatic wind profile model based on the Monin-Obukhov similarity theory [Monin and Obukhov, 1954] is used in describing the input wind conditions. The wind field is considered to be steady and the only asymmetry resulting in the input wind field is due to the wind profile. Fatigue damage is obtained at the blade root as a result of loading due to wind profiles. The influence of using different stability distributions is also demonstrated. The results obtained provided an impetus to carry out a detail fatigue damage study under diabatic conditions by combining wind profiles and turbulence.

The Science of Making Torque from Wind IOP Publishing
Journal of Physics: Conference Series **75** (2007) 012056 doi:10.1088/1742-6596/75/1/012056

Influence of different wind profiles due to varying atmospheric stability on the fatigue life of wind turbines

Ameya Sathe, Wim Bierbooms
DUWIND- Delft University Wind Energy Research Institute, Kluyverweg 1, 2629 HS Delft, NL
E-mail: `A.R.Sathe@tudelft.nl`

Abstract.
Offshore wind energy is being developed on a very large scale in the European seas. The objective of developing wind energy offshore is to capture greater wind speeds than are encountered onshore and as a result more energy. With this also come more challenges in the design of wind turbines due to the hostile offshore environment. Currently the standards for offshore wind turbines prescribe a site specific design for the support structures and the design for the rotor nacelle assembly according to onshore standards. Wind turbines are designed to withstand fatigue and ultimate loads. For the fatigue loading several input conditions have been prescribed, amongst which wind profile is one of them. Wind profile is represented by power law or logarithmic law as given in the standards. A neutral stability of the atmosphere is considered while obtaining the wind profile using the logarithmic law. In this paper the atmospheric stability is varied in order to estimate different wind profiles and simulations are run in Bladed to check its influence on the fatigue damage at the blade root. The variations in the atmospheric stability has been taken into account by using some typical values of Obukhov length. From steady state simulations it has been found that atmospheric stability is important for fatigue damage. The analysis showed that variation in the distribution of atmospheric stability causes large variations in the fatigue damage for different sites. Thus, it is worthwhile to carry out a full scale study using the turbulent winds and real data for wind turbine and environmental conditions.

1. Introduction

Offshore wind energy is on a rapid expansion in Europe and many offshore wind farms are being built. This preludes further development of offshore wind farms all around the world. A wind turbine is subjected to various kinds of loads originating from different sources. Aerodynamic loads is one of the sources of loads on wind turbines. These loads occur due to various input environmental states that a wind turbine has to encounter. Wind shear is one of the environmental state that occurs all the time during the lifetime of a turbine. It is an important parameter which causes cyclic loading in the rotor and hence fatigue damage. Wind shear is extrapolated from measurements done at lower heights to a height z as given by logarithmic law.

$$u_z = \frac{u_*}{k} ln\left(\frac{z}{z_0}\right) \tag{1}$$

where u_* is the friction velocity, k is the von Karman constant and z_0 is the roughness length. Wind shear is also given by the power law as:

$$\frac{u_z}{u_{z_r}} = \left(\frac{z}{z_r}\right)^{\alpha} \tag{2}$$

where α is the power exponent, u_{z_r} is the reference velocity and z_r is the reference height. Equations 1 and 2 assume a neutral stability of the atmosphere while extrapolating to different heights. Offshore wind farms are being planned for wind turbines with large rotor diameters. This poses a particular question on the viability of using neutral stability to obtain wind shear from a reference height. Previous studies [1], [2] and [3] have shown that the energy yield estimates differ when stability is taken into consideration. In this paper the effects of stability classes have been ascertained on the fatigue damage at the blade root. The resulting damage is compared with the fatigue damage obtained from logarithmic and exponential wind shear. The exponential wind shear is obtained using a power law exponent of 0.14 for offshore sites as given in [4].

During the course of the day, cooling and heating of the surface takes place causing different stability conditions and hence different stratifications. According to Monin-Obukhov similarity theory the atmospheric stability can be described in terms of stability parameter z/L, where L is the Obukhov length. Taking stability into account, equation 1 can be written as,

$$u_z = \frac{u_*}{k}\left[ln\left(\frac{z}{z_0}\right) - \psi\left(\frac{z}{L}\right)\right] \tag{3}$$

where $\psi\left(\frac{z}{L}\right)$ is the stability parameter. The stability parameter can be calculated using the Bussinger-Dyer formulation [5]

$$\psi = 2ln\left(\frac{1+\phi_m}{2}\right) + ln\left(\frac{(1+\phi_m^2)}{2}\right) - 2tan^{-1}(x) - \frac{\pi}{2} \quad for\frac{z}{L} < 0 \tag{4}$$

$$\psi = -\beta\frac{z}{L} \quad for\frac{z}{L} > 0 \tag{5}$$

where β and γ are the empirical parameters whose values are taken as 4.8 and 19.3 respectively, [6]. From the wind speed at reference height z_r, the wind speed at height z can be obtained from equation 3,

$$u_z = u_{z_r}\frac{ln(\frac{z}{z_0}) - \psi(\frac{z}{L})}{ln(\frac{z_r}{z_0}) - \psi(\frac{z_r}{L})} \tag{6}$$

In this paper the values of L have been assumed from the classification of stability into five categories given in [7].

Table 1. Classification of stability according to Obukhov lengths

very stable	0<L<200 m
stable	200<L<1000 m
near-neutral	$\mid L \mid$ >1000 m
unstable	-1000<L<-200 m
very unstable	-200<L<0 m

The sea surface roughness z_0 is also not constant and varies with time. Previous studies [1] and [2] have shown that the effect of sea surface roughness is not significant and hence in this paper, for the analysis, its value is taken as constant. Nevertheless, two extreme values of z_0 are assumed and its influence on fatigue damage estimated to verify its influence.

2. Description of the work

The design software used for the fatigue analysis is 'Bladed' developed by Garrad Hassan and Partners Ltd. It is a complete design software and an industry standard, which has been validated by Germanischer Llyod. The wind turbine used is a reference turbine which was prepared for a research project at DUWIND. The characteristics of the turbine are summarized in table 2.

Table 2. Turbine properties

Class I turbine, Mean wind speed = 10 m/s
Power = 5.5MW
Rotor Diameter = 129m
Hub Height = 95m
Number of Blades = 3
Rotational speed = Variable speed
cut in wind speed, v_{cut-in} = 4 m/s
cut out wind speed, $v_{cut-out}$ = 25 m/s

As given in table 2, the turbine has a large rotor diameter and is suited for the analysis of stability influence. The fatigue analysis is carried out for the blade root section. Blade root is selected as the section because it experiences maximum bending moments due to cyclic loading as compared to any other section on the blade. The blade root is modeled as a thin annular cylinder with an outer diameter of $3.5m$ and inner diameter of $3.42m$. The material for the blade is assumed as Glass Epoxy with an inverse slope on the log-log S-N curve as 9 and an intercept of $70Mpa$. The reference height is taken as hub height based on which wind shear across the rotor plane is determined. A wind turbine's life has been assumed as 20 years [8] and fatigue damage has been estimated for different stability classes and compared with the fatigue damage obtained using exponential and logarithmic wind shear assuming a neutral profile. The simulations have been run for steady conditions. The choice of the steady wind conditions for the simulation may not represent the real situation but the analysis would nevertheless give a primary insight into the importance of atmospheric stability. Also, if the steady conditions would not have a significant effect on the fatigue damage then it may not be worthwhile to go for a full scale study using turbulent winds. Apart from the wind conditions, tower shadow effects, gravity and inertia loads have also been taken into account. This allows for the simulation time to be reduced from the standard specified 600s [8] to a value representing a minimum of one complete cycle of loading. Considering that the turbine is a variable speed turbine the minimum simulation time should at least be greater than the time required for one revolution of the rotor at minimum wind speed, i. e. $4m/s$. The rotor speed at $4m/s$ was found to be $4rpm$ and hence the simulation time should be more than $15s$. Nevertheless, the simulation time has been chosen as $90s$ covering 6 cycles of revolution. Thus it is sufficient to cover even the slowest revolution of the rotor. A pre-analysis of the effect of varying z_0 on the fatigue life was carried out to ascertain if its variability would be important. According to DNV offshore standards [9], z_0 can vary from 0.0001 for calm sea to 0.003 for coastal waters with the wind blowing from land to sea. With time, z_0 would at most vary in the two extreme values. Table 3 shows the influence of varying z_0 on the fatigue damage at blade root.

As seen from table 3 there is some influence of z_0 on the fatigue damage. In reality z_0 would not attain a fixed value on either side of extremes but would at most hover from one extreme to the other depending on the wind and site conditions. This would reduce the difference in

Table 3. Fatigue Damage for different sea surface roughness

Roughness	Fatigue Damage
0.003	0.37
0.0001	0.13

the fatigue damage obtained for two extreme z_0 values as shown in table 3. Hence its variation is not accounted for in this paper but could be worthwhile to study using real data. For this paper z_0 is taken as 0.001 assuming that the site would be a coastal site. The combinations for simulations are made using the wind speed bins of $1m/s$ from v_{cut-in} to $v_{cut-out}$ for a z_0 value of 0.001 and various values of L as given in table 1. Table 4 summarizes the combination of simulations.

Table 4. Simulation parameters

Obukhov Length, L					Wind speeds	Roughness, z_0
-300	-100	∞	100	300	v_{cut-in} - $v_{cut-out}$	0.001

The wind shears for a wind speed of $10m/s$ is given in figure 1 as an example.

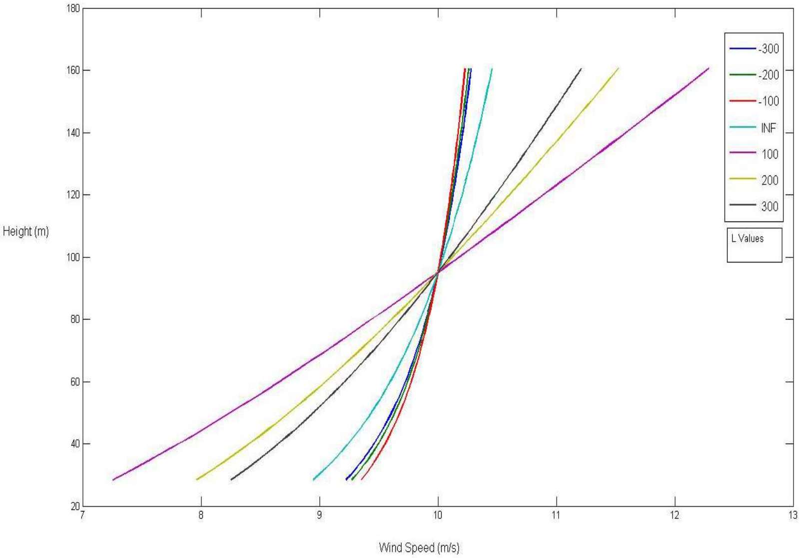

Figure 1. Wind shear for different stability conditions at $10m/s$

To check the influence of stability, it is important to assume a distribution to be able to assess its effect. Hence, distribution of a particular stability condition sampled by wind speeds is taken into consideration. [2] gives stability distributions found for various Danish sites. In this paper the distributions are taken from [2] for Rodsand and Vindeby sites and fatigue damage ascertained. Figures 2 and 3 show the distribution of stability conditions sampled by wind speed.

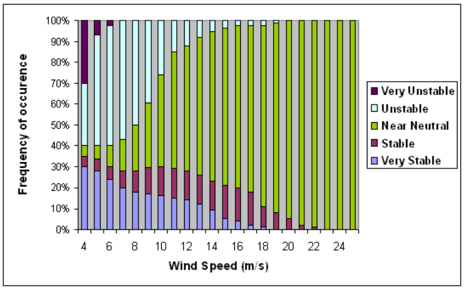

Figure 2. Frequency of occurrence of stability conditions sampled by wind speed for Rodsand site[2]

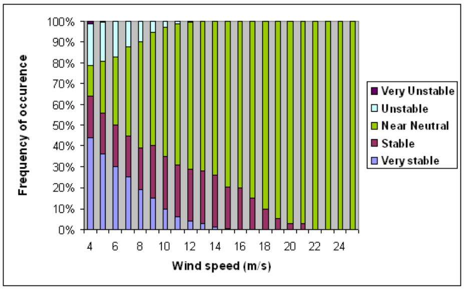

Figure 3. Frequency of occurrence of stability conditions sampled by wind speed for Vindeby site[2]

These sites are chosen without any special preference as any other offshore site could also have been chosen for the analysis. As given in table 4, several simulations were run to calculate the bending moments at the blade root. The time histories of bending moments were converted into stress histories using the following relation:

$$\sigma = \frac{M.y}{I} \tag{7}$$

where σ is the stress at the blade root at a particular time, M is the bending moment, y is the distance at which the moment acts, which is the radius of the outer diameter and I is the moment of inertia of annular cylinder.

3. Results

Figure 4 shows different stress histories for different stability cases for a wind speed of $10m/s$. The figure is just an illustration of various stress histories obtained for various wind speeds and stability classes. The number of cycles to failure and subsequently the fractional damage is calculated using the following log-log relationship:

$$log(S) = log(K) - \frac{1}{m}log(N) \tag{8}$$

where S is the stress amplitude in Mpa, $log(K)$ is the intercept, $\frac{1}{m}$ is the inverse slope and N is the number of cycles to failure. The fatigue damage using different stability classes is calculated using following relation:

$$D = \frac{20 \times 365 \times 24 \times 3600}{90} \sum_{U=4}^{25} \sum_{L=1}^{5} P(U)_L \times d(U)_L \times P(U) \tag{9}$$

where D is the fatigue damage at the blade root, U is the bin average wind speed, $\sum_{L=1}^{5}$ represents five stability classes given in table 1, $P(U)_L$ is the probability of occurrence of a stability class

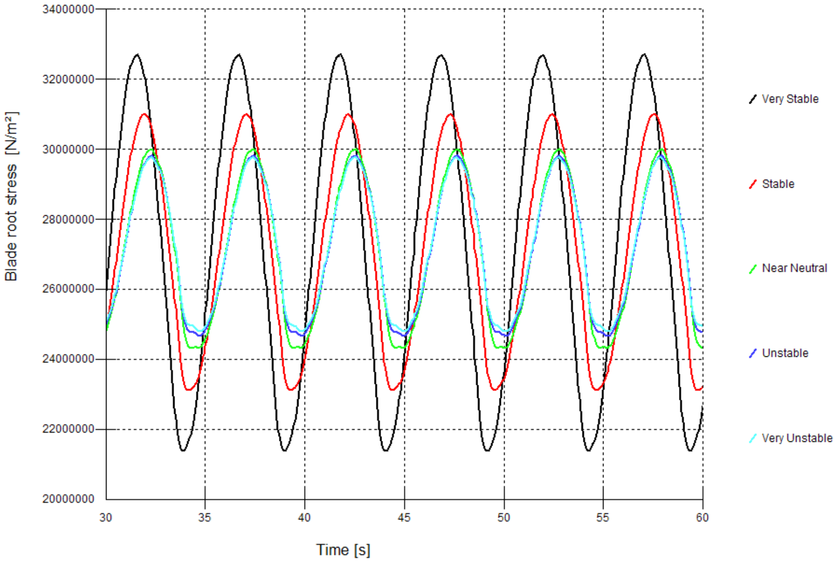

Figure 4. Stress histories for different stability conditions at $10m/s$

sampled by wind speeds, $d(U)_L$ is the fractional damage for the simulation time for respective stability class at a particular wind speed and $P(U)$ is the probability of occurrence of a particular wind speed. Since the simulations have been performed for $90s$ the resulting fatigue damage has been divided by this simulation time. Table 5 summarizes the results obtained from the simulations.

Table 5. Lifetime fatigue damage using different wind shear models

Method used	Fatigue Damage
Wind shear considering stability classes for Rodsand site	6.12
Wind shear considering stability classes for Vindeby site	1.68
Wind shear modeled by logarithmic law and neutral stability	0.25
Wind shear modeled by exponential law	1.91

As seen in table 5, the lifetime fatigue is considerably affected by using different models of wind shear. The distribution of stability shows a significant change in the fatigue damage. For Rodsand site the fatigue damage is considerably higher than for Vindeby site. The wind shear modeled using logarithmic law gives the lowest fatigue damage.

4. Conclusions

As seen in table 5, considering stability classes while modeling wind shear is an important factor in assessing the fatigue damage more accurately. The importance of distribution of stability classes is clearly emphasized in the results. It can be concluded from the above results that logarithmic wind shear with neutral stability underpredicts the fatigue damage depicting a non-conservative approach. It could have been contested that the occurrence of different stability conditions would tend to average out the effects over time but the results do not show this behavior. Two factors are dependent on it:

- Differences in the wind shears for various stability conditions.
- Frequency of occurrence of a particular stability condition.

Figure 1 shows that the difference in the wind velocities at the lowermost part of the rotor and the uppermost part for a very stable condition can be up to $5m/s$ for a hub height velocity of $10m/s$. This difference increases for a greater hub height velocity and with the increase in rotor diameter. This is a significant difference in the wind speed as compared to that obtained from the logarithmic law considering only neutral stability. The importance of a stability is certainly evident in the difference between the fatigue damage obtained at two sites.
Although the results have been obtained for steady state simulations, it provides an impetus to carry out a full scale fatigue damage study by using turbulent winds and real data for wind turbines and environmental conditions.

References

[1] Bernhard Lange, Søren Larsen, Jørgen Højstrup, and Rebecca Barthelmie. Importance of thermal effects and sea surface roughness for offshore wind resource assessment. *Journal of Wind Engineering and Industrial aerodynamics*, pages 959–988, May 2004.

[2] M.Motta and R.J.Barthelmie. The influence of non-logarithmic wind speed profiles on potential power output at danish offshore sites. *Wind Energy*, pages 219–236, 2005.

[3] Jonathan Summer and Christian Masson. Influence of atmospheric stability on wind turbine power performance curves. *Journal of Solar Energy Engineering*, 128:531–538, November 2006.

[4] IEC 61400-3. Offshore wind turbines-part 1: Design requirements. 2005.

[5] Roland B. Stull. *An Introduction to Boundary Layer Meteorology.* Kluwer Academic Publishers, 1988.

[6] U.Högstrom. Nondimensional wind and temperature profiles in the atmospheric surface layer. *Boundary-Layer Meteorology*, pages 55–78, 1988.

[7] Van Wijk AJM, Beljaars ACM, Holtslag AAM, and Turkenburg WC. Evaluation of stability corrections in wind speed profiles over the north sea. *Journal of Wind Engineering and Industrial Aerodynamics*, pages 551–566, 1990.

[8] IEC 61400-1. Wind turbines-part 1: Design requirements. 2005.

[9] DNV Det Norske Veritas. Design of offshore wind turbine structures. June 2004.

[10] Bernhard Lange, Søren Larsen, Jørgen Højstrup, and Rebecca Barthelmie. The influence of thermal effects on the wind speed profile of the coastal marine boundary layer. *Boundary-Layer Meteorology*, pages 587–617, 2004.

Chapter 4

Influence of atmospheric stability on wind turbine loads

Having studied the influence of diabatic wind profiles under steady wind conditions on wind turbine loads in chapter 3 the next obvious step was to perform a full scale load calculation that included the combined influence of diabatic wind profiles and turbulence. The theory of wind profiles described in this chapter is an overlap of that described in chapter 2. The load calculations are carried out for the case of normal power production. The aim of this chapter is to answer the following research questions:

1. Are wind turbine loads influenced by atmospheric stability?
2. Are wind turbine loads influenced by wind profile models?
3. Are the IEC [2005a] loads different from those calculated using site-specific diabatic wind profile and turbulence?

Two wind profile models are used. One is the standard surface-layer diabatic wind profile model, and the second is the more advanced Gryning et al. [2007] model that is valid for the entire boundary layer. Turbulence is quantified using the Mann [1994] model, where the model parameters under diabatic and neutral conditions are obtained by fitting the model with the measurements at a flat terrain test site in Denmark. In order to compare the influence of wind speed and stability distributions on the loads, four different sites are chosen. The wind profiles and turbulence obtained at only one site are applied at all other sites. The load calculations are performed using an aero-elastic simulation tool HAWC2, developed at Risø DTU in Denmark. Fatigue loads are obtained at the blade root, tower base and the hub.

WIND ENERGY
Wind Energ. 0000; **00**:1–23
DOI: 10.1002/we

RESEARCH ARTICLE

Influence of atmospheric stability on wind turbine loads

A. Sathe[**+], J. Mann[**], T. Barlas[**], W.A.A.M. Bierbooms[+], G.J.W. van Bussel[+]

[**] Wind Energy Division, Risø DTU, Frederiksborgvej 399, 4000 Roskilde, Denmark
[+] TU Delft, Kluyverweg 1, 2629 HS Delft, The Netherlands

ABSTRACT

Simulations of wind turbine loads for the NREL 5 MW reference wind turbine under diabatic conditions are carried out. The diabatic conditions are incorporated in the input wind field in the form of wind profile and turbulence. The simulations are carried out for mean wind speeds between 3 – 16 m/s at the turbine hub height. The loads are quantified as the cumulative sum of the damage equivalent load for different wind speeds that are weighted according to the wind speed and stability distribution. Four sites with a different wind speed and stability distribution are used for comparison. The turbulence and wind profile from only one site is used in the load calculations which are then weighted according to wind speed and stability distributions at different sites. It is observed that atmospheric stability influences the tower and rotor loads. The difference in the calculated tower loads using diabatic wind conditions and those obtained assuming neutral conditions only is up to 17%, whereas the difference for the rotor loads is up to 13%. The blade loads are hardly influenced by atmospheric stability, where the difference between the calculated loads using diabatic and neutral input wind conditions is up to 3% only. The wind profiles and turbulence under diabatic conditions have contrasting influences on the loads, e.g. under stable conditions, loads induced by the wind profile are larger due to increased wind shear, whereas those induced by turbulence are lower due to less turbulent energy. The tower base loads are mainly influenced by diabatic turbulence, whereas the rotor loads are influenced by diabatic wind profiles. The blade loads are influenced by both, diabatic wind profile and turbulence, that leads to averaging of the loads. The importance of using a detailed boundary-layer wind profile model is also demonstrated. The difference in the calculated blade and rotor loads is up to 6% and 8% respectively, when only the surface-layer wind profile model is used in comparison to those obtained using a boundary-layer wind profile model. Finally, comparison of the calculated loads obtained using site-specific and IEC wind conditions is carried out. It is observed that the IEC loads are up to 95% larger than those obtained using site-specific wind conditions. Copyright © 0000 John Wiley & Sons, Ltd.

KEYWORDS

Atmospheric stability, Wind Profile, Turbulence, Wind turbine loads

Correspondence

[**] Wind Energy Division, Risø DTU, Frederiksborgvej 399, 4000 Roskilde, Denmark, E-mail: amsat@risoe.dtu.dk

Received . . .

1. INTRODUCTION

Wind turbines are designed to withstand fatigue and extreme loads during their lifetime of approximately 20 years [1]. Amongst different factors that cause fatigue loading, atmospheric turbulence and wind profile have a significant influence.

Prepared using weauth.cls [Version: 2010/06/17 v1.00]

The IEC standards [1] prescribe a range of wind conditions between the cut-in and cut-out wind speeds under which the turbine has to operate. Also, a power law wind profile model with a fixed value of the exponent is prescribed. Turbulence is defined by either the Kaimal model [2], or the more recent Mann model [3]. No consideration to atmospheric stability is given in the [1] standard neither in the wind profile nor the turbulence model. The [1] standards are known to give a conservative estimate of the loads. In this study we attempt to answer the following research questions:

1. Are wind turbine loads influenced by wind profile models?
2. Are wind turbine loads influenced by atmospheric stability?

Two diabatic wind profile models are investigated, the first is using the standard surface-layer scaling according to Monin-Obukhov theory [4], and the second is using the more advanced theory developed by [5] that connects the surface layer scaling with the geostrophic drag law. Turbulence is simulated using the Mann model under different atmospheric stabilities. The time-domain aeroelastic code HAWC2 is utilized for the calculation of the loads on various components of the wind turbine. Fatigue loads are quantified using the concept of Damage Equivalent Loads (DEQ), which for a given arbitrary number of load cycles would produce the same fatigue damage as that of the sum of the individual load cycles. Simulations are used to compare the load cases.

The investigation of diabatic wind profile models has been a subject of research since the 1950s. The logarithmic wind profile with a stability correction term has been used in many research projects. The stability corrections have also been subject of extensive research [6, 7]. The model is however strictly applicable only in the surface layer, which is roughly the lower 10% of the atmospheric boundary layer. It is well known that the boundary layer height varies according to atmospheric stability, where it is typically between 600 – 1000 m under unstable conditions and 150 – 200 m under stable conditions [8]. Modern wind turbines extend up to 150 m, which means that they operate in and above the surface layer. We thus need wind profile models that extend up to the the entire boundary layer height. [9, 10] proposed a wind shear model under neutral conditions that extend up to the entire boundary layer height. [11] extended this model to all atmospheric stability conditions using the Rossby number similarity theory. Recently, [5] proposed a new diabatic wind profile model that extends up to the entire boundary layer height, also using the Rossby number similarity theory. The main difference between these models and the surface-layer model is the inclusion of the boundary layer height parameter that limits the growth of the wind profile length scale above the surface layer. In this study, we use the model from [5], since the performance of [9, 10] was similar to [5] when compared with the measurements [11].

For wind turbines we need two-point statistics in order to simulate turbulent wind fields that affects the entire wind turbine. Thus we either need a three-dimensional spectral tensor model or combine the one-dimensional spectra with some coherence model. Different spectral tensor models have been proposed in the past [12, 13] but the IEC standards recommend the Mann model [3] since it incorporates the atmospheric physics to the best possible extent. The starting point for these models is the isotropic spectral tensor model by [14]. Alternatively the expressions by [2] for the one-dimensional spectra are recommended to be used with a some coherence model, e.g. [15]. In principle all these models are valid only under neutral conditions in the surface layer. [16] derived analytical expressions of spectral tensors also under stable conditions. Due to unavailability of spectral tensor models under unstable conditions and non-stationarity of the model by [16], we use the Mann model [3] by fitting the model parameters to the data under different stability conditions.

There have been a few studies concerning the influence of the wind conditions on wind turbine loads. [17] studied the complex terrain effects on turbulence and subsequently on wind turbine loads, and concluded that increased fatigue loads were caused by increased turbulence. [18] carried out a linear multi-variable regression analysis and concluded that the vertical component of the wind field and atmospheric stability have a significant influence on blade DEQ. The wind shear and turbulence effects on rotor fatigue loads were studied by [19]. The wind profile is modelled using the power law and turbulence using the von-Kármán isotropic spectral tensor [14]. They concluded that the increase in wind shear and turbulence increased rotor fatigue loads considerably. [20] performed a statistical analysis of the influence of several primary and secondary inflow parameters including atmospheric stability. They used a sequential analysis of each parameter instead of multi-variable regression analysis and concluded that there is not much influence of atmospheric stability on fatigue and extreme loads of blades. In contrast [21] studied the influence of coherent turbulent structures induced by Kelvin-Helmholtz waves under very stable conditions on wind turbine loads and concluded that these large coherent structures have a significant influence on wind turbine loads. It should however be noted that the site chosen by [21] for their analysis is such that large coherent structures are observed quite often. [22] performed a parametric study of several inflow parameters and concluded that they do not influence the fatigue failure as much as the uncertainty in the material properties. Similar conclusions were made by [23], where a detailed investigation of wind turbine fatigue loads was carried out using a probabilistic approach. [24] calculated fatigue loads at the blade root using diabatic wind profiles and steady winds, and concluded that fatigue loads increase using diabatic wind profiles in comparison to those obtained under neutral conditions. [25] varied turbulence intensity and length scales to investigate their influence on wind turbine loads and concluded that variation in turbulence parameters have a negligible influence on blade and tower moments but a significant influence on the yaw moments. Recently, [26] investigated the influence of atmospheric turbulence on wind turbine rotor torque. The Gaussian and non-Gaussian turbulent time series were simulated using two different models and comparison with measurements was carried out. They concluded that non-Gaussian turbulence, which is also observed in the atmosphere significantly increases the loads.

Section 2 of this article gives a description of the sites and the measurements used. Section 3 describes the wind climate at different sites, giving the wind speed and stability distributions. Section 4 introduces some theory of the wind profile models and turbulence used in this work. Section 5 briefly explains the aero-elastic simulation tool used in this study. The load calculations are described in section 6. Finally, we conclude our work with some discussion in section 7.

2. SITE DESCRIPTIONS

Load calculations are performed based on turbulence and mean wind speed data at Høvsøre, which is the Danish National Test Center for Large Wind Turbines. Based on data availability the range of mean wind speeds chosen is 3 – 16 m/s. For estimating the cumulative load of all wind speeds the loads need to be weighted according to the joint wind speed and stability distribution. These distributions are specific to a particular site. Hence, we selected three additional sites with different distributions of the mean wind speed and atmospheric stability for comparing the cumulative fatigue loads. These sites are Egmond aan Zee in the Dutch North Sea, Östergarnsholm in the Baltic sea, and Hurghada in the Gulf of Suez, Egypt. For all sites we use the turbulence and wind profiles from Høvsøre, in order to isolate the effect of atmospheric stability.

2.1. Høvsøre

A reference meteorological mast (met-mast), which is 116.5 m tall and intensively equipped with cup and sonic anemometers, is located at the coordinates $56^\circ 26'26''$ N, $08^\circ 09'03''$ E. The site is about 2 km from the West coast of Denmark. The eastern sector is generally characterized by a flat, homogeneous terrain, and to the South is a lagoon. To the North, there is a row of five wind turbines. The sonics are placed on the North booms of the met-mast, resulting in unusable data when the wind is from the South because of the wake of the mast, and from the North because of the wakes of the wind turbines. In order to bin the wind speeds we use the cup anemometers at 80 and 100 m, since the hub height of the turbine is 90 m (refer table III). The data is selected between March 2004 – November 2009. To comply with terrain homogeneity we restrict our analysis to a directional sector of 50° – 150°. Atmospheric stability is characterized using the standard surface-layer length scale L, commonly known as the Monin-Obukhov length. L is estimated using the eddy covariance method [27] from the sonic measurements at 20 m. The aerodynamic roughness length $z_0 = 0.014$ cm. More details of the site and instrumentation can be found in [28].

2.2. Egmond aan Zee – OWEZ

A 116 m tall meteorological mast is located at about 18 km from the coast of Egmond aan Zee (henceforth referred to as OWEZ, the offshore wind farm Egmond aan Zee), The Netherlands, coordinates $52^\circ 36'22.9''$ N, $4^\circ 23'22.7''$ E. The depth of water is approximately 20 m. The stability analysis is carried out using the 10-min mean measurements between July 2005 – December 2008. In order to avoid turbine wakes and sudden change of roughness from the east, we use a directional sector of 225° – 315° such that homogeneous conditions prevail. The wind speed distribution is obtained from the cup anemometer measurements at 70 m. Atmospheric stability is estimated using the bulk Richardson number method [29] from the wind speed and temperature measurements at 21 m and the sea-surface temperature. More details of the site and instrumentation can be found in [30].

2.3. Östergarnsholm

A 30 m tall mast is located at a small island about 4 km east coast Gotland, in the Baltic Sea, coordinates $57^\circ 27'$ N, $18^\circ 59'$ E. The stability analysis is carried out using the eddy covariance method [27] from the sonic measurements at 9 m above the surface between June 1995 – July 2002. The island is very flat. For the directional sector 80° – 220° the data represents undisturbed open sea conditions, for the other sectors the wave field is influenced by limited fetch or bottom topography [31]. Since one the goals of this study is to assess the influence of atmospheric stability and wind speed distribution, and not to perform a detailed site specific study, all wind directions are used. The wind speed distribution is obtained from the cup anemometer measurements at 30 m. More details of the site and instrumentation can be found in [32, 33].

2.4. Hurghada

A 30 m tall mast is located at a coastal plateau about 650 m to the west of the Gulf of Suez, Egypt, coordinates $27^\circ 18' 59''$ N, $33^\circ 41' 56''$ E. The stability analysis is carried out using the profile temperature difference method [34]. The period of analysis is between March 1991 – November 1996. The measurements are the mean wind speed at 24 m and temperature difference at 22.5 m. The island is quite flat with a gentle slope to the South west that reaches about 300 m above sea level at a distance of 20 km. To the North West the terrain abruptly rises to about 200 m at a distance of 10 km. In order to avoid the sudden roughness change from the Red Sea, we select a directional sector of 135° – 330°. More details of the site and instrumentation can be found in [35].

3. WIND CLIMATE AND ATMOSPHERIC STABILITY

Table I. Weibull scale and shape parameters for different sites

	Scale (λ)	Shape (k)
Høvsøre	9.13	3.82
OWEZ	11.12	3.07
Östergarnsholm	7.86	2.18
Hurghada	6.56	2.70

Fig. 1 shows the histograms of the mean wind speeds at the four sites. The decrease in the mean wind speed at Östergarnsholm and Hurghada is evident by the shift in the distribution to the left in comparison to Høvsøre and OWEZ. When a Weibull distribution is fitted to the measurements at these sites, we obtain the scale (λ) and shape (k) parameters as given in table I. At Östergarnsholm and Hurghada these parameters are significantly smaller than those at Høvsøre and OWEZ. It would be ideal to obtain these measurements at 90 m at all four sites, however, they are not available. Another alternative is to extrapolate the wind at different heights to 90 m using some wind profile model. We do not opt for this because we are interested in having an indication of the influence of variability in site specific distributions on wind turbine loads and not to perform a detailed site specific analysis.

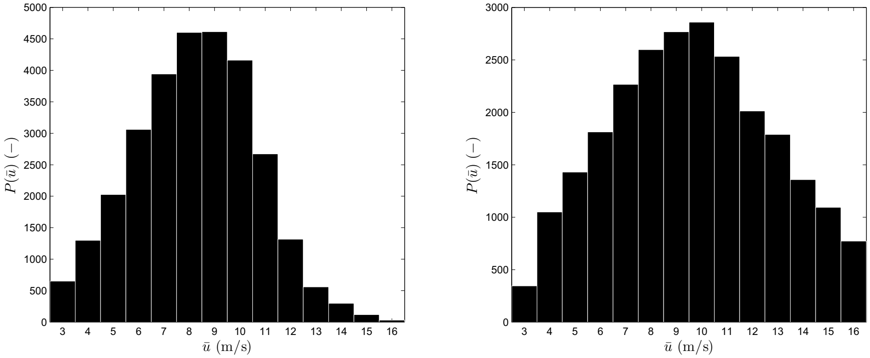

(a) Høvsøre **(b)** OWEZ

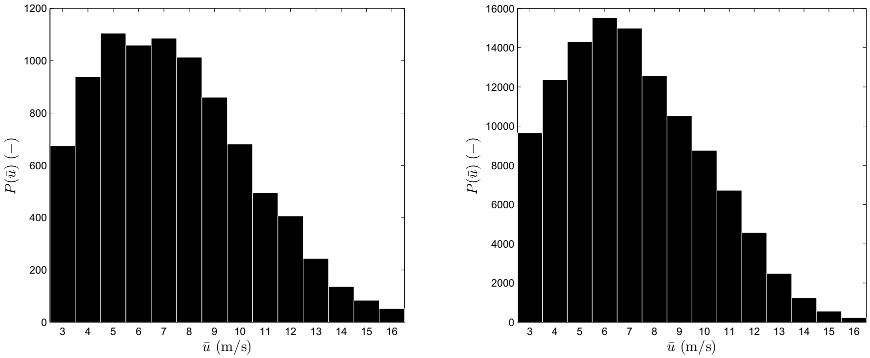

(c) Östergarnsholm **(d)** Hurghada

Figure 1. Histograms of wind speeds at different sites for the selected wind sectors

Except at Östergarnsholm, for each site we select a particular directional sector in order to comply with homogeneous site conditions. As a consequence the number of observations may reduce. In order to verify this we plot the wind rose at all four sites (Fig. 2). It is seen that except at Høvsøre the data selection is in the prevailing wind direction, but we have a sufficient number of 10-min observations at all sites. Atmospheric stability is classified into seven stabilities following [5], and is given in table II.

Table II. Classification of atmospheric stability according to Obukhov length intervals

very stable (vs)	$10 \leq L \leq 50$ m
stable (s)	$50 \leq L \leq 200$ m
near-neutral stable (nns)	$200 \leq L \leq 500$ m
neutral (n)	$\mid L \mid \geq 500$ m
near-neutral unstable (nnu)	$-500 \leq L \leq -200$ m
unstable (u)	$-200 \leq L \leq -100$ m
very unstable (vu)	$-100 \leq L \leq -50$ m

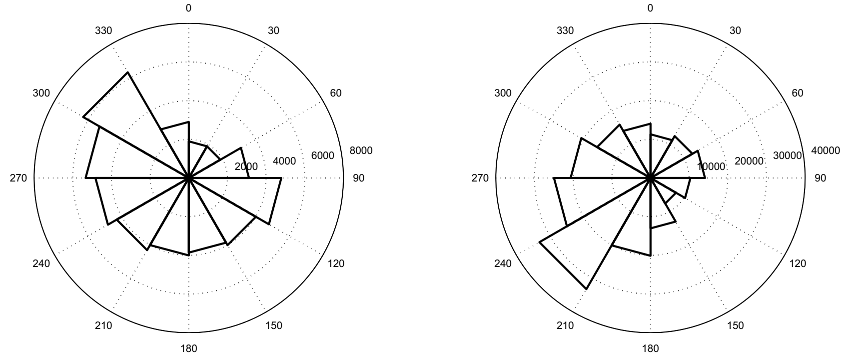

(a) Høvsøre

(b) OWEZ

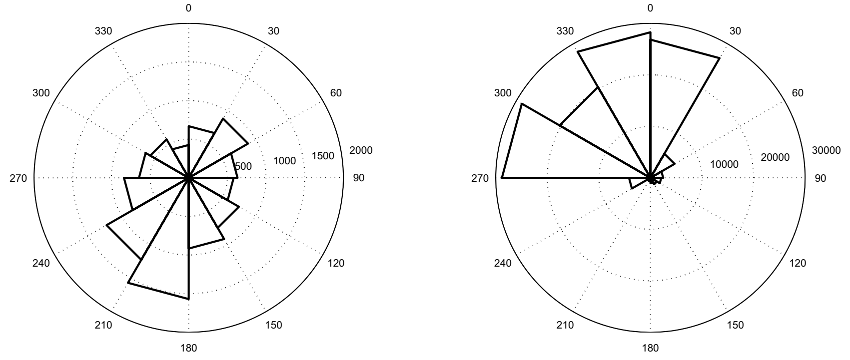

(c) Östergarnsholm

(d) Hurghada

Figure 2. Wind rose at different sites. The numbers outside the concentric circles are the number of observations at the respective sites.

Fig. 3 shows the distribution of atmospheric stability with the mean wind speed at the four sites. There is a striking resemblance in the stability distributions of the two offshore sites, OWEZ (Fig. 3b) and Östergarnsholm (Fig. 3c), which are dominated by unstable conditions. At all sites there is an increase in neutral conditions with increasing wind speed, which indicates that mechanical production is dominant over buoyant production of turbulent kinetic energy. Hurghada is the most stable site due to cold temperatures prevailing during the long night hours. At both onshore sites the stable conditions dominate over the unstable conditions. In general this result is in agreement with the European Wind Atlas [36] where unstable conditions dominate at offshore sites and stable conditions at onshore. The stability distribution at OWEZ is slightly different from that obtained by [30] because a different data filtering criteria is used in this study.

4. WIND PROFILE AND TURBULENCE

According to similarity theory if we have similar sites, i.e. the friction velocity, surface roughness and buoynacy fluxes are approximately the same, then the mean wind profile and turbulence should be similar. Thus if we have homogeneous

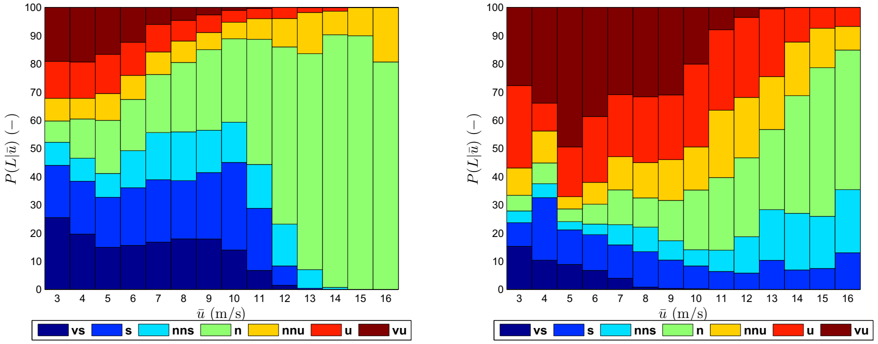

(a) Høvsøre

(b) OWEZ

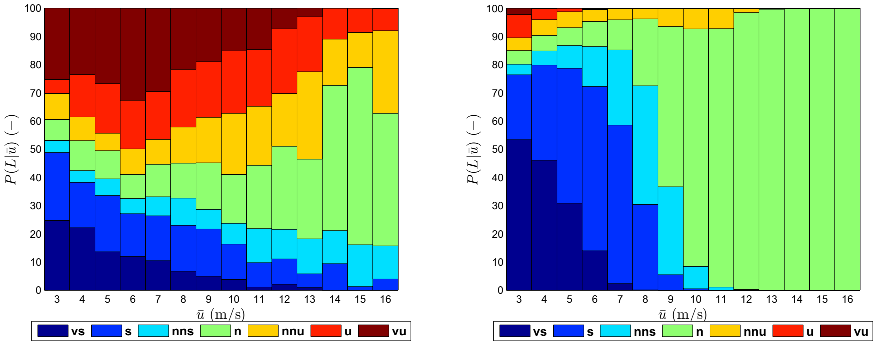

(c) Östergarnsholm

(d) Hurghada

Figure 3. Distribution of atmospheric stability for each mean wind speed at different sites.

conditions at different sites then we can obtain the wind profile and turbulent structure at only one site and apply those at other sites. In this study we make use of this assumption by performing a detailed wind profile and turbulence spectra analysis at Høvsøre only, and applying those at the other three sites. One of the major differences between the offshore and onshore sites is that the sea-surface roughness varies continuously over the water, whereas it is constant over the land (unless there has been any changes to the landscape during the period of data analysis). This will obviously have an influence on the wind profile and turbulence structure. Nevertheless we limit our study to using site specific wind speed and stability distributions only and use the same wind profile and turbulence at all sites.

4.1. Wind profile

Two wind profile models are studied. The first is the diabatic wind profile in the surface layer given as,

$$\bar{u} = \frac{u_*}{\kappa}\left[\ln\left(\frac{z}{z_0}\right) - \psi_m(z/L)\right], \tag{1}$$

where $\bar{u}$ is the mean wind speed, u_* is the friction velocity near the ground, $\kappa = 0.4$ is the von Kármán constant, z is the height, and $\psi_m(z/L)$ is the empirical stability function. We use the ψ_m relation from [6] for stable, and that from [7] for unstable conditions, where L is given as,

$$L = -\frac{{u_*}^3 T}{\kappa g \overline{w'\theta_v'}}. \tag{2}$$

Here T is the absolute temperature, θ_v is the virtual potential temperature and $\overline{w'\theta_v'}$ is the virtual kinematic heat flux. The second is the model by [5] that is valid for the entire boundary layer. It is given as follows: for neutral conditions,

$$\bar{u} = \frac{u_*}{\kappa}\left[\ln\left(\frac{z}{z_0}\right) + \frac{z}{L_{MBL}} - \frac{z}{z_i}\left(\frac{z}{2L_{MBL}}\right)\right] \tag{3}$$

for unstable conditions and

$$\bar{u} = \frac{u_*}{\kappa}\left[\ln\left(\frac{z}{z_0}\right) - \psi_m(z/L) + \frac{z}{L_{MBL}} - \frac{z}{z_i}\left(\frac{z}{2L_{MBL}}\right)\right] \tag{4}$$

for stable conditions,

$$\bar{u} = \frac{u_*}{\kappa}\left[\ln\left(\frac{z}{z_0}\right) - \psi_m(z/L)\left(1 - \frac{z}{2z_i}\right) + \frac{z}{L_{MBL}} - \frac{z}{z_i}\left(\frac{z}{2L_{MBL}}\right)\right] \tag{5}$$

where L_{MBL} is the length scale of the middle boundary layer, and z_i is the height of the planetary boundary layer. z_i is assumed to be proportional to u_* under neutral conditions as,

$$z_i = c\frac{u_*}{|f_c|}, \tag{6}$$

where f_c is the Coriolis parameter and c is a proportionality constant. For a neutral homogeneous terrain, [37] estimated $c = 0.15$ from the reanalysis of the Leipzig wind profile. Under diabatic conditions, there is no agreement on diagnostic expressions for z_i [8]. In the absence of measurements, it is expected that the climatological z_i decreases as the conditions become more stable. Hence, $c = 0.14$ is used for stable and $c = 0.13$ for very stable conditions as in [38]. The mean value of z_i obtained during neutral conditions is also applied for unstable conditions in accordance with [11]. L_{MBL}, which is a function of z_i, is estimated following [30].

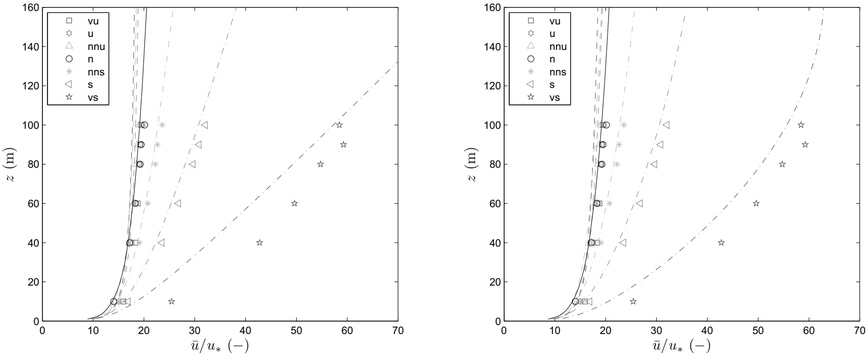

(a) surface-layer theory

(b) Boundar-Layer model by [5]

Figure 4. Measured and modelled surface-layer and boundary-layer wind profiles for different stability classes. The markers indicate measurements and the lines indicate the models. The unstable, neutral and stable wind profiles from the models are represented by dashed, solid and dash-dot lines respectively.

The comparison between the measured and modelled wind profile is shown in Fig. 4. The x-axis is normalized by the friction velocity in order to include the comparison for all mean wind speeds. We observe that there is considerable wind shear under stable conditions as compared to the unstable and neutral conditions, which is captured in the model by [5] reasonably well. In surface-layer theory the length scale increases with height without bounds, but in [5] it is limited by the boundary layer height. The differences between the two models are most pronounced under very stable conditions, where [5] fits the measurements slightly better (Fig. 4b). For unstable conditions both models agree well with the measurements, which indicates that limiting the length scale with boundary layer height may not be necessary. [30] gives a more detailed comparison between the two models.

4.2. Atmospheric turbulence

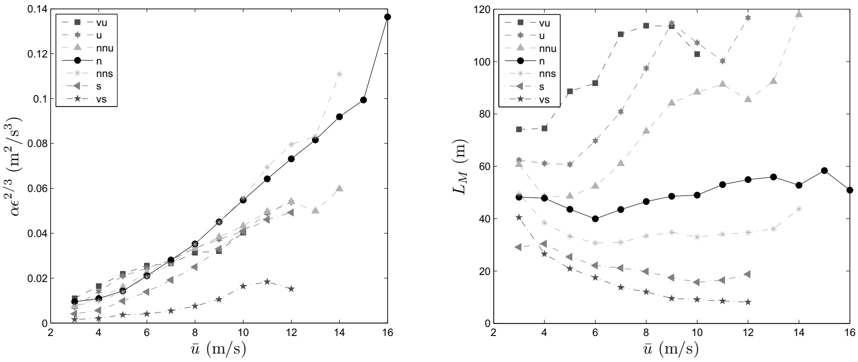

(a) $\alpha\epsilon^{2/3}$ **(b)** L_M

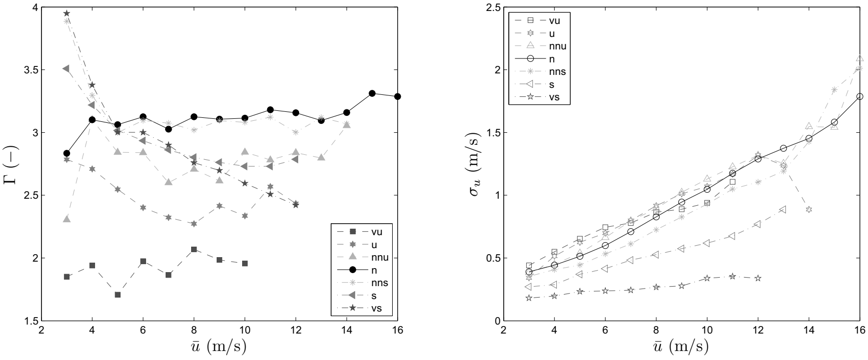

(c) Γ **(d)** σ_u

Figure 5. [3] model parameter fits at different mean wind speeds and atmospheric stabilities. The variation of the standard deviation of the u component is also given.

We quantify atmospheric turbulence using the Mann model [3]. This model is described by the three model parameters, $\alpha\epsilon^{2/3}$, which is a product of the spectral Kolmogorov constant α and the rate of viscous dissipation of specific turbulent kinetic energy to the two-thirds power $\epsilon^{2/3}$, a length scale (wavelength of the eddy corresponding roughly to the maximum spectral energy) L_M and an anisotropy parameter Γ. Thus any variation of turbulence with respect to specific site conditions means variation of $\alpha\epsilon^{2/3}$, L_M and Γ. The quite complicated equations of the spectral tensor model may be found in [3]. The $\alpha\epsilon^{2/3}$ parameter results in shifting the spectra in the vertical direction, i.e. increase in the value of $\alpha\epsilon^{2/3}$ results

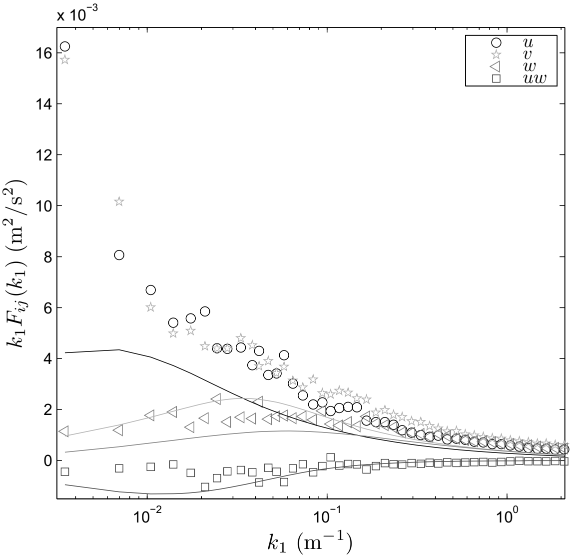

Figure 6. Turbulence spectra under very stable conditions for a mean wind speed of 3 m/s

in shifting the spectra up and vice-versa. The L_M parameter results in shifting the spectra in the horizontal direction, i.e. increase in the value of L_M results in shifting the spectra to the left and vice-versa. $\Gamma = 0$ corresponds to isotropic turbulence, i.e. $\sigma_u^2 = \sigma_v^2 = \sigma_w^2$, which are the variances for the u, v and w components of the wind field respectively. Increasing the Γ parameter beyond zero implies that $\sigma_u^2/\sigma_w^2 > 1$, $\sigma_v^2/\sigma_w^2 > 1$ and $\sigma_u^2/\sigma_v^2 > 1$.

The Mann model [3] is a semi empirical model that is strictly valid only for neutral conditions in the surface layer. Nevertheless, in this study we perform a χ^2-fit of the [3] model with the measurements to obtain $\alpha\epsilon^{2/3}$, L_M and Γ (using Eq. 4.1 from [3]) under different atmospheric stabilities at 80 and 100 m for mean wind speeds between 3 – 16 m/s. Ideally, we would like to fit the model with the measurements at 90 m, which is the hub height of the turbine (refer table III). Unfortunately, at Høvsøre we do not have sonic measurements at 90 m, and hence, $\alpha\epsilon^{2/3}$, L_M and Γ are linearly interpolated between 80 and 100 m to obtain the same at 90 m. We assume that since the difference between the measurement heights is only 20 m, the model parameters are locally linear (refer Fig. 4 in [39]) and the errors introduced in the two-point turbulence statistics by linear interpolation of the parameters would be negligible. It should also be noted that the performance of the Mann model [3] has not been tested in predicting coherences, i.e. two-point statistics under diabatic conditions, but in this study we assume that the coherences can be predicted under all conditions using this model.

Fig. 5 shows variation of $\alpha\epsilon^{2/3}$, L and Γ with the mean wind speed under diabatic conditions. In Fig. 5a it is observed that under all stabilities the energy dissipation rate increases with the increase in the mean wind speed. This is mainly because the turbulent energy production increases with increasing mean wind speeds. For a fixed z, neutral surface-layer scaling dictates that $\epsilon^{2/3} \propto \bar{u}^2$, which is reflected in Fig. 5a. The neutral conditions have the largest dissipation rates followed by the unstable conditions. The stable conditions have the smallest rate of dissipation because there is hardly any turbulent energy production. In Fig. 5b a systematic trend is observed with increasing mean wind speeds such that under unstable and neutral conditions the length scales increase, whereas under stable conditions they decrease. The increase in length scales under neutral conditions is in agreement with [39], however the magnitude of increase is much lower than that observed by [39].

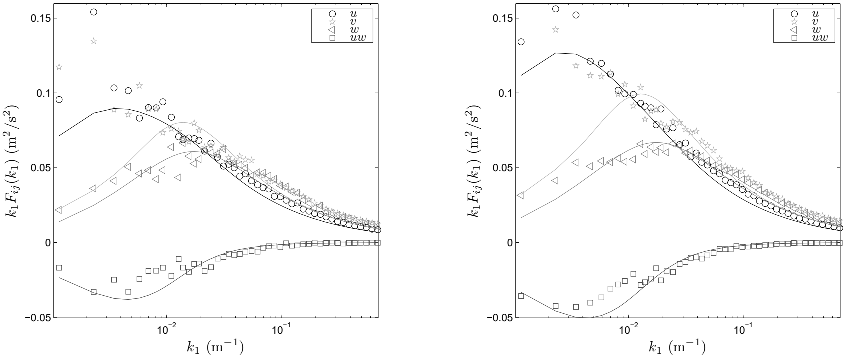

(a) very unstable

(b) unstable

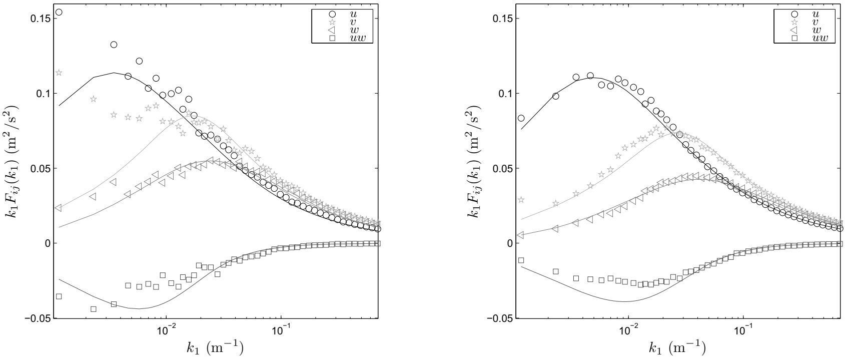

(c) near neutral unstable

(d) neutral

Figure 7. a–d: Turbulence auto-spectra of u, v, w components, and the uw co-spectrum at 80m for the mean wind speed of 9 m/s under different stabilities. The markers are the measurements and the smooth lines are Mann model [3] fits.

We speculate the decrease in the length scales under stable conditions as follows. From Fig. 6, we observe that there is a sharp increase in the energy content at low frequencies relative to that observed at high frequencies for low wind speeds. Under stable conditions there is hardly any turbulent energy as compared to unstable and neutral conditions. This causes the turbulent energy in the mesoscale range, which is known to be proportional to $f^{-5/3}$ for $f \gtrsim 2$ days^{-1} [40], to contribute to the increase in energy at low wavenumbers in the microscale range. This results in increasing the turbulent length scales at low wind speeds and stable conditions. At high wind speeds the microscale fluctuations becomes more powerful and the mesoscale contribution at low frequencies cannot be seen. Hence, under stable conditions at low wind speeds we observe larger length scales as compared to high wind speeds. In general we observe that the length scales are much larger under unstable conditions than under stable conditions, which is well known [2]. In Fig. 5c we observe that under neutral conditions the degree of anisotropy is constant with increasing mean wind speeds, whereas except for very unstable conditions it decreases weakly with increasing mean wind speeds. In general except for very low wind speeds, anisotropy is largest under neutral conditions whereas it is lowest for unstable conditions. Since the focus of this study is fatigue loads it is also interesting to observe variation in the degree of turbulence as standard deviation of the u component of the wind field σ_u with respect to atmospheric stability and mean wind speed (refer Fig. 5d). It is observed that σ_u is

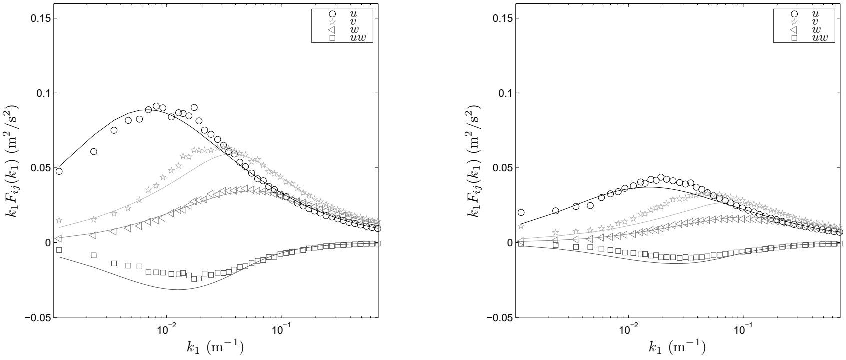

(e) near neutral stable

(f) stable

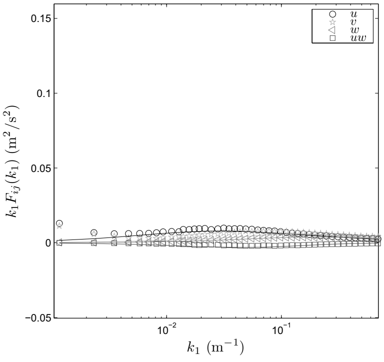

(g) very stable

Figure 7. e–g: Turbulence auto-spectra of u, v, w components, and the uw co-spectrum at 80m for the mean wind speed of 9 m/s under different stabilities. The markers are the measurements and the smooth lines are Mann model [3] fits.

greater for unstable conditions than stable conditions, but increases roughly linearly with the mean wind speed under all stability conditions.

Fig. 7 shows the fitted spectra of the u, v, w and uw components with the measurements for an example mean wind speed of 9 m/s under different atmospheric stabilities at 80 m. The variation in the spectral energy for different components is clearly evident, particularly for stable conditions, where there is very little turbulent energy. It is also evident that the Mann model [3] fits to the measurements is better under neutral conditions than under diabatic conditions. Nevertheless we can say that the model fits the measurements well under all stabilities (for $k_1 \gtrsim 0.01$ m^{-1}).

5. DESCRIPTION OF THE SIMULATION ENVIRONMENT

The simulations are carried out for mean wind speeds between 3 – 16 m/s with a bin size of 1 m/s. In this way, we can compare the cumulative fatigue loads, and also those varying with the mean wind speed. At Høvsøre, for the chosen eastern sector we do not have any wind observations above 16 m/s. For each wind speed bin we fit the Mann model [3] with the turbulence measurements from the sonics and obtain the three model parameters $\alpha\epsilon^{2/3}$, L_M and Γ. We obtain the wind profile over the entire turbine using the wind profile models described in section 4.1. The three-dimensional wind is then simulated over the entire rotor following [41]. The simulated loads are the blade root flap-wise and edge-wise bending moments, tower base fore-aft bending moments, and the rotor bending moments at the hub. The blade and rotor loads are obtained in the rotating coordinate system, whereas the tower loads are obtained in a fixed coordinate system.

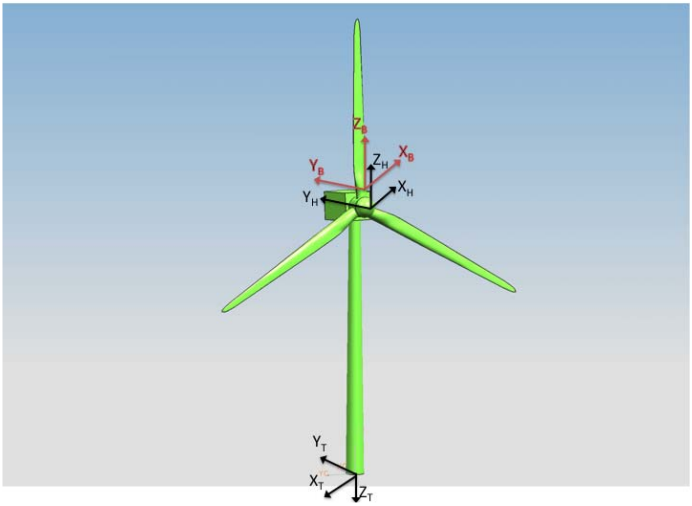

Figure 8. Coordinate systems for the blades (subscript B), hub (subscript H) and tower (subscript T)

Fig. 8 shows the coordinate system for the blades, hub, and the tower used in the load calculations. For each blade, the z-axis is along the blade, y-axis is in the mean wind direction and x-axis is in the lateral direction to the blade tip. The blade loads are obtained in the rotating blade coordinate system (subscript B) attached to the blade root. The rotor loads at the hub are obtained in the rotating coordinate system attached to the hub (subscript H). If we consider the initial position of the rotor such that the blade points upwards then the orientation of the axes are the same as that for the blade coordinate system, and rotates with this particular blade. The tower loads are obtained in a fixed coordinate system attached to tower base (subscript T), where the y-axis is along the mean wind direction, x-axis is in the lateral direction and the z-axis is in the vertical direction.

5.1. Wind turbine

We use the NREL 5 MW reference wind turbine for simulating the turbine loads, which is a fictional representative utility-scale multi-MW wind turbine, used by research teams throughout the world to standardize baseline offshore wind turbine specifications, and to quantify the benefits of advanced land- and sea-based wind energy technologies. The details of the turbine are given by [42]. The main characteristics of the turbine are given in table III.

5.2. Aero-elastic simulation tool – HAWC2

For simulating the aeroelastic response of the wind turbine, and calculating various loads on its components, the aeroelastic time-domain code HAWC2 is used, developed at Risø-DTU [43, 44]. The structural part of HAWC2 is based on a multi-body formulation using the floating frame of reference approach, where wind turbine main structures are subdivided into a number of bodies where each body consists of an assembly of Timoshenko beam elements. Each body has its own

Table III. Main properties of the wind turbine

Maximum Power	5 MW
Number of blades	3
Rotor diameter	126 m
Hub height	90 m
Cut-in wind speed	3 m/s
Rated wind speed	11.4 m/s
Cut-out wind speed	25 m/s
Control	Variable speed, collective pitch

coordinate system, with calculation of internal inertia loads when this coordinate system is moved in space, so that large rotation and translation of the body motion is accounted for. The aerodynamic forces are calculated using an unsteady Blade Element Momentum approach, including additional models for azimuthally dependent induction [*], dynamic inflow and tip losses. Static aerodynamic data for all airfoils is provided, which are corrected for rotational effects. The unsteady aerodynamics of the airfoil sections is taken into account by the Beddoes-Leishman type dynamic stall model of [45]. The influence of the tower on the inflow is accounted for with a potential flow 'tower shadow' model. The aerodynamic drag of the tower and nacelle is also modelled.

6. LOAD CALCULATIONS

In order to quantify the fatigue damage a widely used approach is to divide the random loads experienced by a component into single amplitude load ranges that are associated with the corresponding number of cycles to failure based on the experimentally obtained Wöhler curve (or the Stress-number of cycles, S-N curve). Following Palmgren-Miner linear damage rule we then assume that the damage from different load ranges can be linearly added to obtain the total fatigue damage of a component. Usually it is difficult to obtain the S-N curve of a component material (there is no data for the S-N curve because the NREL turbine used in this study is a fictitious turbine), and hence, we have to resort to other ways of quantifying the fatigue damage. Fortunately, we can do that using the concept of Damage Equivalent Load (D_{EQ}). It is defined as the fatigue load range corresponding to a number of equivalent load cycles N_{EQ}, that produces the same damage as the real load ranges D_i corresponding to the respective load cycles N_i. If we let D denote the total fatigue damage, D_{EQ} can implicitly be written as,

$$D = \sum D_i^m N_i = D_{EQ}^m N_{EQ}, \tag{7}$$

where m is the Wöhler exponent. In this study $m = 12$ is used for blades, i.e. corresponding to the glass fiber material, and $m = 3$ is used for estimating the hub and tower loads, since they are made up of steel. Rearranging the terms we get,

$$D_{EQ} = \Big(\frac{\sum D_i^m N_i}{N_{EQ}}\Big)^{1/m}. \tag{8}$$

In order to estimate D_{EQ} we thus need some algorithm that separates the random loads into individual load ranges and the corresponding number of cycles, and assume some value of N_{EQ}. In this study we use the Rainflow counting algorithm to estimate D_i and N_i and assume $N_{EQ} = 10^7$ cycles. The cumulative Damage Equivalent Load D_{EQ_C} including all mean wind speeds and atmospheric stabilities can be estimated using the wind speed and stability distributions given in section 3. Thus, if we denote $P(L|\bar{u})$ as the distribution of atmospheric stability at given mean wind speed and $P(\bar{u})$ as

---

[*] The calculation of thrust and induction is performed in a polar grid using the local wind speed vectors. This improves predictions in case of large wind shear and skew inflow.

the distribution of the mean wind speeds, then D_{EQ_C} is estimated as,

$$D_{EQ_C} = \sum_{\bar{u}=3}^{16}\Big(\sum_{L=\text{vu}}^{\text{vs}} D_{EQ} \times P(L|\bar{u})\Big) \times P(\bar{u}). \tag{9}$$

The limits of L indicate the corresponding probability of atmospheric stability at a given mean wind speed, where vu denotes very unstable conditions, and vs denotes very stable condition. The operating conditions considered are normal power production for the chosen wind speed range. Variations in the load cases are given in table IV. For each mean wind speed and atmospheric stability the turbulent field is generated for 10 random seeds to reduce the statistical uncertainty [†], and the simulation time is 600 s. Table V gives the normalized D_{EQ_C} for different cases at different sites. At each site the loads are normalized with those from the reference case I. The blade flap-wise and edge-wise loads are defined as the bending moments at the root of the blade along the x and y axis respectively, in the blade coordinate system (Fig. 8). The fore-aft loading of the tower is defined as the bending moment at the base of the tower along the x-axis in the tower coordinate system (Fig. 8). M_x, M_y and M_z denote the rotor loads at the hub defined along the x, y and z axis respectively, in the rotating hub coordinate system (Fig. 8). Cases I and II compare the influence of the diabatic boundary-layer wind profile and turbulence on the loads with those obtained by assuming neutral conditions only. Cases I and III

Table IV. Load cases

Cases	
I	Diabatic boundary-layer wind profile and turbulence
II	Neutral boundary-layer wind profile and turbulence
III	Diabatic surface-layer wind profile and turbulence
IV	IEC load case, power law exponent = 0.2

Table V. Normalized D_{EQ_C} of bending moments at different sites

	Blade root		Tower base	Rotor loads		
Cases	flap	edge	fore-aft	M_x	M_y	M_z
			Høvsøre			
I	1.000	1.000	1.000	1.000	1.000	1.000
II	0.994	0.996	1.160	0.885	0.996	0.996
III	1.060	1.004	0.987	1.079	1.005	1.016
IV	1.378	1.018	1.749	1.277	1.013	1.089
			OWEZ			
I	1.000	1.000	1.000	1.000	1.000	1.000
II	1.029	1.003	1.028	1.032	1.002	0.995
III	0.989	0.998	0.997	0.981	0.998	1.004
IV	1.356	1.029	1.397	1.421	1.024	1.092
			Östergarnsholm			
I	1.000	1.000	1.000	1.000	1.000	1.000
II	1.020	1.001	1.084	0.999	1.001	1.001
III	1.027	1.001	0.990	1.034	1.002	1.011
IV	1.458	1.022	1.776	1.482	1.019	1.110
			Hurghada			
I	1.000	1.000	1.000	1.000	1.000	1.000
II	1.030	0.999	1.170	0.946	0.999	1.009
III	1.040	1.002	0.978	1.053	1.004	1.014
IV	1.491	1.019	1.956	1.420	1.016	1.120

[†] IEC standard [1] recommends simulation for at least 6 random seeds

compare the differences in the loads obtained by using boundary-layer and surface-layer wind profile models (section 4.1). The turbulence used is the same for both cases. Cases I and IV shows the corresponding comparison with the IEC load case.

6.1. Tower base fore-aft loads

The tower loads will be mainly caused due to the variation in the thrust exerted by the wind field on the rotor. In this study, the variation in the input wind field is due to the wind profile and turbulence that varies with atmospheric stability. Thus it is important to understand the variation of the thrust force due to variation in atmospheric stability. We hypothesize that the force exerted by the wind profile will mainly cause a dynamic moment at the blade root or at the hub, whereas that exerted by turbulence will cause a dynamic moment at the tower base. If we conceptualize turbulence in the form of eddies then intuitively it can be said that the larger the size of the eddy, the larger will be the dynamic force, and vice versa. From Fig. 5b we observe that the turbulence length scales (or characteristic eddy sizes) decrease as the conditions change from unstable to stable. We then expect that the large eddies under unstable conditions will exert a large dynamic force on the entire rotor that will cause large dynamic moments in the fore-aft direction. Under stable conditions the rotor will act as a low-pass filter that causes some averaging of the turbulence. For a three-bladed rotor with blades at 120° with respect to each other, the variation of the force exerted by the wind profile on tower base will average out. We think that this is because the asymmetry in the loads due to the wind profile will be experienced by all three blades equally, that averages out as the blades sweep the rotor area.

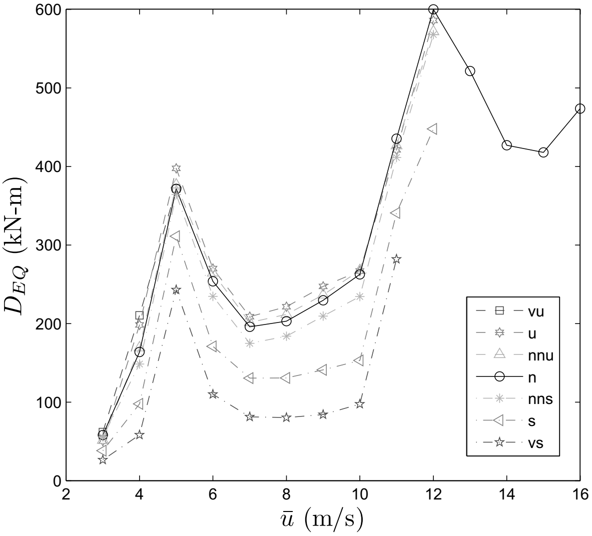

Figure 9. Variation of tower base fore-aft loads with respect to mean wind speeds and atmospheric stability.

In order to verify the above reasoning, we plot the variation of tower loads with respect to mean wind speeds and atmospheric stability in Fig. 9. The loads are largest for unstable and neutral conditions, whereas they are significantly smaller under stable conditions (of the order of 2). If we compare the turbulent energy in the low wavenumber range (or large length scales), i.e. between $10^{-3} < k_1 < 10^{-1}$ m^{-1} in Fig. 7, then we observe a relatively small difference between the unstable and neutral conditions (roughly by a factor of 1.2), but a large difference under stable conditions (roughly by a factor of 10). At smaller length scales, corresponding roughly to $k_1 > 10^{-1}$ m^{-1}, except for very stable conditions, the difference in the turbulent energy is relatively small (of the order of 2). Hence, the length scales under unstable and neutral conditions that contain larger turbulent energy at low wavenumbers cause more fatigue damage than under stable conditions. Variation of the loads with respect to wind speed is highly non-linear. At about 5 m/s we observe a peak in the loads because at that wind speed the natural frequency of the tower (≈ 0.33 Hz) correspond to three times the rotational frequency. At 11 m/s the rated power is produced, and above that wind speed the pitching of the rotor blades causes a decrease of the loads.

At Høvsøre and Hurghada, we observe a reduction in calculated tower loads of approximately 16% and 17% respectively under diabatic conditions in comparison to those assuming only neutral conditions, whereas at OWEZ and Östergarnsholm the corresponding reduction of approximately 3% and 8% respectively. Høvsøre and Hurghada are dominated by stable conditions, whereas OWEZ and Östergarnsholm are dominated by unstable and near-neutral conditions. From Fig. 9, we observe that under stable conditions the tower loads are much smaller than those under unstable and neutral conditions. Hence, there is larger reduction in the calculated tower loads using diabatic wind conditions at Høvsøre and Hurghada than at OWEZ and Östergarnsholm.

Our intuitive understanding that wind profiles will not influence tower loads is verified by comparing cases I and III, where under diabatic conditions two different wind profile models are used but with the same turbulence. Even at Høvsøre and Hurghada, which are stable sites, and where the surface-layer wind profile model predicts a large wind shear (see Fig. 4), there is hardly any difference between the tower loads (up to 2% only). There is a negligible difference ($< 1\%$) in the calculated tower loads at OWEZ and Östergarnsholm.

At all sites the calculated IEC tower loads are significantly larger (up to 96%) than those obtained by using diabatic turbulence and wind shear, which means that the IEC standard [1] is very conservative in the definition of wind shear and turbulence. The $\alpha\epsilon^{2/3}$ parameter defined according to the IEC standard is about 4.5 to 1.5 times larger for mean wind speeds from 3 to 16 m/s than that observed at Høvsøre. The L_M and Γ parameters are constant according to the IEC definition and have values of 42 m and 3.9 respectively, whereas from Figs. 5b and 5c we observe that L_M and Γ vary significantly with atmospheric stability and mean wind speed. Wind profile is defined by the power law with an exponent of 0.2 in the IEC standard for all mean wind speeds, which is also a conservative estimate. The overall result is that we get a conservative estimate of the tower loads.

6.2. Blade loads

It is interesting to note in Table V that the blade root flap-wise loads are not notably influenced by atmospheric stability, since the difference in the dynamic loads obtained using diabatic wind conditions and those obtained assuming neutral conditions is only up to 3%. We hypothesize that the blade flap-wise loads as defined in section 6 will be influenced by both, the wind profile and turbulence, which will be seen as dynamic moments at the root section. This is in contrast to the loads observed at the tower base, where only turbulence seems to be influential. The dynamic force exerted by the wind on the blade due to wind profile under diabatic conditions is in direct contrast with that exerted by turbulence. Under stable conditions there is a large wind gradient as compared to unstable conditions. Thus wind profile under stable conditions will exert a larger dynamic force on the blades than under unstable conditions. This has been verified from a previous study [24], where only steady winds are considered. On the contrary, turbulence is lower under stable conditions as compared to that under unstable conditions (see Fig. 5d). This means that under stable conditions there will be smaller amplitude load ranges as compared to unstable conditions. The combined influence on the blades is that the flap-wise loads are averaged out under diabatic conditions (see cases I and II in table V).

In order to verify the above reasoning, the variation of blade root flap-wise loads with respect to mean wind speeds and atmospheric stability is plotted in Fig. 10 . We observe that the flap-wise loads are increased only slightly (of the order of 1.2) from unstable to stable conditions. It shows that contrasting influence of wind profiles and turbulence under diabatic conditions tend to average out the loads. The loads increase with the mean wind speed (Fig. 10) even after the rated wind speed has reached. This is because wind speed standard deviation increases with the mean wind speed causing greater

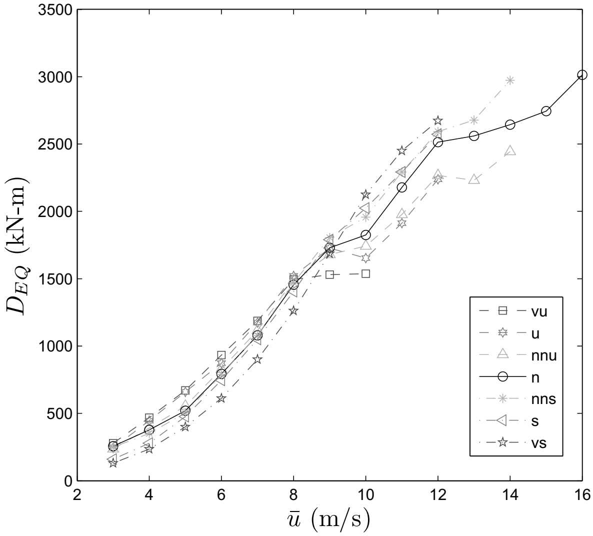

Figure 10. Variation of blade root flap-wise loads with respect to mean wind speeds and atmospheric stability.

number of large load range cycles to occur at high wind speeds (refer Fig. 5d). At Høvsøre, we observe that the flap-wise loads are completely averaged out. At Hurghada we observe about 3% difference between cases I and II likely because of the low Weibull λ and k parameters. At other sites we do not observe much difference in the blade root flap-wise loads under diabatic and neutral conditions.

We observe a slightly larger influence of using a different wind shear model, where the loads vary by up to 6% (cases I and III). Using the surface-layer wind profile (case III) we get a large wind gradient under stable conditions thus resulting in large asymmetrical loading as compared to the model by [5] (case I). At Høvsøre and Hurghada where stable conditions dominate over unstable conditions this effect is more pronounced. At OWEZ and Östergarnsholm the conditions are mostly unstable, and hence, we do not observe much influence of changing the wind shear model. As observed for the tower base fore-aft loads, the blade root flap-wise loads are significantly larger for the IEC load case (up to 50%) in comparison with those obtained under diabatic conditions (cases I and IV).

At all sites the blade root edge-wise loads are the least influenced by atmospheric stability, where the difference with neutral conditions is less than 1%. This is mainly because the gravity forces resulting from the mass of the blades are more dominant in producing edge-wise loads as compared to the wind loads. For the same reason we also do not see any influence of using a different wind profile model (cases I and III). Even with the very conservative IEC standard we observe that the variation in the loads is up to 3% only.

6.3. Rotor loads

The difference between the rotor and blade loads is that the rotor loads are experienced at the hub due to the combined loading by all three blades, whereas the blade loads are experienced at the respective blade root for each blade. The rotor yaw and tilt loads can be calculated if the azimuth angle is fixed, but in this study the rotor loads are obtained in a rotating coordinate system. Thus, the rotor M_x and M_z loads along x and z axis respectively experience alternating yaw and tilting loads depending on the azimuth position. From table V we see that the rotor loads along the x axis (M_x) obtained under diabatic conditions are up to 12% larger than those obtained assuming neutral conditions. It is interesting to note that this result is in contrast to that observed for tower loads, where the loads under neutral conditions were larger than those obtained under diabatic conditions. From Fig. 8 we see that M_x is calculated by combining the moment of the vertical blade in one direction with those induced by the other two blades in the opposite direction. As the blades sweep the rotor area the flapping moments induced by two blades will counteract that induced by the third blade. The larger wind gradient under stable conditions will induce larger moments at the hub than those under unstable conditions. Hence, at Høvsøre and Hurghada, which are predominantly stable sites, large M_x loads are experienced at the hub due to large wind shear. OWEZ and Östergarnsholm are predominantly unstable sites, and hence we do not observe much difference in the M_x loads between diabatic and neutral conditions (cases I and II). From the results it seems that the rotor loads are mainly experienced due to variation in the wind profile, and turbulence has only a minor influence.

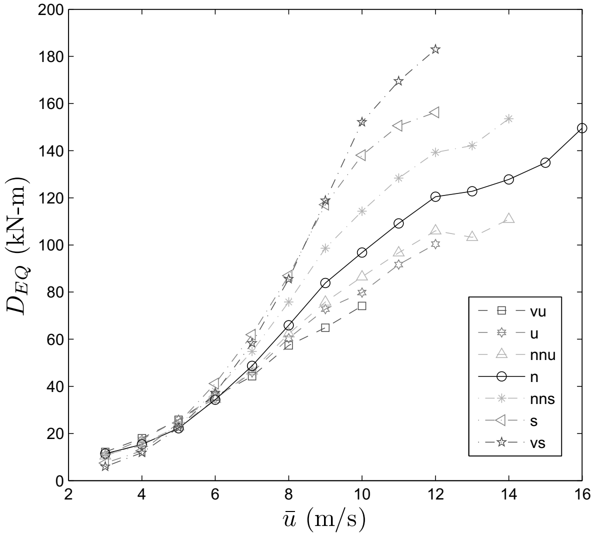

Figure 11. Variation of rotor M_x loads with respect to mean wind speeds and atmospheric stability.

The variation of the rotor M_x loads with respect to atmospheric stability and mean wind speeds is plotted in Fig. 11. We observe that the loads increase significantly with increasing wind speeds when the conditions change from unstable to stable (by a factor of 2). This provides some basis for the hypothesis that only the wind profile influences rotor M_x loads. It is interesting to note that the variation of M_x with atmospheric stability is in contrast with that observed for tower loads (see Figs. 9 and 11). As with the blade loads the rotor M_x loads increase with the mean wind speeds. The hypothesis that only wind profiles influence rotor M_x loads is further strengthened when we compare cases I and III in table V. The surface-layer wind profile model with a much larger wind gradient in comparison to the wind profile model by [5] induces larger rotor M_x loads. At stable sites (Høvsøre and Hurghada) we observe that using the surface layer wind profile model the rotor M_x loads are up to 8% larger than those obtained using the wind profile model by [5]. At OWEZ, which is predominantly unstable site, we observe a reduction in the rotor M_x loads. The conservative IEC standards calculate much larger M_x loads (up to 48%) in comparison to the measured wind conditions.

The rotor loads along the z axis (M_z) are not influenced by atmospheric stability. Taking a closer look at the coordinate system defined for rotor loads (refer Fig. 8) we observe that the moment along the z-axis will be induced only due to those blades through which the hub coordinate system does not pass. In Fig. 8 it is then due to the two blades at angle of 120° and pointing downwards. The resulting moment M_z will then be a summation of a positive moment due to one blade and a negative moment due to the other blade. If say we had no turbulence and the wind was completely uniform, then M_z would be zero and in principle we would have no rotor loads along the z-axis. However, in reality wind profile and turbulence exist, and M_z varies non-linearly with respect to the wind speed. Hence, it will create a differential loading of the two blades as they sweep the rotor area. The magnitude of this differential loading seems to be small. Hence, we get same M_z under diabatic and neutral conditions (cases I and II).

The rotor loads along the y axis (M_y) are not influenced by atmospheric stability. This is because gravity will have a more dominating influence instead of the wind loads, in a similar manner as compared to the blade root edge-wise loads. The difference in the loads in comparison with the IEC standard is up to 2% only (cases I and IV).

7. DISCUSSION AND CONCLUSIONS

The main goal of this study is to understand if the wind turbine loads are influenced by atmospheric stability. Load calculations are performed on the NREL 5 MW reference wind turbine. Atmospheric stability is introduced in the form of Monin-Obukhov length L in the wind profile models and turbulence. Two wind profile models are used, one that is the standard surface-layer model and the other that is valid for the entire boundary layer by [5]. Atmospheric turbulence is modelled using the Mann model [3]. The model is fitted to the turbulence measurements at Høvsøre under diabatic conditions and the three model parameters $\alpha\epsilon^{2/3}$, L_M and Γ are obtained. The loads are simulated using the aero-elastic simulation tool HAWC2 developed at Risø DTU [44]. Four sites (two offshore and two onshore) with a different wind speed and stability distribution are chosen. The loads are quantified as the cumulative Damage Equivalent Load (D_{EQ_C}) for the blade root flap-wise and edge-wise moments, tower base fore-aft moment and rotor M_x, M_y and M_z moments at the hub.

The influence of wind profiles and turbulence have contrasting effect on wind turbine loads under diabatic conditions, i.e. under stable conditions the wind gradient is large, which induces larger fatigue loads (as observed in [24]), whereas turbulence is small, which induces smaller fatigue loads. It was observed that under diabatic conditions the tower loads are influenced mainly by turbulence (Fig. 9), blade loads by a combination of wind profile and turbulence (Fig. 10), and rotor loads mainly by wind profile (Fig. 11). The calculate tower loads are up to 17% smaller using diabatic wind conditions in comparison to those obtained under neutral conditions. The corresponding blade loads are up to 3% smaller, whereas the rotor loads are up to 12% larger than those obtained assuming only neutral conditions. All loads are obviously dependent on the wind speed and stability distributions. Thus, a wind turbine at a site where stable conditions are dominant experiences smaller tower loads if diabatic wind conditions are used in load calculations, as compared to loads obtained assuming neutral conditions only. On the other hand larger rotor M_x loads are experienced using diabatic wind conditions, as compared to those obtained assuming neutral conditions only. It is to be noted that the rotor loads are specific to the coordinate system used in load calculations. The behaviour of the tower loads would be opposite for a predominantly unstable site. This cannot be said for the rotor M_x loads because the difference in the wind gradient between unstable and neutral conditions is much smaller than that between stable and neutral conditions (see Fig. 4). This means that approximately same rotor M_x loads are obtained using diabatic wind conditions, as compared to those obtained assuming only neutral conditions. This is verified for two predominantly unstable offshore sites, OWEZ and Östergarnsholm. The blade loads calculated under diabatic conditions average out, and are approximately the same as those obtained assuming neutral conditions only.

The importance of using a boundary-layer wind profile model is observed for blade and rotor M_x loads, particularly for stable sites. Thus, if these loads are calculated assuming only the surface-layer wind profile model at stable sites then the calculated blade and rotor M_x loads will be much larger in comparison to those obtained using a boundar-layer wind profile model. The main cause of this increase in loading is because in the surface-layer wind profile model under stable conditions the wind profile length scale increases infinitely, leading to large wind gradients. The boundary-layer wind profile model by [5] limits the growth of this length scale using the boundary layer height z_i, leading to smaller wind shear (also observed in the measurements in Fig. 4) in comparison to the surface-layer model.

The IEC standards are extremely conservative in its definition of wind shear and turbulence. The calculated loads using the IEC standard are much larger (up to 95%) in comparison to those obtained using the site specific wind conditions. This presents a case for performing detailed calculations of the loads for all IEC load cases defined in [1]. The goal is to eventually reduce wind turbine costs, and such a study can provide valuable comparisons with the current design standard. As to whether to include atmospheric stability in load calculations depends on the influence of overestimating the loads on wind turbine costs. A detailed cost analysis is required to make any conclusions about how important atmospheric stability is for wind turbine loads. Also, a detailed investigation is necessary to verify whether the differences in the calculated loads under diabatic conditions are larger compared to the uncertainties in the load calculations.

ACKNOWLEDGEMENTS

The data from the Offshore Wind farm Egmond aan Zee (OWEZ) were kindly made available by NoordZeewind as part of the PhD project under the Research Program WE@Sea. The data at the Høvsøre Test Station was collected under the auspices of Anders Ramsing Vestergaard and Bjarne Sønderskov. For the data at Östergarnsholm the authors are grateful to Xiaoli Larsén from Risø DTU and Anna Rutgersson from Uppsala University for making it available. The authors are also thankful to Niels Moretensen from Risø DTU for providing the data at Hurghada. The resources provided by the Center for Computational Wind Turbine Aerodynamics and Atmospheric Turbulence funded by the Danish Council for Strategic Research grant no. 09-067216 are also acknowledged. The authors are thankful to the help provided by Torben Larsen from Risø DTU in the aero-elastic simulations. Finally, the authors are also thankful to Gunner Larsen from Risø DTU for interesting discussions and providing valuable feedback to the article.

REFERENCES

1. IEC. IEC 61400-1. Wind turbines – Part 1: Design Requirements 2005; .
2. Kaimal JC, Wyngaard JC, Izumi Y, Coté OR. Spectral characteristics of surface-layer turbulence. *Quarterly Journal of the Royal Meteorological Society* 1972; **98**(417):563–589, doi:10.1002/qj.49709841707.
3. Mann J. The spatial structure of neutral atmospheric surface-layer turbulence. *Journal of Fluid Mechanics* 1994; **273**:141–168, doi:10.1017/S0022112094001886.
4. Monin AS, Obukhov AM. Basic laws of turbulent mixing in the atmosphere near the ground. *Tr. Akad. Nauk. SSR, Geofiz. Inst.* 1954; **151**:163–187.
5. Gryning SE, Batchvarova E, Brümmer B, Jørgensen H, Larsen S. On the extension of the wind profile over homogeneous terrain beyond the surface layer. *Boundary-Layer Meteorology* 2007; **124**(2):251–268, doi: 10.1007/s10546-007-9166-9.
6. Businger JA, Wyngaard JC, Izumi Y, Bradley EF. Flux-profile relationships in the atmospheric surface layer. *Journal of the Atmospheric Sciences* 1971; **28**:181–189, doi:10.1175/1520-0469(1971)028<0181:FPRITA>2.0.CO;2.
7. Grachev AA, Fairall CW, Bradley EF. Convective profile constants revisited. *Boundary-Layer Meteorology* 2000; **94**(3):495–515.
8. Seibert P, Beyrich F, Gryning SE, Joffre S, Rasmussen A, Tercier P. Review and intercomparison of operational methods for the determination of the mixing height. *Atmospheric Environment* 2000; **34**(7):1001–1027.
9. Blackadar AK. The vertical distribution of wind and turbulent exchange in a neutral atmosphere. *Journal of Geophysical Research* 1962; **67**(8):3095–3102, doi:10.1029/JZ067i008p03095.

10. Lettau HH. Theoretical wind spirals in the boundary layer of a barotropic atmosphere. *Beitr. Phys. Atmos.* 1962; **35**:195–212.
11. Peña A, Gryning SE, Hasager CB. Comparing mixing-length models of the diabatic wind profile over homogeneous terrain. *Theoretical and Applied Climatology* 2010; **100**:325–335, doi:10.1007/s10546-008-9323-9.
12. Kristensen L, Lenschow DH, Kirkegaard P, Courtney M. The spectral velocity tensor for homogeneous boundary-layer turbulence. *Boundary-Layer Meteorology* 1989; **47**(1–4):149–193, doi:10.1007/BF00122327.
13. Maxey MR. Distortion of turbulence in flows with parallel streamlines. *Journal of Fluid Mechanics* 1982; **124**:261–282, doi:10.1017/S0022112082002493.
14. von Kármán T. Progress in the statistical theory of turbulence. *Proceedings of National Academy of Sciences, USA*, vol. 34, California Institute of Technology, Pasadena, 1948; 530–539.
15. Kristensen L, Jensen NO. Lateral coherence in isotropic turbulence and in the natural wind. *Boundary-Layer Meteorology* 1979; **17**(3):353–373, doi:10.1007/BF00117924.
16. Hanazaki H, Hunt JCR. Structure of unsteady stably stratified turbulence with mean shear. *Journal of Fluid Mechanics* 2004; **507**:1–42, doi:10.1017/S0022112004007888.
17. Fragoulis AN. The complex terrain wind environment and its effects on the power output and loading of wind turbines. *ASME Wind Energy Symposium*, American Institute of Aeronautics and Astronautics, Inc., 1997; 33–40. AIAA Paper 97-0934.
18. Sutherland HJ. Analysis of the structural and inflow data from the LIST turbine. *Journal of Solar Energy Engineering - Transactions of ASME* 2002; **124**(4):432–445, doi:10.1115/1.1507763.
19. Eggers AJ, Digumarthi R, Chaney K. Wind shear and turbulence effects on rotor fatigue and loads control. *Journal of Solar Energy Engineering - Transactions of ASME* 2003; **125**(4):402–409, doi:10.1115/1.1629752.
20. Nelson LD, Manuel L, Sutherland HJ, Veers PS. Statistical analysis of wind turbine inflow and structural response data from the LIST program. *Journal of Solar Energy Engineering - Transactions of ASME* 2003; **125**(4):541–550, doi:10.1115/1.1627831.
21. Kelley ND, Jonkman BJ, Scott GN, Bialasiewicz JT, Redmond LS. The impact of coherent turbulence on wind turbine aeroelastic response and its simulation. AWEA Windpower, 2005.
22. Downey RP. Uncertainty in wind turbine life equivalent loads due to variation of site conditions. M.sc thesis project, Technical University of Denmark, Fluid Mechanics Section April 2006.
23. Veldkamp D. Chances in wind energy: A probabilistic approach to wind turbine fatigue design. Phd thesis, Delft University of Technology 2006.
24. Sathe A, Bierbooms W. The influence of different wind profiles due to varying atmospheric stability on the fatigue life of wind turbines. *The Science of Making Torque from Wind*, *Journal of Physics: Conference Series*, vol. 75, Hansen MOL, Hansen KS (eds.), 2007; 12 056–12 062, doi:10.1088/1742-6596/75/1/012056.
25. Saranyasoontorn K, Manuel L. On the propogation of uncertainty in inflow turbulence to wind turbine loads. *Journal of Wind Engineering and Industrial Aerodynamics* 2008; **96**(5):503–523, doi:10.1016/j.jweia.2008.01.005.
26. Mücke T, Kleinhans D, Peinke J. Atmospheric turbulence and its influence on the alternating loads on wind turbines. *Wind Energy* 2011; **14**(2):301–316, doi:10.1002/we.422.
27. Kaimal JC, Finnigan JJ. *Atmospheric Boundary Layer Flows*, chap. Acquisition and processing of atmospheric boundary layer data. 7, Oxford University Press, New York, 1994; 255–257.
28. Sathe A, Mann J, Gottschall J, Courtney MS. Can wind lidars measure turbulence? *Journal of Atmospheric and Oceanic Technology* 2011; **28**(7):853–868, doi:10.1175/JTECH-D-10-05004.1.
29. Grachev AA, Fairall CW. Dependence of the Monin-Obukhov stability parameter on the bulk Richardson number over the ocean. *Journal of Applied Meteorology* 1996; **36**:406–414.
30. Sathe A, Gryning SE, Peña A. Comparison of the atmospheric stability and wind profiles at two wind farm sites over a long marine fetch in the North Sea. *Wind Energy* 2011; **14**(6):767–780, doi:10.1002/we.456.

31. Högström U, Sahlé E, Drennan WM, Kahma KK, Smedman AS, Johansson C, Pettersson H, Rutgersson A, Zhang LTF, Johansson M. Momentum fluxes and wind gradients in the marine boundary layer – a multi-platform study. *Boreal Environment Research* 2008; **13**:475–502.
32. Larsén X, Smedmann A, Högström U. Air-sea exchange of sensible heat over the Baltic Sea. *Quarterly Journal of the Royal Meteorological Society* 2004; **130**(597):519–539, doi:10.1256/qj.03.11.
33. Smedmann A, Högström U, Bergström H, Rutgersson A. A case study of air-sea interaction during swell conditions. *Journal of Geophysical Research* 1999; **104**:25 833–25 851, doi:10.1029/1999JC900213.
34. Motta M, Barthelmie RJ. The influence of non-logarithmic wind speed profiles on potential power output at Danish offshore sites. *Wind Energy* 2005; :219–236doi:10.1002/we.146.
35. Mortensen NG, Said US, Frank HP, Georgy L, Hasager CB, Akmal M, Hansen JC, Salam AB. *Wind atlas for the Gulf of Suez. Measurements and Modelling 1991 – 2001*. New and Renewable Energy Authority, Cairo, and Risø National Laboratory, Roskilde, 2003. 196 pp.
36. Troen IB, Petersen E. European wind atlas. *Technical Report*, Risø National Laboratory 1989.
37. Peña A, Gryning SE, Mann J, Hasager CB. Length scales of the neutral wind profile over homogeneous terrain. *Journal of Applied Meteorology and Climatology* 2010; **49**:792–806, doi:10.1175/2009JAMC2148.1.
38. Peña A, Gryning SE, Hasager CB. Measurement and modelling of the wind speed profile in the marine atmospheric boundary layer. *Boundary-Layer Meteorology* 2008; **129**(3):479–495, doi:10.1007/s10546-008-9323-9.
39. Peña A, Gryning SE, Mann J. On the length scale of the wind profile. *Quarterly Journal of the Royal Meteorological Society* 2010; **136**(653):2119–2131, doi:10.1002/qj.714.
40. Larsén XG, Ott S, Badger J, Hahmann AN, Mann J. Recipes for correcting the impact of effective mesoscale resolution on the estimation of extreme winds. *Journal of Applied Meteorology and Climatology* 2011; doi: 10.1175/JAMC-D-11-090.1.
41. Mann J. Wind field simulation. *Prob. Engng. Mech.* 1998; **13**(4):269–282.
42. Jonkman J, Butterfield S, Musial W, Scott G. Definition of a 5-MW reference wind turbine for offshore system development. *Technical report*, National Renewable Energy Laboratories, Colorado, USA 2008.
43. Larsen TJ, Hansen AM. Influence of Blade Pitch Loads by Large Blade Deflections and Pitch Actuator Dynamics Using the New Aeroelastic Code HAWC2. *Proceedings of the European Wind Energy Conference and Exhibition, Athens Greece*, 2006.
44. Larsen TJ, Hansen AM. How 2 HAWC2, the user's manual. *Risø R report Risø-R-1597(ver. 3-1)(EN)*, Risø 2007.
45. Hansen MH, Gaunaa M, Madsen HA. A Beddoes-Leishman type dynamic stall model in state-space and indicial formulations. *Risø R report Risø-R-1354(EN)*, Risø 2004.

Part II

Turbulence measurements by wind lidars

Chapter 5

Measurement of second-order turbulence statistics using wind lidars

The results obtained in chapters 3 and 4 indicate that there is significant difference in wind turbine loads when site-specific wind conditions are used in comparison to those obtained using the IEC [2005a] defined wind conditions. This provides a strong incentive for measuring wind profiles and turbulence at the site where wind turbines will operate. Cup or sonic anemometers are the state-of-the art in measuring wind speeds. Especially, for turbulence measurements sonic anemometers are widely used. Both these anemometers require a meteorological mast that adds to the complexity and cost of the measurement campaign. Recently wind lidars have provided a tremendous boost for wind energy purposes, since wind speeds can be measured remotely. Lidars measure the mean wind speeds with very good accuracy as compared to cup anemometers [Courtney et al., 2008]. Their ability to perform turbulence measurements is still a matter of research.

The wind lidars used for wind energy purposes derive wind speeds using the velocity azimuth display (VAD) technique. This results in large systematic errors in turbulence measurements. In this chapter we model these errors for a continuous-wave (ZephIR) and a pulsed (WindCube) lidar from the basic principles. We take into account the averaging effect of the turbulence measurements that arise due to the large sample volume in which lidars measure wind speeds. We also take into account the contamination of turbulence components that result from the contribution of all components of the Reynolds stress tensor. The model makes use of the Mann [1994] model to describe the three-dimensional turbulence structure. Comparisons with the measurements under diabatic conditions are carried out at different heights.

AMS's full Copyright Notice

VOLUME 28 JOURNAL OF ATMOSPHERIC AND OCEANIC TECHNOLOGY JULY 2011

Can Wind Lidars Measure Turbulence?

A. SATHE

Faculty of Aerospace Engineering, Section Wind Energy, Delft University of Technology, Delft, Netherlands

J. MANN, J. GOTTSCHALL, AND M. S. COURTNEY

Wind Energy Division, Risø DTU, Roskilde, Denmark

(Manuscript received 5 October 2010, in final form 10 January 2011)

ABSTRACT

Modeling of the systematic errors in the second-order moments of wind speeds measured by continuous-wave (ZephIR) and pulsed (WindCube) lidars is presented. These lidars use the conical scanning technique to measure the velocity field. The model captures the effect of volume illumination and conical scanning. The predictions are compared with the measurements from the ZephIR, WindCube, and sonic anemometers at a flat terrain test site under different atmospheric stability conditions. The sonic measurements are used at several heights on a meteorological mast in combination with lidars that are placed on the ground. Results show that the systematic errors are up to 90% for the vertical velocity variance, whereas they are up to 70% for the horizontal velocity variance. For the ZephIR, the systematic errors increase with height, whereas for the WindCube, they decrease with height. The systematic errors also vary with atmospheric stability and are low for unstable conditions. In general, for both lidars, the model agrees well with the measurements at all heights and under different atmospheric stability conditions. For the ZephIR, the model results are improved when an additional low-pass filter for the 3-s scan is also modeled. It is concluded that with the current measurement configuration, these lidars cannot be used to measure turbulence precisely.

1. Introduction

A theoretical model is developed to estimate the systematic errors in the second-order moments of wind speeds in the atmospheric surface layer measured by lidars. The systematic errors are those that arise resulting from the averaging effect in the sample or pulse volume and the relatively large circle in which Doppler lidars scan to obtain two-component horizontal wind profiles. Two types of lidars are considered, the ZephIR, developed by QinetiQ (Natural Power), as a continuous-wave (CW) lidar and the WindCube, developed by Leosphere as a pulsed lidar.[1] The verification is carried out by comparing the variances measured by the ZephIR and WindCube with that of the sonic anemometers placed at different heights on a meteorological mast.

Wind energy has expanded rapidly for several decades and every year thousands of multimegawatt wind turbines are being installed all over the world. The importance of wind speed measurements can never be overstated because the power produced from the wind turbine is directly proportional to the cube of the wind speed, at least below turbine-rated wind speeds. Atmospheric turbulence is one of the main inputs in assessing loads on the wind turbines. Thus, accurate estimation of wind speed and turbulence at several heights is crucial for the successful development of a wind farm. In wind energy, the current standard is the use of meteorological masts equipped with cup and/or sonic anemometers. However, tall meteorological masts are very expensive, and offshore the costs increase significantly. The advent of remote sensing devices like lidars gives a further boost to the development of wind energy. In recent years with the introduction of the ZephIR and WindCube, there has been a surge in the verification campaigns of comparing the lidar mean wind speed with that of a cup anemometer for wind energy applications (Smith et al.

---

[1] These lidars are not the second versions, WindCubeV2 and ZephIR 300, which were released in 2010, but the first versions of the instruments.

Corresponding author address: A. Sathe, L & R, Section Wind Energy, TU Delft, Kluyverweg 1, 2629 HS Delft, Netherlands.
E-mail: a.r.sathe@tudelft.nl

DOI: 10.1175/JTECH-D-10-05004.1

2006; Kindler et al. 2007; Courtney et al. 2008; Peña et al. 2009). Courtney et al. (2008) discuss the advantages and disadvantages of CW and pulsed lidars. To use a lidar as a standard measuring instrument in the future, for example, in the International Electrotechnical Commission (IEC) standards for loads (IEC 2005a,b) and power performance measurements (IEC 2005c), a fair degree of confidence is also required in the turbulence measurements.

Although lidars have been introduced in wind energy recently, for meteorology they have been investigated previously to measure turbulence using different scanning techniques. One of the first remote sensing (Doppler radar) turbulence studies using a full 360° scan in a horizontal plane was carried out by Browning and Wexler (1968), where the limitations of horizontal homogeneity and vertical wind shear are explained in detail. Wilson (1970) modified the technique from Browning and Wexler (1968) and performed turbulence measurements over snow. Kropfli (1986) extended the technique to accommodate turbulence scales of motion larger than those described in Wilson (1970) and showed that these techniques could be used to make reasonable estimates of turbulent kinetic energy and momentum flux by modeling the random errors in the measurements.

Eberhard et al. (1989) studied turbulence using Doppler lidar and modeled the random errors using a partial Fourier decomposition method, which gave better estimates of the errors than Wilson (1970) and Kropfli (1986). Gal-Chen et al. (1992) presented a technique for analyzing lidar data for turbulence measurements using the scans at two levels, and produced estimates of fluxes in the mixed layer and spectra of the horizontal velocity at the surface. Banakh et al. (1995) presented an analysis of estimating the random errors in the measurement of the mean wind speed by lidars using the theory of isotropic turbulence. Banta et al. (2002) studied the turbulence characteristics under the conditions of low-level jets, using the vertical slice scans of radial velocities. Smalikho et al. (2005) presented a method to use lidar data for the estimation of turbulent energy dissipation rate to study wake vortices of an aircraft. A comprehensive review is given in Engelbart et al. (2007), which covers different remote sensing techniques for turbulence measurements, including lidars. A review of the use of lidars for wind energy applications is also presented in Emeis et al. (2007). Pichugina et al. (2008) demonstrated the sensitivity of the streamwise velocity variance to the spatial and temporal averaging, also by using the technique of vertical slice scans of radial velocities. Recently, studies have been carried out to model the spatial averaging effects (Sjöholm et al. 2009) and compare the 3D turbulence measurements using three staring lidars (Mann et al. 2009). Wagner et al. (2009) modeled the systematic errors by approximating the conical scan and the scan time as a length scale, providing first estimates of the variances of the longitudinal component of wind velocity. Mann et al. (2010) estimated the momentum fluxes using lidars and modeled the unfiltered turbulence from the CW lidar, where the model compares reasonably well with the measurements. In the present work, line-of-sight averaging and the full extent of conical scanning is considered. An additional low-pass filter for the 3-s scan is also considered for the ZephIR.

In the remaining sections, the work is described in detail. Section 2 describes the theory, where the systematic error in the second-order moments is modeled for the ZephIR and WindCube. Section 3 provides details of the measurements used for comparison with the model. Section 4 describes the results along with some inferences. Section 5 gives a discussion on the systematic errors of the second-order moments, while section 6 provides a conclusion.

2. Theory

The model in this study is developed for the conical scanning and velocity–azimuth display (VAD) technique of data processing. The approach is similar to Wyngaard (1968) and Citriniti and George (1997), where turbulence measured by the hot-wire anemometer probe was modeled.

Figure 1 shows the lidar emitting the laser beam at different azimuth angles θ. The azimuth angles increase from 0° to 360° in the clockwise direction, as for the geographical convention. The line-of-sight velocity (also called radial velocity v_r) is measured by the lidar at each azimuth angle. The half-opening angle ϕ ($= 90° -$ elevation angle) is kept constant throughout the scan. The CW and pulsed lidars work on the principle of backscattering of the emitted radiation, and the subsequent detection of the Doppler shift in the frequency of the received radiation. The Doppler shift in the frequency is related to v_r by

$$\delta f = 2\frac{v_r}{\lambda}, \qquad (1)$$

where f and λ are the frequency and wavelength of the emitted radiation. Mathematically, v_r is given as the dot product of the unit directional vector and the velocity field at the point of focus for a CW lidar, and the center of the range gate (Lindelöw 2007) for the pulsed lidar,

$$v_r(\theta) = \mathbf{n}(\theta) \cdot \mathbf{v}[d_f \mathbf{n}(\theta)], \qquad (2)$$

where d_f is the focus distance for the CW lidar or the distance to the center of the range gate for the pulsed lidar at which the wind speeds are measured, $\mathbf{v} = (u, v, w)$

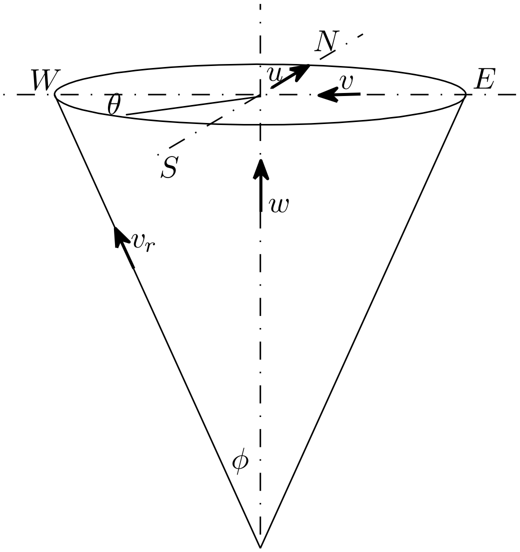

FIG. 1. Schematic of the velocity–azimuth display scanning.

is the instantaneous velocity field evaluated at the focus point or the center of the range gate $d_f\mathbf{n}(\theta)$, and $\mathbf{n}(\theta)$ is the unit directional vector given as

$$\mathbf{n}(\theta) = (\cos\theta \sin\phi, \sin\theta \sin\phi, \cos\phi). \qquad (3)$$

In practice it is impossible to obtain the backscattered radiation precisely from only the focus point, and there is always backscattered radiation of different intensities from different regions in space along the line of sight. Hence, it is necessary to assign appropriate weights to the backscattered intensity such that the weight corresponding to the focus point or the center of the range gate is the highest. Mathematically, the weighted average radial velocity can be written as

$$\tilde{v}_r(\theta) = \int_{-\infty}^{\infty} \varphi(s)\mathbf{n}(\theta) \cdot \mathbf{v}[s\mathbf{n}(\theta) + d_f\mathbf{n}(\theta)]\, ds, \qquad (4)$$

where $\varphi(s)$ is any weighting function, integrating to one, and s is the distance along the beam from the focus. For simplicity we assume that $s = 0$ corresponds to the focus distance.

Following are the main assumptions of our model:

(i) The terrain is homogeneous.
(ii) The flow field is frozen during the scan.
(iii) Equation (4) with an appropriately chosen $\varphi(s)$ models the averaging well.
(iv) The spatial structure of the turbulent flow is described well by the spectral tensor model of Mann (1994).

a. Systematic turbulence errors for the ZephIR lidar

The ZephIR transmits the laser beam through a constantly rotating prism, giving the required half-opening angle of nominally 30°. Each of up to five heights is scanned for 1 or 3 s, corresponding to one or three complete rotations of the prism. The beam is then refocused to the next height in the sequence and the scanning procedure is repeated. Up to five different heights can be selected, with the sequence (with five heights and 3-s scans) taking up to 18 s to complete. Thus, the lidar spends less than 20% of the time required to make a wind profile on any one of the five heights. A typical scan at each height consists of 50 measurements of v_r on the azimuth circle. If we assume the coordinate system such that u is aligned to the mean wind direction, v is perpendicular to the mean wind direction, w is the vertical component, and the mean wind comes from the north, then $\tilde{v}_r(\theta)$ can be expressed as

$$\tilde{v}_r(\theta) = A + B\cos\theta + C\sin\theta, \qquad (5)$$

where the coefficients $A = w_{qq}\cos\phi$, $B = u_{qq}\sin\phi$, and $C = v_{qq}\sin\phi$, and the sign ambiguity in $\tilde{v}_r(\theta)$ is neglected (see Mann et al. 2010). We use the subscript qq to denote the velocity components measured by ZephIR, because they are not the true velocity components u, v, and w. The assumption that the mean wind comes from the north is only made for simplicity. For a lidar measuring at many points on the azimuth circle the choice of the mean wind direction does not matter since averaging over the entire circle is carried out. The values of the coefficients A, B, and C are found using the least squares method by fitting Eq. (5) to the measured values of $\tilde{v}_r(\theta)$ at all scanned azimuth angles. The coefficients can be written as Fourier integrals,

$$A = \frac{1}{2\pi}\int_0^{2\pi} \tilde{v}_r(\theta)\, d\theta, \qquad (6)$$

$$B = \frac{1}{\pi}\int_0^{2\pi} \tilde{v}_r(\theta)\cos\theta\, d\theta, \qquad (7)$$

$$C = \frac{1}{\pi}\int_0^{2\pi} \tilde{v}_r(\theta)\sin\theta\, d\theta. \qquad (8)$$

We proceed by deriving expressions for the w_{qq} variance. The expressions for the (co)variances of the remaining components of wind velocity can be derived in a similar manner.

The variance of A is defined as $\sigma_A^2 = \langle A'^2\rangle$, where the angle brackets denotes ensemble averaging of a variable. From the above definition of A, we can write

$$\sigma_A^2 = \langle w'^2_{qq}\rangle \cos^2\phi. \qquad (9)$$

Using Eq. (6) we can also write,

$$\sigma_A^2 = \left\langle \left[\frac{1}{2\pi}\int_0^{2\pi} \tilde{v}'_r(\theta)\, d\theta\right]^2 \right\rangle. \tag{10}$$

Substituting $\tilde{v}_r(\theta)$ from Eq. (4) into Eq. (10), converting the square of the integral into a double integral, and interchanging the order of integration and averaging we get,

$$\begin{aligned}\sigma_A^2 &= \frac{1}{4\pi^2}\int_0^{2\pi}\int_0^{2\pi}\int_{-\infty}^{\infty}\int_{-\infty}^{\infty}\langle \mathrm{v}'_i[s_1\mathbf{n}(\theta_1) + d_f\mathbf{n}(\theta_1)]\mathrm{v}'_j[s_2\mathbf{n}(\theta_2) + d_f\mathbf{n}(\theta_2)]\rangle \varphi(s_1)\varphi(s_2)n_i(\theta_1)n_j(\theta_2)\, ds_1\, ds_2\, d\theta_1\, d\theta_2,\\ &= \frac{1}{4\pi^2}\int_0^{2\pi}\int_0^{2\pi}\int_{-\infty}^{\infty}\int_{-\infty}^{\infty} R_{ij}(\mathbf{r})\varphi(s_1)\varphi(s_2)n_i(\theta_1)n_j(\theta_2)\, ds_1\, ds_2\, d\theta_1\, d\theta_2,\end{aligned} \tag{11}$$

where $\langle \mathrm{v}'_i[s_1\mathbf{n}(\theta_1) + d_f\mathbf{n}(\theta_1)]\mathrm{v}'_j[s_2\mathbf{n}(\theta_2) + d_f\mathbf{n}(\theta_2)]\rangle = R_{ij}(\boldsymbol{r})$ is the covariance tensor separated by a distance $\mathbf{r} = [s_1\mathbf{n}(\theta_1) + d_f\mathbf{n}(\theta_1)] - [s_2\mathbf{n}(\theta_2) + d_f\mathbf{n}(\theta_2)]$ and is related to the three-dimensional spectral velocity tensor $\Phi_{ij}(\mathbf{k})$ by the inverse Fourier transform,

$$R_{ij}(\mathbf{r}) = \int \Phi_{ij}(\mathbf{k})e^{i\mathbf{k}\cdot\mathbf{r}}\, d\mathbf{k}, \tag{12}$$

where $\int d\mathbf{k} \equiv \int_{-\infty}^{\infty}\int_{-\infty}^{\infty}\int_{-\infty}^{\infty} dk_1\, dk_2\, dk_3$, $\mathbf{k} = (k_1, k_2, k_3)$ denotes the wave vector and the subscripts i, j take the values from 1 to 3. Inserting Eq. (12) into Eq. (11) we get,

$$\sigma_A^2 = \int \Phi_{ij}(\mathbf{k})\left\{\int_{-\infty}^{\infty}\varphi(s_1)\left[\frac{1}{2\pi}\int_0^{2\pi} n_i(\theta_1)e^{i(s_1+d_f)\mathbf{k}\cdot\mathbf{n}(\theta_1)}\, d\theta_1\right] ds_1\right\}\left\{\int_{-\infty}^{\infty}\phi(s_2)\left[\frac{1}{2\pi}\int_0^{2\pi} n_j(\theta_2)e^{i(s_2+d_f)\mathbf{k}\cdot\mathbf{n}(\theta_2)}\, d\theta_2\right] ds_2\right\} d\mathbf{k}. \tag{13}$$

Let $\alpha_i(\mathbf{k}) = \int_{-\infty}^{\infty}\varphi(s)[1/2\pi\int_0^{2\pi} n_i(\theta)e^{i(s+d_f)\mathbf{k}\cdot\mathbf{n}(\theta_1)}d\theta]ds$, which physically represents the line-of-sight and conical averaging. Equation (13) can then be written as (using Eq. 9),

$$\langle w'^2_{qq}\rangle \cos^2\phi = \int \Phi_{ij}(\mathbf{k})\alpha_i(\mathbf{k})\alpha_j^*(\mathbf{k})\, d\mathbf{k}, \tag{14}$$

where the asterisk denotes complex conjugation. Thus the integral reduces to evaluating $\alpha_i(\mathbf{k})$, since the analytical expressions for $\Phi_{ij}(\mathbf{k})$ are given in Mann (1994). Equation (16) can then be estimated numerically. For a CW lidar, $\varphi(s)$ is well approximated by a Lorentzian function (Sonnenschein and Horrigan 1971),

$$\varphi(s) = \frac{1}{\pi}\frac{l}{l^2 + s^2}, \tag{15}$$

where l is the Rayleigh length ($=\lambda_b d_f^2/\pi r_b^2$, where $\lambda_b = 1.55\ \mu$m is the wavelength of the emitted radiation, and $r_b = 19.5$ mm is the beam radius). An attempt has been made to obtain analytical expressions for $\alpha_i(\mathbf{k})$. However, no general analytical solution exists for $\alpha_i(\mathbf{k})$ and at most the integral can be reduced (by integrating over s) to

$$\alpha_i(\mathbf{k}) = \frac{1}{2\pi}e^{id_fk_3\cos\phi}\int_0^{2\pi} n_i(\theta + \theta_0)e^{id_fk_h\sin\phi\cos\theta}e^{-l|k_h\cos\theta\sin\phi + k_3\cos\phi|}\, d\theta, \tag{16}$$

where $k_h = \sqrt{k_1^2 + k_2^2}$ is the magnitude of the horizontal wave vector, $\cos\theta_0 = k_1/k_h$, $\sin\theta_0 = k_2/k_h$, and $n_i(\theta + \theta_0)$ is the component of the unit directional vector obtained from Eq. (3). Thus numerical integration has to be applied also for the evaluation of $\alpha_i(\mathbf{k})$.

A similar approach is taken for deriving u_{qq} and v_{qq} variances, where we obtain,

$$\langle u'^2_{qq}\rangle \sin^2\phi = \int \Phi_{ij}(\mathbf{k})\beta_i(\boldsymbol{k})\beta_j^*(\mathbf{k})\, d\mathbf{k}, \tag{17}$$

$$\langle v'^2_{qq}\rangle \sin^2\phi = \int \Phi_{ij}(\mathbf{k})\gamma_i(\mathbf{k})\gamma_j^*(\mathbf{k})\, d\mathbf{k}. \tag{18}$$

The corresponding β and γ functions are

$$\beta_i(\mathbf{k}) = \frac{1}{\pi}e^{id_fk_3\cos\phi}\int_0^{2\pi} n_i(\theta + \theta_0)\cos(\theta + \theta_0)e^{id_fk_h\sin\phi\cos\theta}e^{-l|k_h\cos\theta\sin\phi + k_3\cos\phi|}\, d\theta, \tag{19}$$

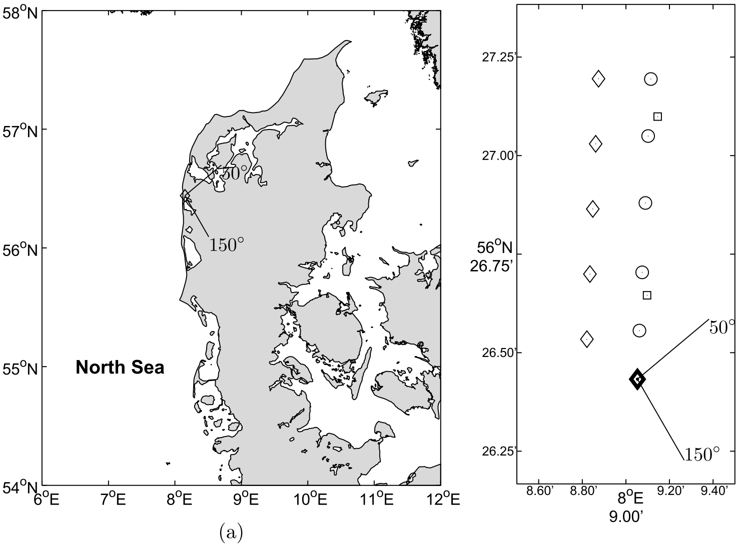

(a)

(b)

FIG. 2. Location of the Høvsøre meteorological mast and details of the site. The wind turbines (circles), light tower (squares), and the meteorological masts (diamonds) are shown. The meteorological mast from which the measurements are used is indicated (dark diamond) and the selected wind directions are also shown.

$$\gamma_i(\mathbf{k}) = \frac{1}{\pi} e^{id_f k_3 \cos\phi} \int_0^{2\pi} n_i(\theta + \theta_0) \sin(\theta + \theta_0)\, e^{id_f k_h \sin\phi \cos\theta} e^{-l|k_h \cos\theta \sin\phi + k_3 \cos\phi|}\, d\theta. \tag{20}$$

The derivation of the covariances is merely a combination of the weighting functions $\alpha_i(\mathbf{k})$, $\beta_i(\mathbf{k})$, and $\gamma_i(\mathbf{k})$, and their complex conjugates used with $\Phi_{ij}(\mathbf{k})$.

MODELING THE LOW-PASS FILTERING EFFECT RESULTING FROM THE 3-S SCAN

Because the ZephIR scans three circles in approximately 3 s, there will be a low-pass filter effect in turbulence measurements. We assume a length scale $L_f = \langle u \rangle \times 3\mathrm{s}$ such that it represents the 3-s averaging. We assume that the ZephIR scans a circle infinitely fast for 3 s. We model the corresponding filtering effect by a simple rectangular filter, such that,

$$f(x) = \begin{cases} \dfrac{1}{L_f} & \text{for} \quad |x| < \dfrac{L_f}{2}; \\ 0 & \text{elsewhere,} \end{cases} \tag{21}$$

where x is the center of the scanning circle and $f(x)$ is any function of x. The corresponding spectral transfer function is given as

$$\hat{T}_f(k_1) = \mathrm{sinc}^2\left(\frac{k_1 L_f}{2}\right), \tag{22}$$

where $\mathrm{sinc}(x) = \sin(x)/x$. The variances of u_{qq}, v_{qq}, and w_{qq} are given as

$$\langle u_{qq}'^2 \rangle \sin^2\phi = \int \Phi_{ij}(\mathbf{k})\beta_i(\mathbf{k})\beta_j^*(\mathbf{k})\hat{T}_f(k_1)\, d\mathbf{k}, \tag{23}$$

$$\langle v_{qq}'^2 \rangle \sin^2\phi = \int \Phi_{ij}(\mathbf{k})\gamma_i(\mathbf{k})\gamma_j^*(\mathbf{k})\hat{T}_f(k_1)\, d\mathbf{k}, \tag{24}$$

$$\langle w_{qq}'^2 \rangle \cos^2\phi = \int \Phi_{ij}(\mathbf{k})\alpha_i(\mathbf{k})\alpha_j^*(\mathbf{k})\hat{T}_f(k_1)\, d\mathbf{k}. \tag{25}$$

b. Systematic turbulence errors for the WindCube lidar

The assumption made in section 2a that the mean wind direction comes from the north cannot be made for the WindCube, because it measures at four azimuth

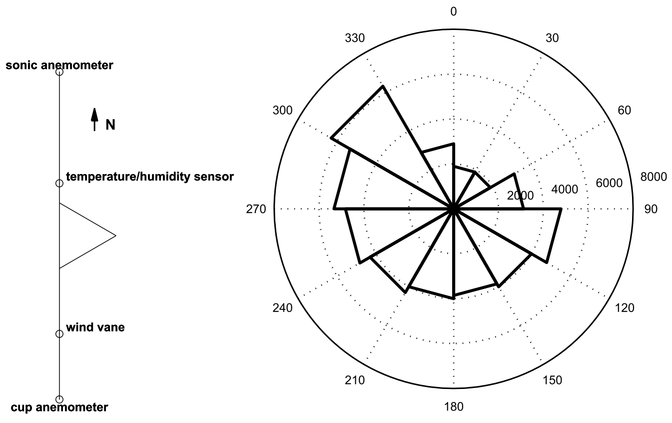

(a) Sensor Orientation (b) Wind Rose

FIG. 3. Orientation of the sensors on the meteorological mast and wind rose at 60 m. The numbers inside the circles are the number of 10-min observations.

angles only (cf. Fig. 1), for example, north, east, south and west. In this case the coordinate system is such that u is aligned in the mean wind direction. Thus,

$$u_{\mathrm{wc}} = u_{NS}\cos\Theta + u_{EW}\sin\Theta, \tag{26}$$

$$v_{\mathrm{wc}} = u_{NS}\sin\Theta - u_{EW}\cos\Theta, \tag{27}$$

where u_{NS} and u_{EW} denote wind speeds in the north–south and east–west directions, respectively, Θ denotes the wind direction, and the subscript wc denotes the velocity components measured by WindCube. From simple geometrical considerations (cf. Fig. 1),

$$u_{NS} = \frac{\tilde{v}_{rN} - \tilde{v}_{rS}}{2\sin\phi}, \tag{28}$$

$$u_{EW} = \frac{\tilde{v}_{rE} - \tilde{v}_{rW}}{2\sin\phi}, \tag{29}$$

where $\tilde{v}_{rN}$, $\tilde{v}_{rS}$, $\tilde{v}_{rE}$, and $\tilde{v}_{rW}$ are the weighted average radial velocities in the north, south, east and west directions, respectively. For the w component,

$$w_{\mathrm{wc}} = \frac{P(\tilde{v}_{rN} + \tilde{v}_{rS}) + Q(\tilde{v}_{rE} + \tilde{v}_{rW})}{2\cos\phi}, \tag{30}$$

where P and Q are the weights associated with the wind direction such that $P + Q = 1$. Leosphere uses

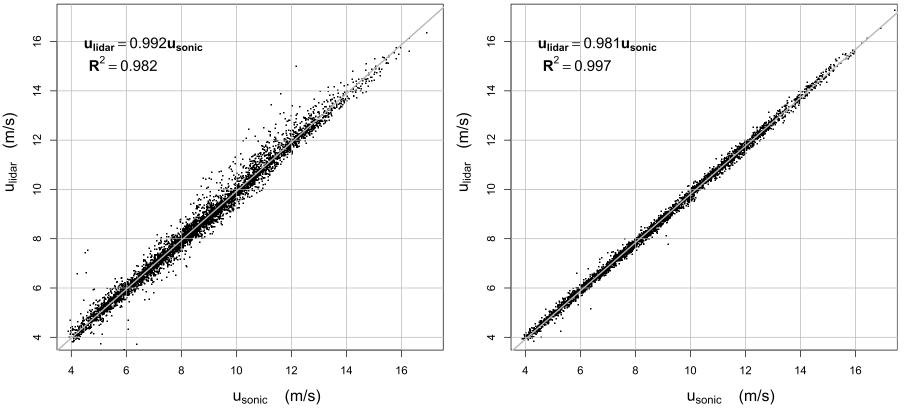

(a) ZephIR (b) WindCube

FIG. 4. Comparison of the mean wind speed measured by (left) lidars and (right) sonic anemometer.

$P = \cos^2\Theta$ and $Q = \sin^2\Theta$, and hence, we use the same in our calculations.

We proceed by deriving expressions for the $u_{\rm wc}$ variance. The expressions for the (co)variances of the remaining components of wind velocity can be derived in a similar manner. Substituting Eqs. (28) and (29) into Eq. (26), we get

$$u_{\rm wc} = \frac{1}{2\sin\phi}[(\tilde{\upsilon}_{rN} - \tilde{\upsilon}_{rS})\cos\Theta + (\tilde{\upsilon}_{rE} - \tilde{\upsilon}_{rW})\sin\Theta]. \tag{31}$$

We define unit vectors in the four directions as

$$\begin{aligned} \mathbf{n}_N &= \mathbf{n}(-\Theta), \\ \mathbf{n}_S &= \mathbf{n}(\pi - \Theta), \\ \mathbf{n}_E &= \mathbf{n}\left(\frac{\pi}{2} - \Theta\right), \\ \mathbf{n}_W &= \mathbf{n}\left(\frac{3\pi}{2} - \Theta\right), \end{aligned} \tag{32}$$

where $\mathbf{n}_N$, $\mathbf{n}_S$, $\mathbf{n}_E$, and $\mathbf{n}_W$ are the unit directional vectors in the north, south, east, and west directions, respectively. From Eq. (4), for the north direction,

$$\tilde{\upsilon}_{rN} = \int_{-\infty}^{\infty} \varphi(s)\mathbf{n}_N \cdot \mathbf{v}(s\mathbf{n}_N + d_f\mathbf{n}_N)\, ds. \tag{33}$$

To further simplify the notation we define the translation operator T_δ acting on any scalar or vector field $\xi(\mathbf{x})$,

$$T_\delta \xi(\mathbf{x}) = \xi(\mathbf{x} + \delta). \tag{34}$$

We also define a convolution operator $C_\mathbf{n}$ acting on any scalar or vector field as

$$C_\mathbf{n}\mathbf{v}(\mathbf{x}) = \int_{-\infty}^{\infty} \varphi(s)\mathbf{n} \cdot \mathbf{v}(\mathbf{x} + \mathbf{n}s)\, ds. \tag{35}$$

For the north direction, Eq. (33) can be written as

$$\tilde{\upsilon}_{rN} = C_{\mathbf{n}_N} T_{d_f\mathbf{n}_N}\mathbf{v}. \tag{36}$$

TABLE 1. Classification of atmospheric stability according to Monin–Obukhov length intervals

Very stable (vs)	$10 \le L_{\rm MO} \le 50$ m
Stable (s)	$50 \le L_{\rm MO} \le 200$ m
Near-neutral stable (nns)	$200 \le L_{\rm MO} \le 500$ m
Neutral (n)	$\lvert L_{\rm MO}\rvert \ge 50$ m
Near-neutral unstable (nnu)	$-500 \le L_{\rm MO} \le -200$ m
Unstable (u)	$-200 \le L_{\rm MO} \le -100$ m
Very unstable (vu)	$-100 \le L_{\rm MO} \le -50$ m

We get similar expressions for the south, east, and west directions. Equation (31) can then be written as

$$\begin{aligned} u_{\rm wc} = \frac{1}{2\sin\phi}[(&C_{\mathbf{n}_N} T_{d_f\mathbf{n}_N} - C_{\boldsymbol{n}_S} T_{d_f\mathbf{n}_S})\cos\Theta \\ &+ (C_{\mathbf{n}_E} T_{d_f\mathbf{n}_E} - C_{\mathbf{n}_W} T_{d_f\mathbf{n}_W})\sin\Theta]\mathbf{v} \end{aligned} \tag{37}$$

We also know that, by definition,

$$\langle u'^2\rangle = \int \langle \hat{u}(\mathbf{k})\hat{u}^*(\mathbf{k})\rangle\, d\mathbf{k}, \tag{38}$$

where ^ denotes the Fourier transform and * denotes complex conjugation. In the Fourier space we have

$$\widehat{T_\delta\mathbf{v}}(\mathbf{k}) = e^{i\mathbf{k}\cdot\delta}\hat{\mathbf{v}}(\mathbf{k}), \tag{39}$$

$$\widehat{C_{\boldsymbol{n}}\mathbf{v}}(\mathbf{k}) = \hat{\varphi}(\mathbf{n}\cdot\mathbf{k})\mathbf{n}\cdot\hat{\mathbf{v}}(\mathbf{k}), \tag{40}$$

where $\hat{\phi}(k) = \mathrm{sinc}^2(kl_p/2)$, considering that the weighting function for a pulsed lidar is commonly defined as

$$\varphi(s) = \begin{cases} \dfrac{l_p - |s|}{l_p^2} & \text{for} \quad |s| < l_p; \\ 0 & \text{elsewhere}, \end{cases} \tag{41}$$

where l_p is the half-length of the ideally rectangular light pulse leaving the lidar, assuming the matching time windowing ($=2l_p/c$, where c is the speed of light). In reality, the weighting function may be more rounded, but this will not affect the conclusions that are drawn. Thus, in Fourier space Eq. (37) can then be written as

$$\hat{u}_{\rm wc}(\mathbf{k}) = \frac{1}{2\sin\phi}\left\{\begin{matrix}[\mathbf{k}_N e^{id_f\mathbf{k}\cdot\mathbf{n}_N}\,\mathrm{sinc}^2(\mathbf{k}\cdot\mathbf{n}_N l_p/2) - \mathbf{n}_S e^{id_f\mathbf{k}\cdot\mathbf{n}_S}\,\mathrm{sinc}^2(\mathbf{k}\cdot\mathbf{n}_S l_p/2)]\cos\Theta \\ [\mathbf{n}_E e^{id_f\mathbf{k}\cdot\mathbf{n}_E}\,\mathrm{sinc}^2(\mathbf{k}\cdot\mathbf{n}_E l_p/2) - \boldsymbol{n}_W e^{id_f\mathbf{k}\cdot\mathbf{n}_W}\,\mathrm{sinc}^2(\mathbf{k}\cdot\mathbf{n}_W l_p/2)]\sin\Theta\end{matrix}\right\}\cdot\hat{\mathbf{v}}(\mathbf{k}) \equiv \mathbf{b}(\mathbf{k})\cdot\hat{\mathbf{v}}(\mathbf{k}), \tag{42}$$

and the variance [from Eq. (38)] as

$$\langle u'^2_{\rm wc}\rangle = \int \Phi_{ij}(\mathbf{k}) b_i(\mathbf{k}) b_j^*(\mathbf{k})\, d\mathbf{k}, \tag{43}$$

where we have implicitly used the relation $\Phi_{ij}(\mathbf{k}) = \langle \hat{\mathrm{v}}_i(\mathbf{k})\hat{\mathrm{v}}_j^*(\mathbf{k})\rangle$. The (co)variances of other components can be estimated in a similar manner by first estimating the

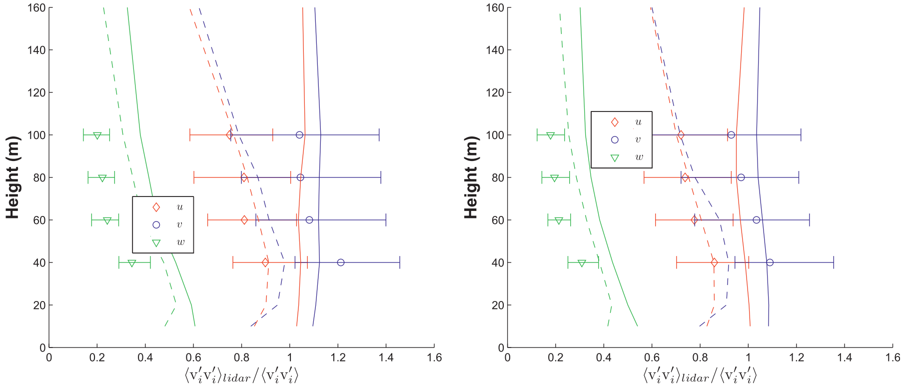

(a) very unstable (b) unstable

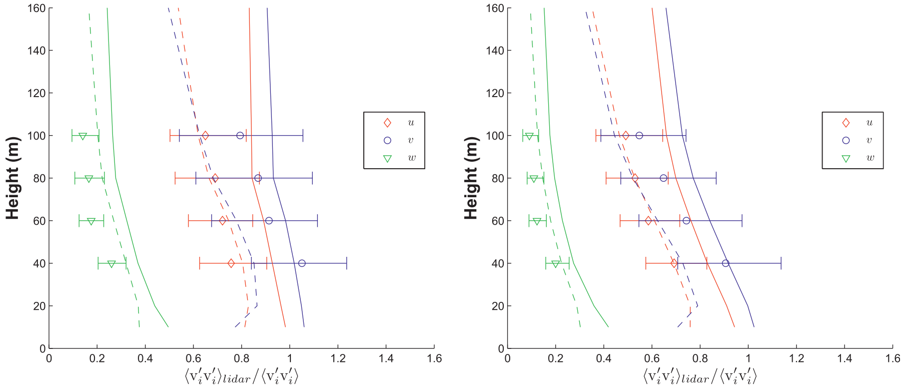

(c) near neutral unstable (d) neutral

FIG. 5. (a)–(g) ZephIR systematic errors under different atmospheric stability conditions in the eastern sector ranging from very unstable to very stable. The symbols indicate measurements. The solid lines are the theory without the low-pass filter, and the dashed lines are with the low-pass filter. The colored symbols represent the u (red diamonds), υ (blue circles), and w (green inverted triangles). The horizontal lines represent the error bars in the first and third quartile range.

corresponding weighting functions $c_i(\mathbf{k})$ and $a_i(\mathbf{k})$ for the υ_{wc} and w_{wc} components, respectively.

3. Description of the measurements

The measurements were performed at the Danish National Test Center for Large Wind Turbines at Høvsøre, Denmark. Figure 2 shows the layout of the test center and the location of the used reference meteorological mast, a 116.5-m-tall, intensively equipped mast located at the coordinates 56°26′26″N, 08°09′03″E, (indicated by a dark diamond in Fig. 2b). The site is about 2 km from the west coast of Denmark. The eastern sector is characterized by flat homogeneous terrain, and to the south is a lagoon.

Our reference measurements for this study are the sonic anemometer measurements taken at 40, 60, 80, and 100 m. The measured three-dimensional wind speeds are resolved with a frequency of 20 Hz and then reduced to the respective 10-min statistics (mean values and standard deviations or variances). All sonic anemometers are placed on the north booms of the meteorological mast (Fig. 3a), resulting in unusable data when the wind is from the south resulting from the wake of the mast. In combination with the sonic measurements, wind speeds from a ZephIR (coordinates 56°26′26.9556″N, 08°09′2.448″E) and a WindCube (coordinates 56°26′26.0556″N, 0.8°09′3.226″E) are used. The ZephIR is located about 35 m north of the meteorological mast and the WindCube is located about 11 m northwest of the meteorological mast. Reference and lidar data were collected over two different time periods: for the WindCube between January and April 2009, and for the ZephIR between April and November 2009. To further avoid the influence of the wakes from the wind turbines and the meteorological mast on

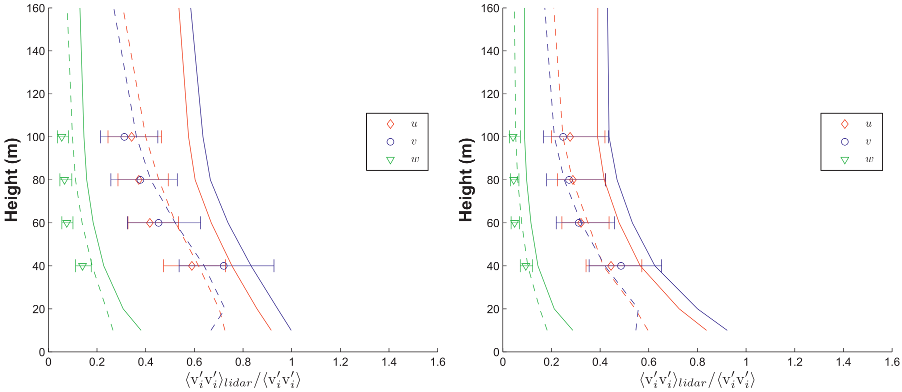

(e) near neutral stable

(f) stable

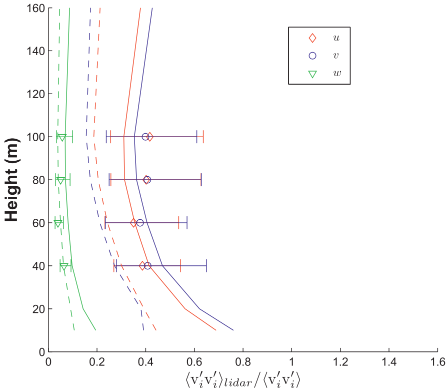

(g) very stable

FIG. 5. (*Continued*)

lidar measurements, and inhomogeneities resulting from the sudden change of roughness (the sea–land transition; see Fig. 2a), only data periods with easterly winds (50°–150°) are analyzed. Figure 3b shows that although the dominant wind direction is west-northwest, there is also sufficient data in the chosen directional (eastern) sector. For the ZephIR 5530 data points were used after using the entire filter, whereas for the WindCube 4003 data points were used.

The precision of the sonic anemometer measurements is estimated to be about ±1.5%. From comparisons with cup anemometers, the mean error of the WindCube in typical flat coastal conditions is within ±0.05 m s^{-1}, with a standard deviation in mixed shear conditions of about 0.15 m s^{-1}. The corresponding uncertainty for the measurements made with a ZephIR is slightly higher [a detailed list of different error sources is given in Lindelöw-Marsden (2007)].

Figure 4 shows the comparison of the 10-min mean horizontal wind speed (at 100 m) measured by the ZephIR and WindCube with the sonic anemometer. Data are shown for the easterly winds (50°–150°) and reference mean wind speeds between 4 and 25 m s^{-1}. To guarantee repeatable conditions the data were furthermore filtered with respect to rain (i.e., only 10-min periods with no precipitation were considered) and the availability of the lidar (i.e., 100% of the fast data within a 10-min period had to be available). The lidar observations agree reasonably well with those of the sonic anemometer, with coefficients of determination $R^2 > 0.98$, where the data of the WindCube shows a significantly better correlation than those of the ZephIR.

4. Comparison of models with the measurements

The estimation of Φ_{ij} using the model from Mann (1994) requires three input parameters: $\alpha\epsilon^{2/3}$, which is a product of the spectral Kolmogorov constant α (Monin and Yaglom 1975) and the rate of viscous dissipation of specific turbulent kinetic energy $\epsilon^{2/3}$; a length scale L, and an anisotropy parameter Γ. We use these input parameters obtained by fitting the sonic anemometer measurements under different atmospheric stability conditions at several heights on the meteorological mast in the eastern sector (Peña et al. 2010). The classification of atmospheric stability (Table 1) is based on the Monin–Obukhov length (L_{MO}) intervals (Gryning et al. 2007).

Here, L_{MO} is estimated using the eddy covariance method (Kaimal and Finnigan 1994) from the high-frequency (20 Hz) measurements at 20 m. Mathematically, L_{MO} is given as

$$L_{\mathrm{MO}} = -\frac{u_*^3 T}{\kappa g \overline{w'\theta_v'}}, \tag{44}$$

where u_* is the friction velocity, $\kappa = 0.4$ is the von Kármán constant, g is the acceleration resulting from gravity, T is the absolute temperature, θ_v is the virtual potential temperature, and $\overline{w'\theta_v'}$ (covariance of w and θ_v) is the virtual kinematic heat flux; u_* is estimated as

$$u_* = \sqrt[4]{\overline{u'w'}^2 + \overline{v'w'}^2}, \tag{45}$$

where $\overline{u'w'}$ (covariance of u and w) and $\overline{v'w'}$ (covariance of v and w) are the vertical fluxes of the horizontal momentum.

a. Definition of the systematic error

For simplicity we define systematic error as the ratio of the lidar to the true second-order moment. Thus, a ratio equal to one would signify no systematic error, whereas deviations from unity signify systematic error. By definition, the true second-order moment of a velocity component is given as

$$\langle \mathrm{v}_j' \mathrm{v}_j' \rangle = \int \Phi_{ij}(\mathbf{k})\, d\mathbf{k}. \tag{46}$$

The theoretical systematic errors are calculated by taking the ratio of lidar second-order moments [Eqs. (14), (17), (18), and (42)] to the true second-order moment [Eq. (46)]. The numerical integration is carried out using an adaptive algorithm (Genz and Malik 1980). For experimental comparison, the second-order moments measured by sonic anemometers are considered to be true second-order moments. Thus, experimentally, the systematic errors are estimated by taking the ratio of the measured lidar second-order moments to sonic second-order moments.

b. Comparison with the ZephIR measurements

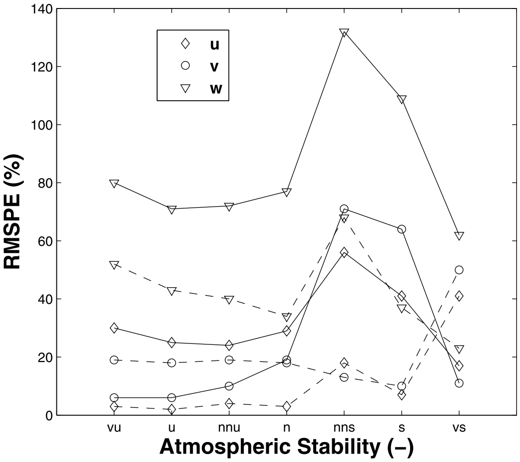

FIG. 6. Root-mean-square percent error (RMSPE) in the prediction of the systematic errors for the ZephIR. The model without the low-pass filter (solid line) and the model with the low-pass filter (dashed line) are shown. See Table 1 for the meaning of the abbreviations on the x axis. Symbols as in Fig. 5.

Figure 5 shows the comparison of the modeled and measured systematic errors for u, v, and w variances over 10-min periods. The theoretical points are shown both with and without the low-pass filter. For the low-pass filter, the model is dependent on the mean wind speed and the plots are shown for $\langle u \rangle = 9\ \mathrm{m\ s^{-1}}$ at all heights, because this is the mean wind speed at Høvsøre. The measurements are represented as median (markers), and first and third quartiles (error bars), respectively. We infer the following:

- The systematic errors vary considerably under different atmospheric stability conditions: the variation is up to 50% for u and v variances, and up to 20% for w variance. This is due to a large variation in the length scales of different velocity components resulting in varying attenuation of the variances.
- The systematic errors increase with height under all atmospheric stability conditions; this is due to a quadratic increase in the sample volume with height (Lindelöw 2007). The diameter of the scanning circle also increases with height.
- The systematic errors in w variance are much larger (approximately 3–5 times) than that of the u and v variances; this is due to the very small length scales of the w component as compared to those for u and v, resulting in the attenuation of the w variance of up to 90%. The u and v variances are attenuated up to 70%.
- There is a significant spread (first and third quartiles) in the systematic errors of u and v variances; these are the random errors and most likely occur because of the disjunctive sampling (Lenschow et al. 1994) of the ZephIR.

A thorough scientific investigation is needed to quantify random errors, but is not the focus of this paper.

- The trend of the systematic errors predicted by both models is in agreement with the observations at all heights.
- With the exception of very stable conditions, the model with the low-pass filter [Eqs. (23)–(25)] is in better agreement with the measurements at all heights than without the low-pass filter.

To quantify the improvement in the model predictions using the low-pass filter, we compute the root-mean-square percent errors (RMSPE) between the measured and the modeled systematic errors for each stability condition. RMSPE is given as

$$\mathrm{RMSPE} = \sqrt{\frac{1}{n}\sum\left[\frac{\left(\frac{\langle \mathrm{v}_i' \mathrm{v}_i'\rangle_{\mathrm{lidar}}}{\langle \mathrm{v}_i' \mathrm{v}_i'\rangle}\right)_{\mathrm{measured}} - \left(\frac{\langle \mathrm{v}_i' \mathrm{v}_i'\rangle_{\mathrm{lidar}}}{\langle \mathrm{v}_i' \mathrm{v}_i'\rangle}\right)_{\mathrm{modelled}}}{\left(\frac{\langle \mathrm{v}_i' \mathrm{v}_i'\rangle_{\mathrm{lidar}}}{\langle \mathrm{v}_i' \mathrm{v}_i'\rangle}\right)_{\mathrm{measured}}}\right]^2} \times 100, \qquad (47)$$

where median values are used for the measurements.

Figure 6 shows the comparison of the RMSPE in the prediction of the systematic errors with and without the low-pass filter for the ZephIR. A significant decrease in the RMSPE (of the order of 30%) of u and w variances is observed under all atmospheric stabilities (except for the very stable condition for u variance) when the low-pass filtering is used. For the v variance, there is a slight increase (up to 10%) in the RMSPE under unstable conditions, whereas for stable conditions a decrease of up to 40% is observed. Thus, in general, using the low-pass filter, the model predicts the systematic errors better than without using the low-pass filter. We also performed the calculations using the beam radius r_b = 24 mm, and observed that the RMSPE for all three variance components changes only slightly (±5%).

c. *Comparison with the WindCube measurements*

Figure 7 shows the comparison of the modeled and measured systematic errors (section 2a) for u, v, and w variances over 10-min periods. We infer the following:

- The systematic errors vary considerably under different atmospheric stability conditions: the variation is up to 50% for u and v variances, and up to 20% for the w variance. The same is also observed for the ZephIR.
- The systematic errors decrease with height for the u and v variances under all atmospheric stability conditions: for the WindCube, the probe length is constant (Lindelöw 2007), and, hence, at lower heights there is a combined averaging effect resulting from the probe length and the diameter of the scanning circle. Considering that at lower heights the length scales are smaller than at higher heights, it is likely that the variances are attenuated greater at lower heights than at higher heights. For w variance, the systematic error is approximately constant, and is most likely due to the small length scales.
- The systematic error in w variance is much larger (approximately 3–5 times) than that of the u and v variances. The same is also observed for the ZephIR.
- The spread in the systematic error (first and third quartiles) of the u and v variances is smaller than that of the ZephIR; this is most likely because the WindCube updates the velocity vector approximately every 6.5 s, whereas the ZephIR updates every 18 s.
- The systematic error varies significantly with the wind direction relative to the beam direction for w variance, and to a lesser degree for u and v variance under all stability conditions.

Figure 8 shows the comparison of the RMSPE in the prediction of the systematic errors for the WindCube and ZephIR (with the low-pass filter). It is observed that for u and v variances, with the exception of the near-neutral stable condition, the RMSPE in both lidars is approximately equal. There is a considerable variation in the RMSPE for the w variance. This is most likely because for the WindCube, the w variance is very sensitive to the wind direction because of its cosine and sine dependence. In general, for both lidars, except for the very stable condition, the model predicts the systematic errors for u variance reasonably well (RMSPE ≈ 6%), followed by v variance (RMSPE ≈ 12%). It is difficult to say whether the prediction for the w variance is less reliable or not (RMSPE of the order of 60%).

We do not model the filtering effect because of the scanning time (≈6.5 s) of WindCube for two reasons:

(i) Since the measurement is carried out at only four points, with each lasting 0.5 s on the scanning circle, we cannot assume that the WindCube measures infinitely fast on the scanning circle (as we did for the ZephIR). The translations in each direction have

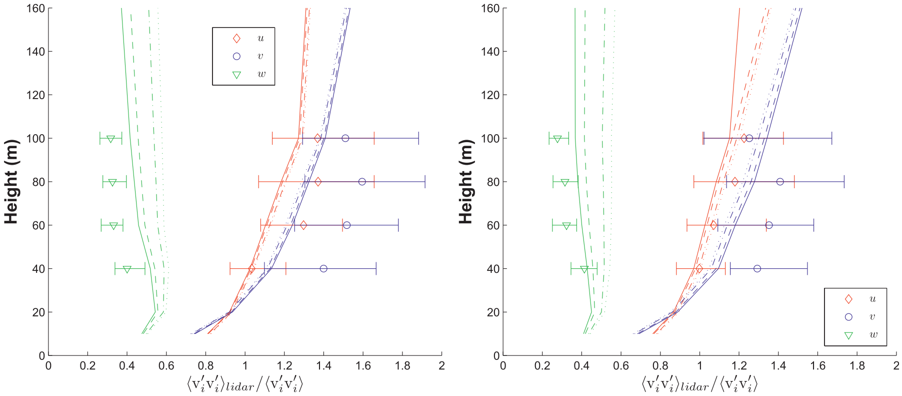

(a) very unstable

(b) unstable

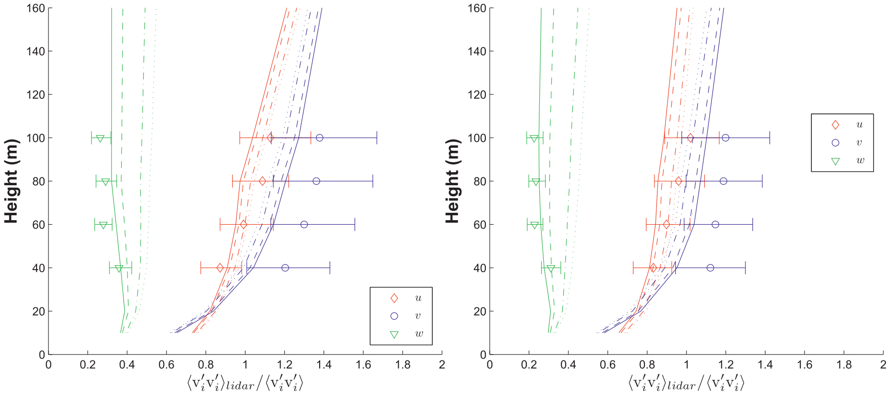

(c) near neutral unstable

(d) neutral

FIG. 7. As in Fig. 5, but for WindCube systematic errors. Here, the model variation with wind direction is plotted for 0° (dotted line), 15° (dash–dot line), 30° (dashed line), and 45° (solid line).

to be convolved with the corresponding spectral transfer function, if the filtering is to be included.

(ii) The calculation becomes too cumbersome if the above procedure is followed.

5. Discussion

The main goal of this paper is to understand the systematic errors in the second-order moments of CW and pulsed lidars. In particular, we model the systematic errors for the ZephIR and WindCube, which are used as CW and pulsed lidars, respectively. Although the model is developed for specific lidars, the modeling framework would be the same for any other instrument. Additionally, we also model the low-pass filter for the 3-s scan in the ZephIR. We expected a large variation in the systematic errors under different atmospheric stability conditions and, hence, performed the analysis accordingly. Figures 5 and 7 indeed justify our analysis.

In general, except for the very stable conditions, the model predicts the systematic errors quite well, where the RMSPE for the *u* and *υ* variances are of the order of 4% and 15%, respectively. For the ZephIR, when the low-pass filter is not used then the RMSPE is quite large (of the order of 30%) for the *u* variance. For the *w* variance, the high values of RMSPE (of the order of 60%) under all atmospheric stability conditions are observed. We think that the following two reasons could contribute to this:

(i) The attenuation in the *w* variance is quite large (up to 90%), as compared to the *u* and *υ* variances (up to 70%). Thus, a small difference in the model prediction and the measurements results in amplifying the RMSPE.

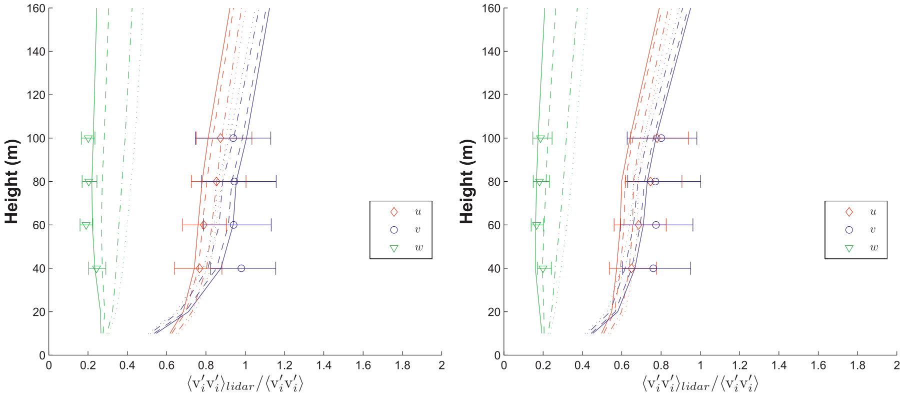

(e) near neutral stable

(f) stable

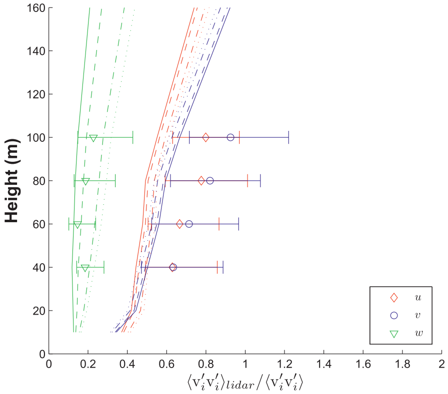

(g) very stable

FIG. 7. (*Continued*)

(ii) For the ZephIR, when the low-pass filter is used in the model, there is a dependence on the mean wind speed. The model results (Fig. 5) are shown for $\langle u \rangle = 9\ \mathrm{m\ s^{-1}}$ only. Segregating the model and observations for different mean wind speeds will result in reducing the RMSPE.

For the WindCube, the model predicts a significant variation of the w variance with wind direction [Eq. (30)]. To estimate the influence of the weights P and Q on the prediction of systematic errors, we calculate $\langle w'^2_{\mathrm{wc}} \rangle$ from the equation for w that corresponds to Eq. (38) with two different ways of calculating w. The first is the formula used by Leosphere, for example, Eq. (30), with $P = \cos^2\Theta$ and $Q = \sin^2\Theta$; the second is $P = Q = ½$. The former is shown as a thin solid line in Fig. 9 and the latter as a thin dashed line. The spectral tensor parameters used are for neutral atmospheric stability from Peña et al. (2010) at 100 m. The measurements of $\langle w'^2_{\mathrm{wc}} \rangle / \langle w'^2 \rangle$, shown as broad curves on Fig. 9, are from the same height, and both measurements and theory show that $\langle w'^2_{\mathrm{wc}} \rangle / \langle w'^2 \rangle$ using Leosphere's choice of P and Q can vary by a factor of 2 solely by changing the wind direction. If $P = Q = ½$ is chosen, then the reduction of the vertical velocity variance does vary much less with wind direction, but the overall attenuation is stronger.

Because the model predicts the trend in the systematic errors in the w variance reasonably well (Figs. 5 and 7), qualitatively it could be said that the model also agrees well with the measurements for the w variance.

While comparing the performance of our model, the following should also be considered:

- The model is dependent on the three-dimensional spectral velocity tensor (Mann 1994), which is strictly valid for neutral conditions only. Thus, one has to be careful while comparing under different atmospheric stability conditions. In this study, we have reduced the uncertainty by using the three input tensor parameters that are fitted to the measurements under

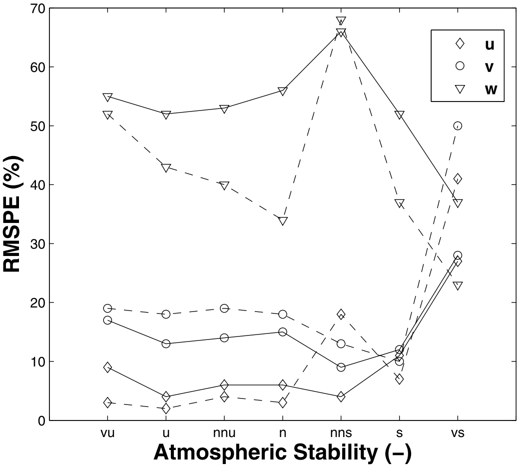

FIG. 8. Comparison of the RMSPE in the prediction of the systematic errors for the WindCube and ZephIR. The WindCube (solid line) and ZephIR (dashed line) with the low-pass filter are shown. See Table 1 for the meaning of the abbreviations on the *x* axis.

different atmospheric stability conditions (Peña et al. 2010).

- While using Eqs. (23)–(25), we have used the same mean wind speed at all heights. In reality, there is always wind shear, which also depends significantly on atmospheric stability (Motta and Barthelmie 2005). However, the calculations will become too cumbersome, and hence we made a crude approximation.
- The very stable conditions are generally difficult to analyze. There could be different reasons for the large deviation in the *u* and *v* variances; for example, uncertainty in the input tensor parameters, and lack of validity of the spectral tensor model (Mann 1994) under different atmospheric stability conditions
- Also, contrary to expectation, the measurements under very stable conditions (Figs. 5 and 8) show a decrease in the systematic errors for the *u* and *v* variances, as compared to the stable conditions.

There is also some room for reducing redundancy in the ZephIR measurements, which might reduce the spread of the systematic errors (quartile range). Instead of scanning at several points on the circle, only four points are required. Reducing the measurement points would increase the dependence of the second-order moments on the wind direction (cf. section 2). However, it would considerably reduce the time required for completing a VAD. There is also no need to scan the circle 3 times; for example, in the present configuration, 50 points are scanned in approximately 1 s. Thus, four points would take only 0.08 s. If it measures five heights sequentially, then the next measurement would be after 0.4 s, giving a measurement frequency of $\gtrsim$2 Hz. Alternatively, at each of the four points the scans can also be performed rapidly at different heights sequentially before scanning the next point.

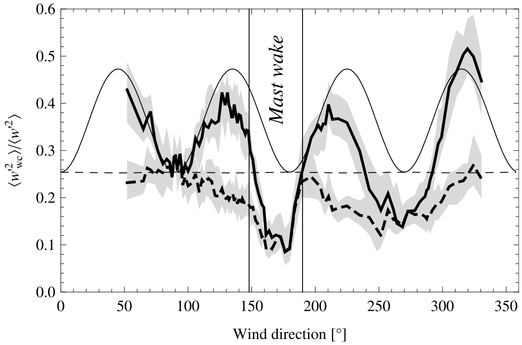

FIG. 9. The ratio of the vertical velocity variance as measured by the WindCube and the actual variance measured and modeled at 100 m. The theoretical expectations (thin lines) using $P = \cos^2\Theta$ and $Q = \sin^2\Theta$ (solid line) and $P = Q = ½$ (dashed line) in Eq. (30) are shown. The corresponding measurements are shown (broad curves), with the first and third quartiles displayed (shades).

We are currently looking into alternative ways of analyzing the lidar data and different beam configurations that would render turbulence measurements more feasible. One idea is to use two different half opening angles as in Eberhard et al. (1989), who show that all terms in the Reynolds stress tensor can be obtained by using the single-beam statistics, without resorting to beam covariances, which is done in this paper. That would require significant hardware modifications to the instruments treated here. Another idea is to supplement the analysis with information on the width of the Doppler spectra, as done for the momentum flux in Mann et al. (2010), in order to compensate for the effect of along-beam averaging.

6. Conclusions

The systematic errors of the second-order moments measured by lidars using the conical scanning and VAD technique to process the data are quite large because of

(i) the spatial separation of the data points along the line-of-sight and
(ii) the spatial separation of the data points in the conical section.

Also, from Eqs. (14), (17), (18), and (43), the general lidar equation for the second-order moments using the VAD data processing technique can be written as

$$\langle \mathrm{v}'_m \mathrm{v}'_n \rangle_{\text{lidar}} = \int \Phi_{ij}(\mathbf{k}) X_i^m(\mathbf{k}) X_j^{n*}(\mathbf{k})\, d\mathbf{k};$$

$$X_i^m(\mathbf{k}) = \begin{cases} \beta_i(\mathbf{k}) \wedge b_i(\mathbf{k}), & m = 1 \\ \gamma_i(\mathbf{k}) \wedge c_i(\mathbf{k}), & m = 2\,. \\ \alpha_i(\mathbf{k}) \wedge a_i(\mathbf{k}), & m = 3 \end{cases} \tag{48}$$

The weighting functions $\alpha_i(\mathbf{k})$, $\beta_i(\mathbf{k})$, and $\gamma_i(\mathbf{k})$ are used for the ZephIR and $a_i(\mathbf{k})$, $b_i(\mathbf{k})$, and $c_i(\mathbf{k})$ are used for the WindCube. Thus, the measurement of the second-order moment by lidar involves interaction of all components of the spectral velocity tensor $\Phi_{ij}(\mathbf{k})$ weighted by the corresponding weighting functions $X_i^m(\mathbf{k})$. It is to be noted that Eq. (48) is given in Einstein summation convention, and, hence, in order to explicitly see the contribution of all components of $\Phi_{ij}(\mathbf{k})$ on the measurement of the second-order moments by lidar, this equation must be expanded for all values of the subscripts i and j. In most cases, this results in the attenuation of the second-order moments, whereas in some cases this also results in amplification of the second-order moment, for example, as observed for the WindCube in the unstable conditions (see Fig. 7).

Finally, to answer the question posed in the title "Can wind lidars measure turbulence?", it is clear that using the conical scanning and VAD technique to process the data they cannot be used to measure turbulence precisely.

Acknowledgments. This study is a part of the Ph.D. project under the We@Sea program, BISK-03041, and sponsored by the Dutch Ministry of Economic affairs. The experimental results are all based on data collected at the Høvsøre Test Station under the watchful eyes of Anders Ramsing Vestergaard and Bjarne Sønderskov. We extend our thanks to them for their highly professional and good-humored assistance. We are also obliged to the NORSEWInD project and its leader Andy Oldroyd, under whose auspices the lidar data were obtained. Finally, we are grateful for valuable comments from Torben Mikkelsen, Risø DTU. This paper has been prepared using resources provided by the EU FP6 UpWind project (Project reference 019945 SES6) and by the Center for Computational Wind Turbine Aerodynamics and Atmospheric Turbulence funded by the Danish Council for Strategic Research Grant 09-067216.

REFERENCES

Banakh, V. A., I. N. Smalikho, F. Köpp, and C. Werner, 1995: Representativeness of wind measurements with a CW Doppler lidar in the atmospheric boundary layer. *Appl. Opt.,* **34,** 2055–2067.

Banta, R. M., R. K. Newsom, J. K. Lundquist, Y. L. Pichugina, R. L. Coulter, and L. Mahrt, 2002: Nocturnal low-level jet characteristics over Kansas during CASES-99. *Bound.-Layer Meteor.,* **105,** 221–252.

Browning, K. A., and R. Wexler, 1968: The determination of kinematic properties of a wind field using a Doppler radar. *J. Appl. Meteor.,* **7,** 105–113.

Citriniti, J. H., and W. K. George, 1997: The reduction of spatial aliasing by long hot-wire anemometer probes. *Exp. Fluids,* **23,** 217–224.

Courtney, M., R. Wagner, and P. Lindelow, 2008: Testing and comparison of lidars for profile and turbulence measurements in wind energy. *Proc. 14th Int. Symp. for the Advancement of Boundary Layer Remote Sensing,* Vol. 1, Risø DTU, Denmark, IOP Conference Series: Earth and Environmental Science, 012021.

Eberhard, W. L., R. E. Cupp, and K. R. Healy, 1989: Doppler lidar measurements of profiles of turbulence and momentum flux. *J. Atmos. Oceanic Technol.,* **6,** 809–819.

Emeis, S., M. Harris, and R. M. Banta, 2007: Boundary-layer anemometry by optical remote sensing for wind energy applications. *Meteor. Z.,* **16,** 337–347, doi:10.1127/0941-2948/2007/0225.

Engelbart, D. A. M., M. Kallistratova, and R. Kouznetsov, 2007: Determination of the turbulent fluxes of heat and momentum in the ABL by ground-based remote-sensing techniques (a review). *Meteor. Z.,* **16,** 325–335, doi:10.1127/0941-2948/2007/0224.

Gal-Chen, T., M. Xu, and W. L. Eberhard, 1992: Estimation of atmospheric boundary layer fluxes and other turbulence parameters from Doppler lidar data. *J. Geophys. Res.,* **97** (D17), 18 409–18 423.

Genz, A. C., and A. A. Malik, 1980: An adaptive algorithm for numerical integration over an n-dimensional rectangular region. *J. Comput. Appl. Math.,* **6** (4), 295–302.

Gryning, S.-E., E. Batchvarova, B. Brümmer, H. Jørgensen, and S. Larsen, 2007: On the extension of the wind profile over homogeneous terrain beyond the surface layer. *Bound.-Layer Meteor.,* **124,** 251–268, doi:10.1007/s10546-007-9166-9.

IEC, 2005a: Wind turbines—Part I: Design requirements. International Electrotechnical Commission IEC 61400-1, 92 pp.

——, 2005b: Offshore wind turbines—Part I: Design requirements. International Electrotechnical Commission IEC 61400-3, 136 pp.

——, 2005c: Wind turbines—Part 12-1: Power performance measurements of electricity producing wind turbines. International Electrotechnical Commission IEC 61400-12-1, 90 pp.

Kaimal, J. C., and J. J. Finnigan, 1994: Acquisition and processing of atmospheric boundary layer data. *Atmospheric Boundary Layer Flows,* Oxford University Press, 255–257.

Kindler, D., A. Oldroyd, A. Macaskill, and D. Finch, 2007: An eight month test campaign of the QinetiQ ZephIR system: Preliminary results. *Meteor. Z.,* **16** (5), 479–489, doi:10.1127/0941-2948/2007/0226.

Kropfli, R. A., 1986: Single Doppler radar measurement of turbulence profiles in the convective boundary layer. *J. Atmos. Oceanic Technol.,* **3,** 305–314.

Lenschow, D. H., J. Mann, and L. Kristensen, 1994: How long is long enough when measuring fluxes and other turbulence statistics? *J. Atmos. Oceanic Technol.,* **11,** 661–673.

Lindelöw, P., 2007: Fibre based coherent lidars for remote wind sensing. Ph.D. thesis, Technical University Denmark, 164 pp.

Lindelöw-Marsden, P., 2007: UpWind D1: Uncertainties in wind assessment with LIDAR. Risø DTU Tech. Rep. Risø-R-1681(EN), 55 pp.

Mann, J., 1994: The spatial structure of neutral atmospheric surface-layer turbulence. *J. Fluid Mech.,* **273,** 141–168.

——, A. Pena, F. Bingöl, R. Wagner, and M. S. Courtney, 2010: Lidar scanning of momentum flux in and above the surface layer. *J. Atmos. Oceanic Technol.,* **27,** 792–806.

——, and Coauthors, 2009: Comparison of 3D turbulence measurements using three staring wind lidars and a sonic anemometer. *Meteor. Z.,* **18** (2), 135–140, doi:10.1127/0941-2948/2009/0370.

Monin, A. S., and A. M. Yaglom, 1975: *Statistical Fluid Mechanics*. Vol. 2. MIT Press, 886 pp.

Motta, M., and R. J. Barthelmie, 2005: The influence of nonlogarithmic wind speed profiles on potential power output at Danish offshore sites. *Wind Energy,* **8,** 219–236.

Peña, A., S.-E. Gryning, and J. Mann, 2010: On the length scale of the wind profile. *Quart. J. Roy. Meteor. Soc.,* **136** (653), 2119–2131.

——, C. B. Hasager, S.-E. Gryning, M. Courtney, I. Antoniou, and T. Mikkelsen, 2009: Offshore wind profiling using light detection and ranging measurements. *Wind Energy,* **12,** 105–124, doi:10.1002/we.283.

Pichugina, Y. L., R. M. Banta, N. D. Kelly, B. J. Jonkman, S. C. Tucker, R. K. Newsom, and W. A. Brewer, 2008: Horizontal-velocity and variance measurements in the stable boundary layer using Doppler lidar: Sensitivity to averaging procedures. *J. Atmos. Oceanic Technol.,* **25,** 1307–1327.

Sjöholm, M., T. Mikkelsen, J. Mann, K. Enevoldsen, and M. Courtney, 2009: Spatial averaging-effects on turbulence measured by a continuous-wave coherent lidar. *Meteor. Z.,* **18** (3), 281–287, doi:10.1127/0941-2948/2009/0379.

Smalikho, I., F. Kopp, and S. Rahm, 2005: Measurement of atmospheric turbulence by 2- μm Doppler lidar. *J. Atmos. Oceanic Technol.,* **22,** 1733–1747.

Smith, D. A., M. Harris, A. S. Coffey, T. Mikkelsen, H. E. Jørgensen, J. Mann, and R. Danielian, 2006: Wind lidar evaluation at the Danish wind test site in Høvsøre. *Wind Energy,* **9,** 87–93, doi:10.1002/we.193.

Sonnenschein, C. M., and F. A. Horrigan, 1971: Signal-to-noise relationships for coaxial systems that heterodyne backscatter from atmosphere. *Appl. Opt.,* **10,** 1600–1604.

Wagner, R., T. Mikkelsen, and M. Courtney, 2009: Investigation of turbulence measurements with a continuous wave, conically scanning lidar. Risø DTU Tech. Rep. Risø-R-1682(EN), 22 pp.

Wilson, D. A., 1970: Doppler radar studies of boundary layer wind profiles and turbulence in snow conditions. *Proc. 14th Conf. on Radar Meteorology,* Tucson, AZ, Amer. Meteor. Soc., 191–196.

Wyngaard, J. C., 1968: Measurement of small-scale turbulence structure with hot wires. *J. Sci. Instrum.,* **1,** 1105–1108.

Chapter 6

Measurement of turbulence spectra using a scanning pulsed wind lidar

In chapter 5 we modelled the systematic errors that arise in turbulence measurements by lidars using the VAD scanning technique. Turbulence was quantified in the form of the diagonal components of the Reynolds stress tensor. The systematic error was quantified in the form of ratio between the lidar and sonic measured turbulence. A basic question that arises out of that work is, can we use a simple transfer function, where the lidar measured Reynolds stress tensor is divided by the corresponding systematic error in order to retrieve the true Reynolds stress tensor? To answer this, we need to understand how turbulent energy is distributed over a range of wavenumbers. This is because any component of the Reynolds stress tensor is simply the area under the (Co-) spectral curve.

In this chapter we model the turbulence spectra as measured by a scanning pulsed (WindCube) wind lidar using basic principles. The model is obtained for the case where the mean wind direction is aligned with the lidar beams. Nevertheless the same framework can be used to model for any arbitrary wind directions. Just as in chapter 5 the model makes use of the Mann [1994] model to describe the three-dimensional turbulence structure. Comparison of the model with the measurements is carried out at two heights. Having understood the distribution of spectral energy with respect to the wavenumbers, the implications of using the scanning pulsed wind lidar for wind energy purposes can also be evaluated. Moreover, it could be used to understand how a scanning pulsed wind lidar measures gusts, since the gust factor is a function of turbulence spectral moments [Rice, 1944, 1945].

JOURNAL OF GEOPHYSICAL RESEARCH, VOL. ???, XXXX, DOI:10.1029/,

Measurement of turbulence spectra using scanning pulsed wind lidars

A. Sathe[1,2], J. Mann[1]

A. Sathe, Wind Energy Division, Risø DTU, Frederiksborgvej 399, 4000 Roskilde, Denmark. (amsat@risoe.dtu.dk)

J. Mann, Wind Energy Division, Risø DTU, Frederiksborgvej 399, 4000 Roskilde, Denmark.

[1]Wind Energy Division, Risø DTU,
Frederiksborgvej 399, 4000 Roskilde,
Denmark.

[2]Wind Energy Section, Faculty of
Aerospace Engineering, Delft University of
Technology, The Netherlands.

Abstract. Turbulent velocity spectra, as measured by a scanning pulsed wind lidar (WindCube), are analyzed. The relationship between ordinary velocity spectra and lidar derived spectra is mathematically very complex, and deployment of the three-dimensional spectral velocity tensor is necessary. The resulting scanning lidar spectra depend on beam angles, line-of-sight averaging, sampling rate, and the full three-dimensional structure of the turbulence being measured, in a convoluted way. The model captures the attenuation and redistribution of the spectral energy at high and low wavenumbers very well. The model and measured spectra are in good agreement at two analyzed heights for the u and w components of the velocity field. An interference phenomenon is observed, both in the model and the measurements, when the diameter of the scanning circle divided by the mean wind speed is a multiple of the time between the beam measurements. For the v spectrum, the model and the measurements agree well at both heights, except at very low wavenumbers, $k_1 < 0.005$ m^{-1}. In this region, where the spectral tensor model has not been verified, the model overestimates the spectral energy measured by the lidar. The theoretical understanding of the shape of turbulent velocity spectra measured by scanning pulsed wind lidar is given a firm foundation.

1. Introduction

This study aims to explain how a scanning pulsed wind lidar measures turbulence spectra in combination with the velocity azimuth display (VAD) technique of data processing. In particular, a theoretical model of the turbulence spectra measured by a pulsed wind lidar (WindCube) operating in a VAD mode is developed. The model is verified by comparing measurements from a lidar and a sonic anemometer (sonic).

Turbulence spectra are one of the main inputs in designing any physical structure where random variations in the atmosphere produce random vibrations in the structure, such as suspension bridges, tall buildings, and wind turbines. Wind turbines, in particular, are designed to withstand fatigue and extreme loads during their entire lifetime of approximately 20 years. For the turbulence spectra, the IEC standard [*IEC*, 2005] for wind turbine design prescribes either the Kaimal model [*Kaimal et al.*, 1972] or the more recent Mann model [*Mann*, 1994], which models the three-dimensional turbulent structure under neutral conditions. Besides normal variations of the wind field in the atmosphere, gusts are a major source of extreme loads on many civil engineering structures. Standard gust models can be used to characterize the input for these extreme loads, e.g., the gust models by *Davenport* [1964] and *Kristensen et al.* [1991] are derived from the so-called Rice theory [*Rice*, 1944, 1945], where the gust factor is proportional to the moments of turbulence spectra. Thus, the model of turbulence spectra in this study is also a prerequisite for obtaining a theoretical model of the gust factors measured by lidars.

In micrometeorology, the structure of turbulence consists of three well-defined regions: the energy containing range, inertial sub-range, and dissipative range [*Kaimal and Finni-*

gan, 1994]. Sonics are the current industry standard instrument to measure the first two turbulence regions that influence wind turbines and other structures. However, a meteorological mast (met-mast) is needed in order to support the boom-mounted sonics at several heights. This requirement leads to several disadvantages such as high installation costs for taller masts (particularly offshore), flow distortion due to the mast and booms, need for several instruments to cover all wind directions, and immobility of the mast. A ground-based remote sensing instrument such as a lidar provides an attractive alternative. In recent years, with the introduction of commercial wind lidars, there have been several verification campaigns for comparing the lidar mean wind speed with that of a cup anemometer for wind energy applications [*Courtney et al.*, 2008; *Peña et al.*, 2009]. Although the performance with respect to mean wind speed is currently relatively well understood, in order to use a lidar as a standard measuring instrument in the future, a fair degree of confidence is also required in the turbulence measurements.

Although new to wind energy, for meteorology, lidars have been investigated previously to measure turbulence using different scanning techniques. Turbulence statistics from lidars has actually been a topic of research since the 1960s. One of the early measurements of turbulence spectra was conducted by *Kunkel et al.* [1980], where only the longitudinal component of the wind field was measured in the convective boundary layer. Good comparisons were obtained with the spectral functions of *Kaimal et al.* [1976]. *Hardesty et al.* [1982] measured turbulence spectra in the surface layer by conically scanning lidar in the vertical plane. Large attenuations were observed in the mid-frequency range that were just below the scanning frequency, whereas additional spectral energy was observed at high frequencies because of the re-distribution of energy by sampling points rapidly in a circle.

A preliminary model was also constructed that explains the differences between the point and lidar spectra. *Mayor et al.* [1997] performed measurements of velocity spectra in the convective boundary layer using a staring lidar. Spatial averaging along the line-of-sight was modeled using a spectral transfer function, and an attempt was made to recover the true atmospheric spectra by observing inertial sub-range isotropy. *Frehlich et al.* [1998] investigated wind field statistics and turbulence spectra using lidars at different azimuth and half opening angles. *Drobinski et al.* [2000] measured turbulence spectra using a horizontally staring lidar beam, where spatial averaging in the line-of-sight velocity was modeled using the Kolmogorov spectrum. Good agreements between the modeled and measured spectra were obtained. The staring lidar configuration was also investigated by *Sjöholm et al.* [2009] and *Mann et al.* [2009] for measuring the turbulence spectra of line-of-sight velocities and modeling the corresponding transfer function, where the model agreed well with the measurements. *Lothon et al.* [2009] conducted a comprehensive study of vertical velocity spectra in the convective boundary layer, also using a vertically staring lidar. Different cases were found to sporadically agree with the *Kristensen et al.* [1989] spectral tensor model. However, because of large variability within different cases, a universal model of the vertical velocity spectra in the convective boundary layer could not be developed. *Canadillas et al.* [2010] compared turbulence spectra measured by a WindCube operating in a VAD mode with those measured by a sonic, and observed an unexplained increase in the energy between the energy containing range and the inertial sub-range. A sudden drop in energy was also observed in the inertial sub-range. *Dors et al.* [2011] performed turbulence spectra measurements in the Kelvin-Helmholtz layer by using a fixed lidar beam configuration and a thermosonde. The lidar measurements of the turbulent kinetic energy dissipation range agreed well with those from a thermosonde when the turbulence levels were high. Recently, *Sathe et al.* [2011] investigated the potential of lidars operating in a VAD mode to measure turbulence statistics, where it was concluded that large systematic errors are introduced in the measurement of second-order statistics of the wind field.

In the remaining sections, we concentrate on investigating how turbulence spectra are measured by a pulsed lidar. In section 2, we explain the basics of the WindCube measurements. The modeling of turbulence spectra is described in section 3. Some background of the measurements and the site is presented in section 4. Section 5 compares the model and the measurements at two heights. Finally, we draw conclusions from our study in section 6.

2. Lidar Measurement Basics

Fig. 1 shows the lidar emitting a laser beam at four azimuth angles, viz. North (N), East (E), South (S), and West (W). The line-of-sight velocity (also called radial velocity v_r) is measured by the lidar at respective azimuth angles. The half-opening angle ϕ ($= 90° -$ elevation angle) is maintained constant throughout the scan. In this study, the instrument has $\phi = 27.5°$. Wind lidars work on the principle of backscattering of the emitted radiation from suspended aerosols and subsequent detection of the Doppler shift in the frequency of the received radiation. The Doppler shift in the frequency is related to v_r, as given by

$$\delta f = 2\frac{v_r}{\lambda}, \tag{1}$$

where f and λ are the frequency and wavelength of the emitted radiation, respectively. Mathematically, measurement of the line-of-sight velocity by a scanning lidar is given as the dot product of the unit vector in the direction of the measurement and the velocity field at the center of the measuring volume,

$$v_r(\theta) = \boldsymbol{n}(\theta) \cdot \mathbf{v}(d_f \boldsymbol{n}(\theta)), \tag{2}$$

where θ is the azimuth angle, d_f is the center of the range gate at which the wind speeds are measured, $\boldsymbol{n}(\theta) = (\cos\theta \sin\phi, \sin\theta \sin\phi, \cos\phi)$ is the unit directional vector, and $\mathbf{v} = (u, v, w)$ is the instantaneous velocity field evaluated at the range gate $d_f \boldsymbol{n}(\theta)$. In practice, for a lidar it is impossible to obtain the backscattered radiation precisely from a single point, and there is always backscattered radiation of different intensities from different regions in space along the line-of-sight. Hence, it is necessary to assign appropriate weights to the backscattered intensity such that the weight corresponding to the center of the range gate is the highest. For a pulsed lidar, a triangular weighting function $\varphi(s)$ is commonly assumed [*Lindelöw*, 2007], which is given as

$$\varphi(s) = \begin{cases} \frac{l_p - |s|}{l_p^2} & \text{for } |s| < l_p; \\ 0 & \text{elsewhere,} \end{cases} \tag{3}$$

where l_p is the half length of the ideally rectangular light pulse leaving the lidar, assuming matching time windowing ($= 2l_p/c$, where c is the speed of light). The weighted average radial velocity can thus be written as

$$\tilde{v}_r(\theta) = \int_{-\infty}^{\infty} \varphi(s)\; \boldsymbol{n}(\theta) \cdot \mathbf{v}(\boldsymbol{n}(\theta)(s + d_f))\; ds, \tag{4}$$

where s is the distance along the beam from the center of the range gate.

In this study, we derive expressions of turbulence spectra assuming that the wind comes from the North. The equations become too cumbersome if an arbitrary wind direction is considered. Nevertheless, the same framework can be used in modeling turbulence spectra for any wind direction. Let us denote the unit vectors in the four directions as

$$\boldsymbol{n}_N = \boldsymbol{n}(-\Theta),\ \boldsymbol{n}_S = \boldsymbol{n}(\pi-\Theta),\ \boldsymbol{n}_E = \boldsymbol{n}(\frac{\pi}{2}-\Theta),\ \boldsymbol{n}_W = \boldsymbol{n}(3\frac{\pi}{2}-\Theta), \tag{5}$$

where the subscripts of the unit vectors indicate respective directions and Θ is the wind direction. In this study, we use $\Theta = 0$. If we consider the coordinate system such that the u component is aligned in the mean wind direction, then from simple geometrical considerations for $\Theta = 0$, we get

$$\begin{aligned} u_{wc} &= \frac{\tilde{v}_{rS} - \tilde{v}_{rN}}{2\sin\phi}, \\ v_{wc} &= \frac{\tilde{v}_{rE} - \tilde{v}_{rW}}{2\sin\phi}, \end{aligned} \tag{6}$$

where the subscript wc denotes the measurement by the WindCube, and $\tilde{v}_{rN}$, $\tilde{v}_{rS}$, $\tilde{v}_{rE}$, and $\tilde{v}_{rW}$ are the weighted average radial velocities in the North, South, East, and West directions, respectively. For the w component, we use the formula by the company that produces the WindCube, Leosphere,

$$w_{wc} = \frac{P(\tilde{v}_{rN} + \tilde{v}_{rS}) + Q(\tilde{v}_{rE} + \tilde{v}_{rW})}{2\cos\phi}, \tag{7}$$

where P and Q are the weights associated with the wind direction such that $P + Q = 1$. Leosphere uses $P = \cos^2\Theta$ and $Q = \sin^2\Theta$, and hence, we use the same in our calculations. Thus, for $\Theta = 0$ we get

$$w_{wc} = \frac{\tilde{v}_{rN} + \tilde{v}_{rS}}{2\cos\phi}. \tag{8}$$

Further details of the working principles of the WindCube are given in *Lindelöw* [2007].

3. Modeling the turbulence spectra measured by a pulsed wind lidar

By definition, the one-dimensional spectrum of any component of the wind field is given as [*Wyngaard*, 2010]

$$F_{ij}(k_1) = \frac{1}{2\pi}\int_{-\infty}^{\infty} R_{ij}(x)\exp(-\mathrm{i}k_1 x)\;dx, \\ = \frac{1}{2\pi}\lim_{X\to\infty}\int_{-X}^{X} R_{ij}(x)\exp(-\mathrm{i}k_1 x)\left(\frac{1-|x|}{X}\right)\;dx, \qquad (9)$$

where k_1 is the wavenumber, $F_{ij}(k_1)$ is the one-dimensional spectrum, $R_{ij}(x)$ is the auto-covariance function, x is the separation distance, and X is the length of the record. Since the WindCube cannot make continuous measurements, let us take only discrete values such that $X = N\Delta x$ and $x = n\Delta x$, where n is an integer multiple, N is the total number of samples, and Δx is the distance traveled by the wind when the lidar beam shifts from one azimuth angle to the other. Since it takes about 4 s for the WindCube beam to move from the North to the South, or from the East to the West, assuming Taylor's hypothesis to be valid, we get $\Delta x = \bar{u} \times 4$ m, where $\bar{u}$ is the mean wind speed. If we evaluate the spectra measured by the WindCube at only discrete wave numbers $k_{1_q} = 2\pi q/X$, then we can write

$$F_{ij_{wc}}(q) = \frac{1}{2\pi}\sum_{n=-N}^{N} R_{ij_{wc}}(n)\exp\left(\frac{-\mathrm{i}2\pi nq}{N}\right)\left(1-\frac{|n|}{N}\right)\;\Delta x. \qquad (10)$$

The challenge now is to find an expression for $R_{ij_{wc}}(n)$. As in *Sathe et al.* [2011], we make the following assumptions:

1. The flow is horizontally homogeneous and Taylor's hypothesis is valid.
2. The spatial structure of the turbulent flow is described well by the spectral tensor model of *Mann* [1994].

We first demonstrate the model of $R_{ij_{wc}}(n)$ for the u component and use the same framework to derive the v and w components.

We begin by considering the mathematical form of Taylor's hypothesis such that

$$\mathbf{v}(x,t) = \mathbf{v}(x - \Delta x, 0), \tag{11}$$

where t is the time. For simplicity, let us first neglect the averaging along the line-of-sight. We will introduce this averaging later in the equations. For the turbulence spectra measured by the WindCube, it is necessary to consider the exact spatial and temporal position of the measurements. The wind vector is constructed using the North and South beams such that at any given instant, one current and one previous measurement is used. If we assume that at $t = 0$, we use the current measurement from the North beam and the previous measurement from the South beam, then combining Eqs. (6) and (11) we can write

$$u_{wc}(m\Delta x) = \frac{\tilde{v}_{rS}(\boldsymbol{n}_S d_f - \boldsymbol{e}_1(m-1)\Delta x) - \tilde{v}_{rN}(\boldsymbol{n}_N d_f - \boldsymbol{e}_1 m\Delta x)}{2\sin\phi}, \text{ for even } m, \tag{12}$$

$$u_{wc}(m\Delta x) = \frac{\tilde{v}_{rS}(\boldsymbol{n}_S d_f - \boldsymbol{e}_1 m\Delta x) - \tilde{v}_{rN}(\boldsymbol{n}_N d_f - \boldsymbol{e}_1(m-1)\Delta x)}{2\sin\phi}, \text{ for odd } m, \tag{13}$$

where $\boldsymbol{e}_1 = (1,0,0)$ is the unit vector in the mean wind direction. Combining even and odd m from Eqs. (12) and (13), we can write

$$\begin{aligned} u_{wc}(m\Delta x) = &\Big[\tilde{v}_{rS}\Big(\boldsymbol{n}_S d_f - \boldsymbol{e}_1\big(m - \frac{(1+(-1)^m)}{2}\big)\Delta x\Big) \\ &- \tilde{v}_{rN}\Big(\boldsymbol{n}_N d_f - \boldsymbol{e}_1\big(m - \frac{(1-(-1)^m)}{2}\big)\Delta x\Big)\Big]\Big/\Big(2\sin\phi\Big). \end{aligned} \tag{14}$$

We know that by definition, $R_{ij}(n) = \langle u_i(m\Delta x) u_j\big((m+n)\Delta x\big)\rangle$, where $\langle\rangle$ denotes ensemble averaging. By applying this definition to Eq. (14), we get auto and cross covariances for the North and South beams. Introducing the averaging along the beam (using Eq. 4) for only the south beam, we get

$$\Big\langle \tilde{v}_{rS}\Big(\boldsymbol{n}_S d_f - \boldsymbol{e}_1\big(m - \frac{(1+(-1)^m)}{2}\big)\Delta x\Big)\tilde{v}_{rS}\Big(\boldsymbol{n}_S d_f - \boldsymbol{e}_1\big((m+n) - \frac{(1+(-1)^{m+n})}{2}\big)\Delta x\Big)\Big\rangle$$
$$= \int_{-\infty}^{\infty}\int_{-\infty}^{\infty} n_{iS} n_{jS}\ \varphi(s_1)\varphi(s_2)$$
$$\Big\langle \mathrm{v}_i\Big(\boldsymbol{n}_S d_f - \boldsymbol{e}_1\big(m - \frac{(1+(-1)^m)}{2}\big)\Delta x + \boldsymbol{n}_S s_1\Big)$$
$$\mathrm{v}_j\Big(\boldsymbol{n}_S d_f - \boldsymbol{e}_1\big((m+n) - \frac{(1+(-1)^{m+n})}{2}\big)\Delta x + \boldsymbol{n}_S s_2\Big)\Big\rangle\ ds_1 ds_2 \tag{15}$$

If we denote $\boldsymbol{r} = \Big(\boldsymbol{n}_S d_f - \boldsymbol{e}_1\big(m - (1+(-1)^m)/2\big)\Delta x\Big) - \Big(\boldsymbol{n}_S d_f - \boldsymbol{e}_1\big((m+n) - (1+(-1)^{m+n})/2\big)\Delta x\Big)$ as the separation distance between the S-S beam combination, then we can write

$$R_{\tilde{v}_{rS}}(n) = \int_{-\infty}^{\infty}\int_{-\infty}^{\infty} n_{iS} n_{jS}\ \varphi(s_1)\varphi(s_2) R_{ij}(\boldsymbol{r} + \boldsymbol{n}_S(s_1 - s_2))\ ds_1 ds_2, \tag{16}$$

where $R_{\tilde{v}_{rS}}(n)$ is the autocovariance of the radial velocity for the South beam. $R_{ij}(\boldsymbol{r})$ is related to the three dimensional spectral velocity tensor $\Phi_{ij}(\boldsymbol{k})$ by the inverse Fourier transform [*Wyngaard*, 2010], i.e.,

$$R_{ij}(\boldsymbol{r} + \boldsymbol{n}_S(s_1 - s_2)) = \int \Phi_{ij}(\boldsymbol{k}) \exp(\mathrm{i}\boldsymbol{k}\cdot(\boldsymbol{r} + \boldsymbol{n}_S(s_1 - s_2)))\ d\boldsymbol{k}, \tag{17}$$

where $\int d\boldsymbol{k} \equiv \int_{-\infty}^{\infty}\int_{-\infty}^{\infty}\int_{-\infty}^{\infty} dk_1 dk_2 dk_3$ and $\boldsymbol{k} = (k_1, k_2, k_3)$ denotes the wave vector. Substituting Eq. (17) into (16) and rearranging the terms, we get

$$R_{\tilde{v}_{rS}}(\boldsymbol{r}) = \int \Phi_{ij}(\boldsymbol{k})\ n_{iS} n_{jS}\ \exp(\mathrm{i}\boldsymbol{k}\cdot\boldsymbol{r})\ \hat{\varphi}(\boldsymbol{k}\cdot\boldsymbol{n}_S)\hat{\varphi}^*(\boldsymbol{k}\cdot\boldsymbol{n}_S)\ d\boldsymbol{k} \tag{18}$$

where ˆ denotes Fourier transform and * complex conjugation. Reducing the expression of $\boldsymbol{r}$, we get

$$\boldsymbol{r} = \boldsymbol{e}_1\Big((-1)^m \frac{\Delta x}{2}(1 - (-1)^n) + n\Delta x\Big). \tag{19}$$

Similarly, if we assume that at $t = 0$ we use the current measurement from the South beam and the previous measurement from the North beam, then we get

$$\begin{aligned} u_{wc}(m\Delta x) =& \Big[\tilde{v}_{rS}\Big(\boldsymbol{n}_S d_f - \boldsymbol{e}_1\big(m - \frac{(1-(-1)^m)}{2}\big)\Delta x\Big) \\ & - \tilde{v}_{rN}\Big(\boldsymbol{n}_N d_f - \boldsymbol{e}_1\big(m - \frac{(1+(-1)^m)}{2}\big)\Delta x\Big)\Big]\Big/\Big(2\sin\phi\Big), \end{aligned} \tag{20}$$

and the separation distance for the S-S beam combination is given as $\boldsymbol{r} = -(-1)^m\Delta x/2(1-(-1)^n) + n\Delta x$. In order to make the time series statistically stationary, we consider that there is an equal probability that the beam at $t = 0$ points either in the North or South direction. This eliminates the dependence of the autocovariance function on m. We perform similar analysis on the auto and cross covariances for other beams. In total, we then get eight separation distances; two for the S-S, two for S-N, two for N-S, and two for N-N beam combinations. If we denote $\boldsymbol{r}_{u_l}$ (the subscript l denotes the respective beam combination) as the separation distance for different beam combinations, then we can write all the separation distances in compact form as

$$\boldsymbol{r}_{u_l} = \begin{cases} \boldsymbol{e}_1\Big((-1)^l\frac{\Delta x}{2}(1-(-1)^n) + n\Delta x\Big) & \text{for } l = 1,2,7,8; \\ \boldsymbol{n}_S d_f - \boldsymbol{n}_N d_f + \boldsymbol{e}_1\Big((-1)^l\frac{\Delta x}{2}(1+(-1)^n) + n\Delta x\Big) & \text{for } l = 3,4; \\ \boldsymbol{n}_N d_f - \boldsymbol{n}_S d_f + \boldsymbol{e}_1\Big((-1)^l\frac{\Delta x}{2}(1+(-1)^n) + n\Delta x\Big) & \text{for } l = 5,6. \end{cases} \tag{21}$$

Following a similar procedure for the v component, we get the following separation distances:

$$\boldsymbol{r}_{v_l} = \begin{cases} \boldsymbol{e}_1\Big((-1)^l\frac{\Delta x}{2}(1-(-1)^n) + n\Delta x\Big) & \text{for } l = 1,2,7,8; \\ \boldsymbol{n}_E d_f - \boldsymbol{n}_W d_f + \boldsymbol{e}_1\Big((-1)^l\frac{\Delta x}{2}(1+(-1)^n) + n\Delta x\Big) & \text{for } l = 3,4; \\ \boldsymbol{n}_W d_f - \boldsymbol{n}_E d_f + \boldsymbol{e}_1\Big((-1)^l\frac{\Delta x}{2}(1+(-1)^n) + n\Delta x\Big) & \text{for } l = 5,6. \end{cases} \tag{22}$$

The separation distances for the w component are the same as those for the u component, because only the North and South beams are used to obtain w_{wc} (Eq. 8). Combining Eqs. (12)–(22) and using the symmetry properties of $\Phi_{ij}(\boldsymbol{k})$, we get the expressions for the autocovariance of the u and v components as

$$\begin{aligned} R_{u_{wc}}(n) = \frac{1}{8\sin^2\phi} \int \Phi_{ij}(\boldsymbol{k}) \Big[& n_{iS} n_{jS} \hat{\varphi}(\boldsymbol{k}\cdot\boldsymbol{n}_S)\hat{\varphi}^*(\boldsymbol{k}\cdot\boldsymbol{n}_S) \sum_{l=1}^{2} \exp(\mathrm{i}\boldsymbol{k}\cdot\boldsymbol{r}_{u_l}) \\ & - n_{iS} n_{jN} \hat{\varphi}(\boldsymbol{k}\cdot\boldsymbol{n}_S)\hat{\varphi}^*(\boldsymbol{k}\cdot\boldsymbol{n}_N) \sum_{l=3}^{6} \exp(\mathrm{i}\boldsymbol{k}\cdot\boldsymbol{r}_{u_l}) \\ & + n_{iN} n_{jN} \hat{\varphi}(\boldsymbol{k}\cdot\boldsymbol{n}_N)\hat{\varphi}^*(\boldsymbol{k}\cdot\boldsymbol{n}_N) \sum_{l=7}^{8} \exp(\mathrm{i}\boldsymbol{k}\cdot\boldsymbol{r}_{u_l}) \Big] d\boldsymbol{k}, \end{aligned} \tag{23}$$

$$\begin{aligned} R_{v_{wc}}(n) = \frac{1}{8\sin^2\phi} \int \Phi_{ij}(\boldsymbol{k}) \Big[& n_{iE} n_{jE} \hat{\varphi}(\boldsymbol{k}\cdot\boldsymbol{n}_E)\hat{\varphi}^*(\boldsymbol{k}\cdot\boldsymbol{n}_E) \sum_{l=1}^{2} \exp(\mathrm{i}\boldsymbol{k}\cdot\boldsymbol{r}_{v_l}) \\ & - n_{iE} n_{jW} \hat{\varphi}(\boldsymbol{k}\cdot\boldsymbol{n}_E)\hat{\varphi}^*(\boldsymbol{k}\cdot\boldsymbol{n}_W) \sum_{l=3}^{6} \exp(\mathrm{i}\boldsymbol{k}\cdot\boldsymbol{r}_{v_l}) \\ & + n_{iW} n_{jW} \hat{\varphi}(\boldsymbol{k}\cdot\boldsymbol{n}_W)\hat{\varphi}^*(\boldsymbol{k}\cdot\boldsymbol{n}_W) \sum_{l=7}^{8} \exp(\mathrm{i}\boldsymbol{k}\cdot\boldsymbol{r}_{v_l}) \Big] d\boldsymbol{k}. \end{aligned} \tag{24}$$

The expression for the w component is similar to that for the u component, except that the second term in the square brackets of Eq. (23) is added instead of subtracted, and $\sin^2\phi$ is replaced by $\cos^2\phi$ in the denominator. Substituting Eqs. (23) and (24) into Eq. (10), we can finally theoretically calculate the turbulence spectra measured by the WindCube for the u, v, and w components of the velocity field.

In order to see the extent of attenuation and redistribution of the spectral energy, we compare these models with the true theoretical spectra measured by sonics and those measured by the WindCube. The true theoretical spectrum of any component of the wind field is also given as (apart from Eq. 9) [*Wyngaard*, 2010],

$$F_{ij}(k_1) = \int_{-\infty}^{\infty}\int_{-\infty}^{\infty} \Phi_{ij}(\boldsymbol{k})\ dk_2 dk_3. \tag{25}$$

We consider the sonic measurements to essentially represent the true theoretical spectra.

4. Description of the measurements

The measurements were performed at the Danish National Test Center for Large Wind Turbines at Høvsøre, Denmark. A reference met-mast, which is 116.5 m tall and intensively equipped with cup and sonic anemometers, is located at the coordinates 56°26'26" N, 08°09'03" E. The site is about 2 km from the West coast of Denmark. The eastern sector is generally characterized by a flat, homogeneous terrain, and to the South is a lagoon. To the North, there is a row of five wind turbines. The sonics are placed on the North booms of the met-mast, resulting in unusable data when the wind is from the south because of the wake of the mast, and from the North because of the wakes of the wind turbines.

We use the sonic measurements at 60 and 100 m in combination with the WindCube to compare with the modeled turbulence spectra. The WindCube is located about 5 m North-West of the met-mast, and the data were collected between January and April 2009. In order to avoid interference with the met-mast, the WindCube is turned in a horizontal plane such that the nominal North beam is 45° (i.e., in a North-East direction) with respect to true North. The frequency of measurement for the sonics is 20 Hz, whereas the WindCube takes approximately 2 s to shift from one azimuth angle to the other. We use the measurements from a narrow directional sector of 130°–140° only in order to align the mean wind direction with the nominal E-W beam of the WindCube. Thus, the u and w component measurements are deduced from the nominal E-W beams and the v component measurements are deduced from the nominal N-S beams. In order to avoid further confusion with Eqs. (6) and (8), the nominal E-W beam in the measurement is essentially the N-S beam in the theory, and vice-versa.

The other criteria for the selection of the data are neutral atmospheric stability and a mean wind speed of 9 m/s. Using Taylor's hypothesis, we then have the sampling distance in the mean wind direction $\Delta x = 9 \times 4$ m. We selected the data with a mean wind speed in the interval 8-10 m/s, which resulted in 79 and 58 10-min time series of the sonics and the WindCube at 60 and 100 m, respectively. Atmospheric stability is characterized using the standard surface-layer length scale L_{MO}, commonly known as the Monin-Obukhov length. Following *Gryning et al.* [2007], the conditions are considered neutral when $|L_{MO}| > 500$. L_{MO} is estimated using the eddy covariance method [*Kaimal and Finnigan*, 1994] from the sonic measurements at 20 m. Mathematically, L_{MO} is given as

$$L_{MO} = -\frac{{u_*}^3 T}{\kappa g \overline{w'\theta'_v}}, \tag{26}$$

where u_* is the friction velocity, $\kappa = 0.4$ is the von Kármán constant, g is the acceleration due to gravity, T is the absolute temperature, θ_v is the virtual potential temperature, and $\overline{w'\theta'_v}$ (covariance of w and θ_v) is the virtual kinematic heat flux. u_* is estimated as

$$u_* = \sqrt[4]{\overline{u'w'}^2 + \overline{v'w'}^2}, \tag{27}$$

where $\overline{u'w'}$ and $\overline{v'w'}$ are the vertical fluxes of the horizontal momentum.

The precision of the sonics is estimated to be about ±1.5%. Comparing with cup anemometers, the mean error of the WindCube in typical flat coastal conditions is within ±0.05 m/s, with a standard deviation in mixed shear conditions of about 0.15 m/s. A detailed list of different error sources is given by *Lindelöw-Marsden* [2009]. More details of the site and instrumentation can be found in *Sathe et al.* [2011].

5. Comparison of the model with the measurements

In order to calculate $\Phi_{ij}(\boldsymbol{k})$ in Eqs. (23)–(25), we use the model by *Mann* [1994]. It requires three model parameters, $\alpha\epsilon^{2/3}$, which is a product of the spectral Kolmogorov constant α [*Wyngaard*, 2010] and the rate of viscous dissipation of specific turbulent kinetic energy to the two-thirds power $\epsilon^{2/3}$, a length scale L and an anisotropy parameter Γ. In this study, these model parameters are obtained at 60 and 100 m by a χ^2-fit of the sonic measurements under neutral conditions (Eq. 4.1 from *Mann* [1994]) within the chosen directional sector of 130°–140°. As a result, the *Mann* [1994] model and the measurements agree very well for the sonics. The fitted model parameters are given in table 1. The *Mann* [1994] model is such that analytical expressions of $R_{ij}(\boldsymbol{r})$ and $F_{ij}(k_1)$ from $\Phi_{ij}(\boldsymbol{k})$ are not possible by integrating over the $\boldsymbol{k}$ domain. Hence, we use numerical integration based on adaptive algorithm [*Genz and Malik*, 1980] in order to calculate the integrals in Eqs. (23)–(25).

5.1. u spectrum

Fig. 2 shows the comparison of the modeled and measured u spectrum at 60 and 100 m. The measurements indicate that the spectrum measured by the WindCube deviates significantly from the standard surface-layer spectrum as the turbulence scales decrease approximately from $k_1 > 0.005$ m^{-1}. Approximately in the inertial sub-range, where the sonic spectra scales with $k_1^{-5/3}$, there is an almost complete attenuation of the turbulence signal, and hence a rapid decrease in the spectral energy. This observation has a striking resemblance with that of *Canadillas et al.* [2010], where an independent measurement under neutral conditions in the German North Sea showed an increase in the spectral energy above $k_1 > 0.005$ m^{-1} and subsequent rapid attenuation. One of the reasons for this redistribution of the spectral energy is the contribution of the auto and cross covariances of different components of the velocity field, as seen in Eq. (23). At very low wavenumbers (< 0.005 m^{-1}), the spectral energy measured by the WindCube is approximately the same as that measured by the sonics. This is because very large turbulence eddies are associated with very low wavenumbers that cause the volume measurement from the lidar to behave essentially like a point measurement.

At both heights, our model agrees very well with the measurements at almost all wavenumbers. The point-like behavior of the WindCube at very low wavenumbers, and redistribution of the spectral energy beyond $k_1 > 0.005$ m^{-1}, is captured by the model very well. However, there are stark differences in the distribution of the spectral energy at 60 and 100 m. This is because of the beam interference phenomenon that occurs for certain separation distances at 100 m. This is explained as follows.

In our model, we have assumed validity of Taylor's hypothesis, which states that turbulence is advected by the mean wind field, i.e., the local velocity of the turbulent eddies is so small that they essentially move with only the mean velocity. In other words, turbulence can be considered to be frozen. For the u spectrum, we use only the N-S beams that are aligned in the mean wind direction. At 100 m, the mean wind speed is such that the North and South beams will investigate the same air (but different components) after approximately $3\Delta x$. Looking more closely at Eq. (21), at $3\Delta x$ we get $r_{u_3} \to 0$ and $r_{u_4} \to 0$. This implies that in Eq. (23), $\exp(\mathrm{i}\boldsymbol{k} \cdot r_{u_3}) \to 1$ and $\exp(\mathrm{i}\boldsymbol{k} \cdot r_{u_4}) \to 1$. This will cause an overall decrease in $R_{u_{wc}}(n)$ at $n = 3$. From our calculations, we also find anomalous behavior of $R_{u_{wc}}(n)$ at $n = 2$ and $n = 4$. Revisiting Eq. (21), we find that at $n = 2$, $r_{u_3} \to 0$ and at $n = 4$, $r_{u_4} \to 0$. This implies that it will cause some reduction in

$R_{u_{wc}}(n)$, but not as much as when $n = 3$. In order to explain this behavior, we illustrate the interference phenomenon of the beams in Fig. 3.

Since we assume Taylor's hypothesis, we can either fix the N-S beams and measure the flow field as it moves past the beams, or freeze the flow field and move the N-S beams instead. For simplicity, let us freeze the flow field and represent 1–8 as the positions at which the North and the South beams perform measurements. The difference between each position is then equal to the separation distance Δx. Let 1, 3, 5, and 7 denote the measurements of the North beam and 2, 4, 6, and 8 denote those of the South beam. For now, let us consider only the intersection of beams 2 and 5 at point A, which is the point where the North and South beams will see the same air. This occurs at a separation distance of $3\Delta x$ corresponding to a height of 104 m. As a result, we will get unusual covariances whenever there is intersection of beams 2 and 5 in combination with other beam measurements. Since the WindCube uses one current and one previous measurement to deduce wind field components, we use the measurement from beam 2 when it is in combination with beam 1 or 3. Similarly, we use beam 5 when it is in combination with beam 4 or 6. These combinations can be written as

$$\begin{bmatrix} (\mathbf{2},1) & (\mathbf{3},2) \\ (\mathbf{5},4) & (\mathbf{6},5) \end{bmatrix} \tag{28}$$

The bold numbers in Eq. (28) indicate the current measurement for the respective beams, i.e., the set $(\mathbf{2},1)$ indicates that the current measurement from beam 2 is used in combination with the previous measurement from beam 1 to deduce the u component, and so on for other sets. In this case, we will obtain unusual covariances at these separation distances in the model, which are equal to the difference between beam numbers in bold (Eq. 28) that correspond to the intersection of beams 2 and 5. This happens at $\mathbf{5}-\mathbf{3}$, $\mathbf{5}-\mathbf{2}$, and $\mathbf{6}-\mathbf{2}$, corresponding to separation distances of $2\Delta x$, $3\Delta x$, and $4\Delta x$, respectively. We do not get unusual covariances at $\mathbf{3}-\mathbf{2}$ because the sets $(\mathbf{2},1)$ and $(\mathbf{3},2)$ do not contain beam 5, and similarly at $\mathbf{6}-\mathbf{5}$, since the sets $(\mathbf{5},4)$ and $(\mathbf{6},5)$ do not contain beam 2. Thus, in general, we will always obtain unusual covariances at the heights at which the distance between the North and the South beams corresponds to separation distances of $(n-1)\Delta x$, $n\Delta x$, and $(n+1)\Delta x$ (where n is odd, since for even n the North and South beams never intersect). Thus, if we now consider intersection points B (≈ 35 m) and C (≈ 173 m) in Fig. 3, then the separation distances are Δx and $5\Delta x$, respectively. Thus, we should expect unusual covariances at 0, Δx, and $2\Delta x$ at 35 m, whereas at 173 m, we expect the same at $4\Delta x$, $5\Delta x$, and $6\Delta x$.

In order to verify the above explanation, $R_{u_{wc}}(n)/\sigma_u^2$ (where σ_u^2 is the true variance of the u component) is calculated at two separation distances (100 and 173 m), as shown in Fig. 4. We do not calculate $R_{u_{wc}}(n)/\sigma_u^2$ at 35 m because the WindCube reliably measures from approximately 40 m (owing to a large measuring volume of about 30 m). σ_u^2 is calculated by integrating Eq. (25) over the k_1 domain at respective heights. We can now clearly see unusual covariances at $(n-1)\Delta x$, $n\Delta x$, and $(n+1)\Delta x$ at both heights, where $n=3$ at 100 m and $n=5$ at 173 m. Fig. 2 indicates that the model captures this beam interference phenomenon, which is also present in the measurements at 100 m, very well. Thus, it could also be implied that in nature, Taylor's hypothesis is valid to some extent.

5.2. *v* spectrum

Fig. 5 shows the comparison of the modeled and measured v spectrum at 60 and 100m. As observed for the u component, the v spectrum measured by the lidar deviates significantly from that of the sonic spectrum. However, at very low wavenumbers, there is an offset in the spectral energy between the lidar and the sonic. The behavior in the inertial sub-range is the same as that for the u component, where a rapid attenuation in the spectral energy is observed. Our model agrees very well with the measurements at 60 and 100 m, except at very low wavenumbers (< 0.005 m^{-1}), where the model over estimates the spectral energy. One striking feature of this comparison is that as opposed to the u component, we do not see any beam interference phenomenon at 100 m because of Taylor's hypothesis. This is because only the E-W beams are used to deduce the v components, which are perpendicular to the mean wind field. Thus, even though we assume Taylor's hypothesis, the beams never interfere with each other at any separation distance. Thus, this result indirectly verifies the beam interference phenomenon explanation for the u component at 100 m. We give the following explanation for the over estimation of the spectral energy at very low wavenumbers.

From Eq. (24), it is understood that the v spectrum measured by the WindCube contains contributions from the v and w components of the spectral tensor, i.e., $\Phi_{22}(\boldsymbol{k})$ and $\Phi_{33}(\boldsymbol{k})$, weighted by the corresponding weighting functions $|\varphi(\boldsymbol{k} \cdot \boldsymbol{n}_E)|^2$ and $|\varphi(\boldsymbol{k} \cdot \boldsymbol{n}_W)|^2$. Due to the assumption of uniform shear and no effect of the Coriolis force by *Mann* [1994], the symmetry group of the spectral tensor model is such that the co-spectral energy between v and w is zero, i.e., $F_{23}(k_1) = 0$. We observed, using sonic anemometer measurements, that $F_{23}(k_1)$ is not exactly zero, but has some negative spectral energy at all wavenumbers. We also observed that $F_{23}(k_1) < F_{13}(k_1)$. On closely analyzing Eq. (24), we note that, in nature, if $F_{23}(k_1)$ contributes to the covariance measured by the lidar, it will result in overall reduction of $R_{v_{wc}}$. Thus, the symmetry group of *Mann* [1994] may not be entirely valid. We also find that the contribution of the second term in Eq. (24) is negligible, and only the first and the third terms add to the spectral energy. Let us now consider a case such that at 60 m, the beam is staring perpendicularly to the mean wind field in a horizontal plane. It will thus measure only the v component of the velocity field. In this case, the v spectrum measured by the WindCube is given as

$$F_{v_{wc*}}(k_1) = \int_{-\infty}^{\infty} \Big(\int_{-\infty}^{\infty} \Phi_{22}(\boldsymbol{k}) \; dk_3 \Big) |\hat{\varphi}(k_2)|^2 \; dk_2, \tag{29}$$

where $*$ denotes spectra for a staring beam lidar. In Eq. (29), we first integrate over the k_3 domain, and the resulting two dimensional spectrum $E_v(k_1, k_2)$ is weighted by the filter function $|\hat{\varphi}(k_2)|^2$. The behavior of the weighting function is such that $|\hat{\varphi}(k_2)|^2 \to 1$ as $k_2 \to 0$. Thus, if the amount of two dimensional spectral energy increases sharply as $(k_1, k_2) \to 0$, then the contribution of this spectral energy in the one-dimensional spectrum will be significant. In order to verify this assumption, we calculate $E_v(k_1, k_2)$ at three values of k_1, i.e., $k_1 = (10^{-1}, 10^{-2}, 10^{-3})$ m^{-1}, as shown in Fig. 6. We also plot the variation of $|\hat{\varphi}(k_2)|^2$, so that filtering of the spectral energy for the respective wavenumbers is clearly evident. From the figure, it is observed that $k_1 \to 0$, $E_v(k_1, k_2)$ increases by several orders of magnitude with decreasing $|k_2|$ until a certain value of $|k_2|$, after which it decreases with $k_2 \to 0$. Since *Mann* [1994] does not assume isotropy in the horizontal plane, $E_v(k_1, k_2) \nrightarrow 0$ as $(k_1, k_2) \to 0$ [*Wyngaard*, 2010]. In our study, the WindCube is not horizontal, but at $\phi = 27.5°$ with the vertical. Hence, for the v component, the filter function along the line-of-sight acts over k_2 and k_3 domains. Its influence on averaging of the two and three dimensional spectral energy will be much more complicated than that for a horizontally pointing lidar. Nevertheless, we can argue similar reasons for the conically scanning case.

From the above explanation, we can consider four reasons for the over estimation of $F_{v_{wc}}(k_1)$ in the model as $k_1 \rightarrow 0$.

1. $E_v(k_1, k_2)$ could be more spread out such that the total energy over the k_2 domain would still be the same as that predicted by the *Mann* [1994] model.
2. The peak in $E_v(k_1, k_2)$ could be shifted to larger values of $|k_2|$.
3. Despite anisotropic conditions, $E_v(k_1, k_2)$ could approach zero as $(k_1, k_2) \rightarrow 0$.
4. There could be some contribution by $F_{23}(k_1)$.

As a consequence, the *Mann* [1994] model would still predict $F_v(k_1)$ considerably accurate. However, when $E_v(k_1, k_2)$ is weighted by $|\hat{\varphi}(k_2)|^2$, the total energy calculated using the *Mann* [1994] model and that obtained in nature would be different. Thus, it will cause overestimation of $F_{v_{wc}}(k_1)$ as $k_1 \rightarrow 0$, despite observing a good agreement between the theoretical and measured $F_v(k_1)$ (Fig. 5). Unfortunately, it is very difficult to measure the two- and three-dimensional spectra, and hence, we cannot verify our explanation.

5.3. *w* spectrum

Fig. 7 shows the comparison of the modeled and measured w spectrum at 60 and 100 m. Since in the calculation of the w spectrum, we use only the North and South beams, we will obtain similar beam interference at 100 m, because of the assumption of Taylor's hypothesis, as that observed for the u spectrum. The measured WindCube spectrum agrees quite well with the model at both heights, especially at high wavenumbers. As observed for the u component, at 100 m we note the effect of unusual covariances on the spectral energies. At very low wavenumbers, there is a slight offset between the model and measurements. This offset could be because of the slight deviation in the modeled and measured sonic spectrum. The model also shows that at very low wavenumbers, because of very large turbulence eddies, the volume measurement from the lidar behaves similar to a point measurement.

6. Conclusion

The main objective of this paper is to understand how a pulsed wind lidar measures turbulence spectra. For this purpose, we modeled the u, v, and w spectra as measured by the WindCube only for a case where the mean wind direction is aligned with the measurement beams. For an arbitrary wind direction, a similar framework can be used, but it is much more complicated. In general, the model agrees very well with the measurements for all three components at both heights, except at very low wavenumbers for the v component.

For the u and w components at very low wavenumbers (< 0.005 m^{-1}), the volume measurement of the lidar behaves similar to a point measurement because of very large turbulence eddies. However, redistribution of the spectral energy is noted for all components above 0.005 m^{-1} , which is captured by the model very well. One of the important findings of this study is that for the u and w components the beam interference phenomenon will be observed at the heights in the mean wind direction at which the distance between the beams on the azimuth circle is equal to some odd multiple of the separation distance $(n-1)\Delta x$, $n\Delta x$ and $(n+1)\Delta x$; this is because of the assumption of Taylor's hypothesis. We observe the influence of this beam interference phenomenon at 100 m for the u and w components at approximately $2\Delta x$, $3\Delta x$, and $4\Delta x$.

For the v component, we observe an offset in the spectral energy at very low frequencies compared with those measured by the sonics. One of the reasons for this offset is the large contribution of $\Phi_{22}(\boldsymbol{k})$ as $\boldsymbol{k} \to 0$. Such an offset is also observed in our model, but to a greater degree. We have speculated an explanation based on the difference in the shape of the modeled and the true two-dimensional spectrum $E_v(k_1, k_2)$. Due to lack of measurements of $E_v(k_1, k_2)$, we cannot verify our explanation. Furthermore, there is a small contribution of $F_{23}(k_1)$ in nature, which is not taken into account in the spectral tensor model.

We theoretically explained the interaction of the spectral tensors that cause redistribution of the spectral energy, and thus measurement of turbulence spectra using pulsed wind lidars is clarified. This study is particularly relevant for further understanding of how a pulsed wind lidar measures turbulent gusts. Given the complications displayed in this study, it might be advantageous to abandon the VAD technique for spectral analysis of lidar data, and instead analyze time series of individual beams. This approach is currently being pursued at Risø DTU, Denmark.

Acknowledgments. This study is part of a PhD project at Delft University of Technology. The experimental results are all based on data collected at the Høvsøre Test Station under the auspices of Anders Ramsing Vestergaard and Bjarne Sønderskov. This paper has been prepared using resources provided by the European Commission's FP7 SafeWind Project, Grant Agreement no. 213740, and by the Center for Computational Wind Turbine Aerodynamics and Atmospheric Turbulence funded by the Danish Council for Strategic Research grant no. 09-067216. Finally, the authors would like to thank Dr. Mike Courtney for useful comments and also checking the manuscript for English language errors.

References

Canadillas, B., A. Bégué, and T. Neumann (2010), Comparison of turbulence spectra derived from LiDAR and sonic measurements at the offshore platform FINO1, in *DEWEK 2010,* 10th *German Wind Energy Conference.*

Courtney, M., R. Wagner, and P. Lindelow (2008), Testing and comparison of lidars for profile and turbulence measurements in wind energy, in 14th *International Symposium for the Advancement of Boudary Layer Remote Sensing*, *IOP Conference Series Earth and Environmental Science*, vol. 1, edited by J. Mann et al., p. 012021, IOP Publishing LTD., doi:10.1088/1755-1315/1/1/012021.

Davenport, A. G. (1964), Note on the distribution of the largest value of a random function with application to gust loading, *ICE Proceedings*, *28*(2), 187–196, doi:10.1680/iicep.1964.10112.

Dors, I., J. P. McHugh, G. Y. Jumper, and J. Roadcap (2011), Velocity spectra and turbulence using direct detection lidar and comparison with thermosonde measurements, *Journal of Geophysical Research*, *116*, D01,102, 1–12, doi:10.1029/2010JD014606.

Drobinski, P., A. M. Dabas, and P. H. Flamant (2000), Remote measurement of turbulent wind spectra by heterodyne Doppler lidar technique, *Journal of Applied Meteorology*, *39*, 2434–2451, doi:10.1175/1520-0450(2000)039<2434:RMOTWS>2.0.CO;2.

Frehlich, R., S. M. Hannon, and S. W. Henderson (1998), Coherent doppler lidar measurements on wind field statistics, *Boundary-Layer Meteorology*, *86*(2), 233–256, doi:10.1023/A:1000676021745.

Genz, A. C., and A. A. Malik (1980), Remarks on algorithm 006: An Adaptive Algorithm for Numerical Integration over an N-dimensional Rectangular Region, *Journal of Com-*

putational and Applied Mathematics, *6*(4), 295–302, doi:10.1016/0771-050X(80)90039-X.

Gryning, S.-E., E. Batchvarova, B. Brümmer, H. Jørgensen, and S. Larsen (2007), On the extension of the wind profile over homogeneous terrain beyond the surface layer, *Boundary-Layer Meteorology*, *124*(2), 251–268, doi:10.1007/s10546-007-9166-9.

Hardesty, R. M., J. A. Korrell, and F. F. Hall (1982), Lidar measurement of wind velocity turbulence spectra encountered by a rotating turbine blade, *Technical Report DOE/RL/10236-81/1*, National Oceanic and Atmospheric Administration, Boulder, CO (USA).

IEC (2005), IEC 61400-1. Wind turbines – Part 1: Design Requirements.

Kaimal, J. C., and J. J. Finnigan (1994), *Atmospheric Boundary Layer Flows*, chap. Acquisition and processing of atmospheric boundary layer data, pp. 255–257, Oxford University Press, New York.

Kaimal, J. C., J. C. Wyngaard, Y. Izumi, and O. R. Coté (1972), Spectral characteristics of surface-layer turbulence, *Quarterly Journal of the Royal Meteorological Society*, *98*(417), 563–589, doi:10.1002/qj.49709841707.

Kaimal, J. C., J. C. Wyngaard, D. A. Haugen, O. R. Cote, Y. Izumi, S. J. Caughey, and C. J. Readings (1976), Turbulence structure in the convective boundary layer, *Journal of Atmospheric Sciences*, *33*(11), 2152–2169, doi:10.1175/1520-0469(1976)033<2152:TSITCB>2.0.CO;2.

Kristensen, L., D. H. Lenschow, P. Kirkegaard, and M. Courtney (1989), The spectral velocity tensor for homogeneous boundary-layer turbulence, *Boundary-Layer Meteorology*, *47*(1–4), 149–193, doi:10.1007/BF00122327.

Kristensen, L., M. Casanova, M. S. Courtney, and I. Troen (1991), In search of a gust definition, *Boundary-Layer Meteorology*, *55*(1–2), 91–107, doi:10.1007/BF00119328.

Kunkel, K. E., E. W. Eloranta, and J. A. Weinman (1980), Remote determination of winds, turbulence spectra and energy dissipation rates in the boundary layer from lidar measurements, *Journal of Atmospheric Sciences*, *37*(5), 978–985, doi:10.1175/1520-0469(1980)037<0978:RDOWTS>2.0.CO;2.

Lindelöw, P. (2007), Fibre based coherent lidars for remote wind sensing, PhD thesis, Technical University Denmark.

Lindelöw-Marsden, P. (2009), UpWind D1. Uncertainties in wind assessment with LIDAR, *Tech. Rep. Risø-R-1681(EN)*, Risø DTU.

Lothon, M., D. H. Lenschow, and S. D. Mayor (2009), Doppler lidar measurements of vertical velocity spectra in the convective planetary boundary layer, *Boundary-Layer Meteorology*, *132*(2), 205–226, doi:10.1007/s10546-009-9398-y.

Mann, J. (1994), The spatial structure of neutral atmospheric surface-layer turbulence, *Journal of Fluid Mechanics*, *273*, 141–168, doi:10.1017/S0022112094001886.

Mann, J., J. Cariou, M. Courtney, R. Parmentier, T. Mikkelsen, R. Wagner, P. Lindelow, M. Sjöholm, and K. Enevoldsen (2009), Comparison of 3D turbulence measurements using three staring wind lidars and a sonic anemometer, *Meteorologische Zeitschrift*, *18*(2, Sp. Iss. SI), 135–140, doi:10.1127/0941-2948/2009/0370.

Mayor, S. D., D. H. Lenschow, R. L. Schwiesow, J. Mann, C. L. Frush, and M. K. Simon (1997), Validation of NCAR 10.6-μm CO$_2$ Doppler lidar radial velocity measurements and comparison with a 915-MHz profiler, *Journal of Atmospheric and Oceanic Technology*, *14*(5), 1110–1126, doi:10.1175/1520-0426(1997)014<1110:VONMCD>2.0.CO;2.

Peña, A., C. B. Hasager, S.-E. Gryning, M. Courtney, I. Antoniou, and T. Mikkelsen (2009), Offshore wind profiling using light detection and ranging measurements, *Wind Energy*, *12*(2), 105–124, doi:10.1002/we.283.

Rice, S. O. (1944), Mathematical analysis of random noise, *Bell System Tech. J.*, *23*(3), 282–332.

Rice, S. O. (1945), Mathematical analysis of random noise, *Bell System Tech. J.*, *24*(1), 46–156.

Sathe, A., J. Mann, J. Gottschall, and M. S. Courtney (2011), Can wind lidars measure turbulence?, *Journal of Atmospheric and Oceanic Technology*, *28*(7), 853–868, doi:10.1175/JTECH-D-10-05004.1.

Sjöholm, M., T. Mikkelsen, J. Mann, K. Enevoldsen, and M. Courtney (2009), Spatial averaging-effects on turbulence measured by a continuous-wave coherent lidar, *Meteorologische Zeitschrift*, *18*(3, Sp. Iss. SI), 281–287, doi:10.1127/0941-2948/2009/0379.

Wyngaard, J. C. (2010), *Turbulence in the Atmosphere*, Cambridge University Press, New York.

Table 1: *Mann* [1994] model parameters to estimate $\Phi_{ij}(\boldsymbol{k})$

Height (m)	$\alpha\epsilon^{2/3}$	L (m)	Γ
60	0.051	46.226	3.158
100	0.037	60.867	2.896

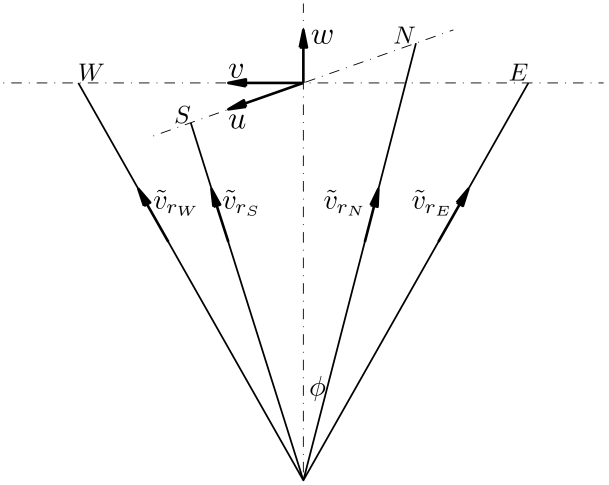

Figure 1: Schematic of the velocity Azimuth display scanning for the WindCube

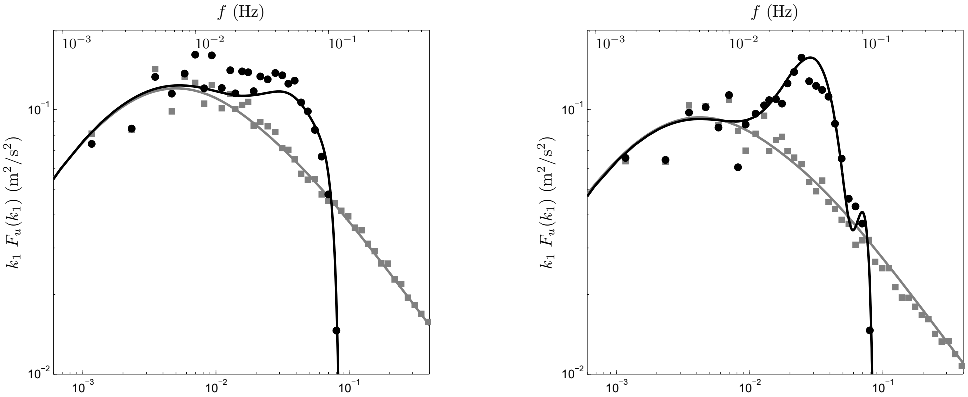

Figure 2: Comparison of the modeled and measured u spectrum at 60 m (left) and 100 m (right). The markers indicate measurements and the continuous line indicates the model. The black and gray markers denote WindCube spectrum and sonic spectrum, respectively.

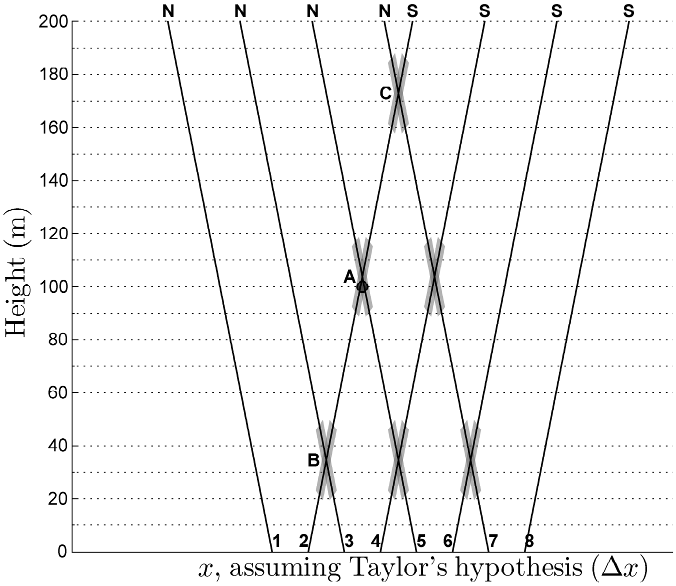

Figure 3: Schematic of the intersection of the North and South Beams. The shaded portion indicates the measurement volume. The black marker indicates a height of 100 m

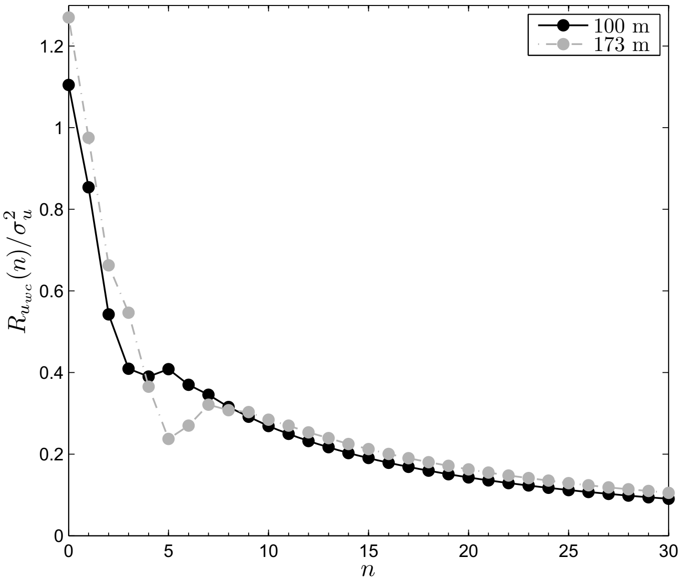

Figure 4: Comparison of $R_{u_{wc}}(n)/\sigma_u^2$ at different heights

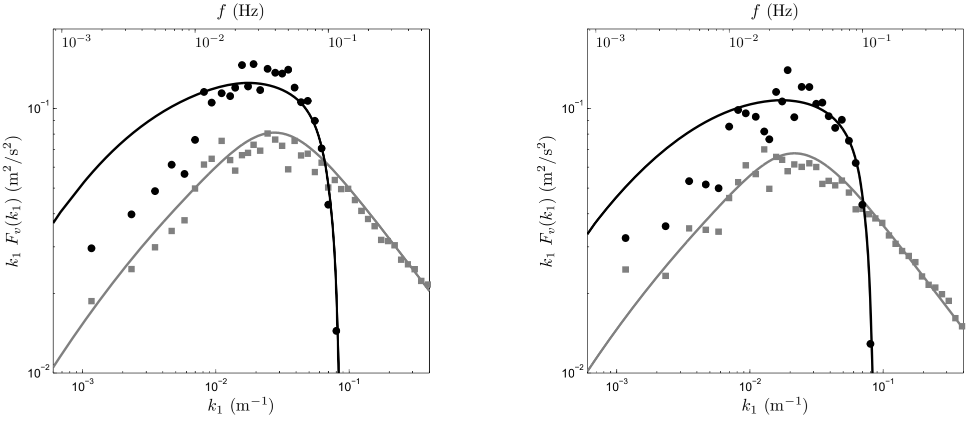

Figure 5: Comparison of the modeled and measured v spectrum at 60 m (left) and 100 m (right). The meaning of the symbols and colors correspond to those in Fig. 2

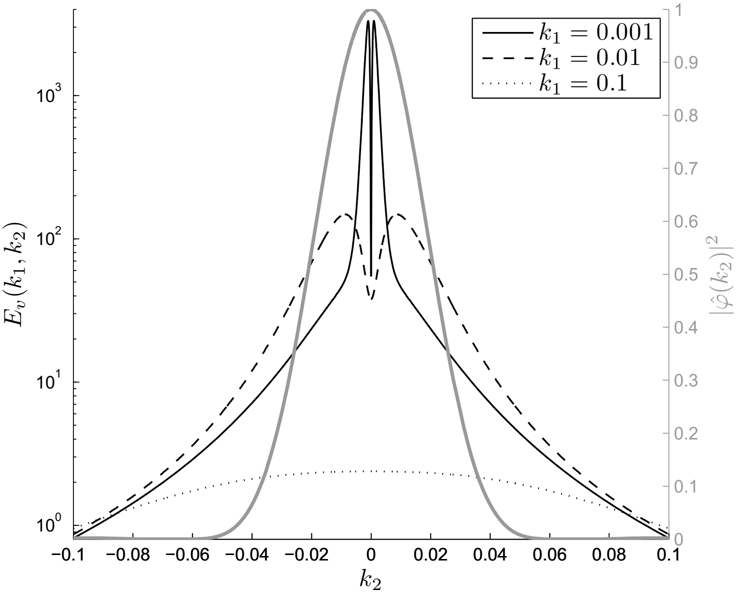

Figure 6: Two-Dimensional energy spectrum of the v component. The weighting function $|\hat{\varphi}(k_2)|^2$ is plotted on the right y-axis

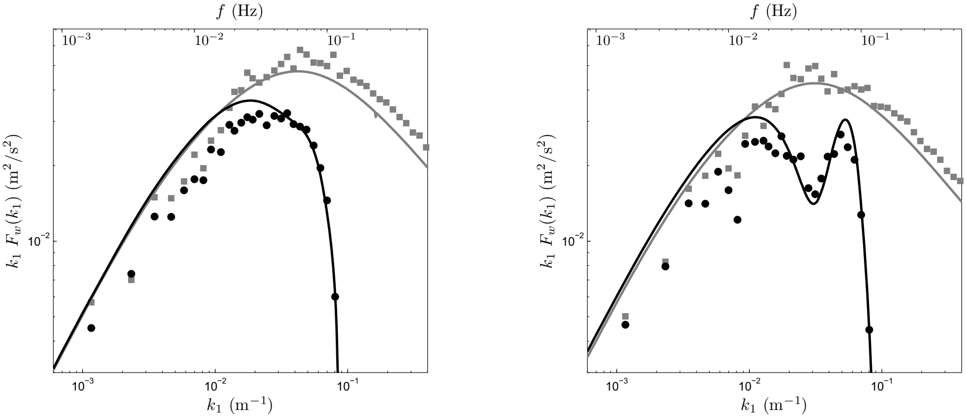

Figure 7: Comparison of the modeled and measured w spectrum at 60 m (left) and 100 m (right). The meaning of the symbols and colors correspond to those in Fig. 2

Chapter 7

How can wind lidars measure turbulence? A preliminary investigation

In chapters 5 and 6 we understood that the VAD scanning technique of measuring turbulence using lidars result in large systematic errors. In this chapter we investigate a new method that in principle has the potential to make turbulence measurements by lidars possible. The method uses six lidar beams to counter the contamination of the measured turbulence by other components of the Reynolds stress tensor. The foundation for this idea was laid down by Eberhard et al. [1989], Mann et al. [2010], where momentum flux was measured using two beams. As a consequence of using six arbitrarily chosen lidar beams the random error in the turbulence measurements will increase. We optimize the beams angles such that these random errors are minimized. Then in principle the only systematic errors that remain in the measurements are the averaging errors due to the large sampling volume in which lidars measure wind speeds. To model these systematic errors, we make use of the Mann [1994] model to describe the three-dimensional turbulence structure.

For both, the continuous-wave (ZephIR) and the pulsed (WindCube) lidars only theoretical calculations of the systematic errors are carried out, which are compared with the calculations for a VAD scanning technique. The measurement using this configuration requires significant hardware changes and are not carried out in this PhD study. The attached paper compares two methods of measurement, the VAD scanning technique and the six-beam method. The description for the VAD scanning technique is an overlap of the work carried out in chapter 5, and only the six beam approach is new work.

Can the available wind lidars measure turbulence?

A. Sathe[a,b][*], J. Mann[a], J. Gottschall[a], M. S. Courtney[a]

[a] *Wind Energy Division, Risø DTU, Roskilde, Denmark, amsat@risoe.dtu.dk*

[b] *L& R, Section Wind Energy, TU Delft, Delft, The Netherlands, A.R.Sathe@tudelft.nl*

1 INTRODUCTION

It is now well established that wind lidars (henceforth referred to as lidars) measure the 10-min mean wind speed with acceptable accuracy. Several measurement campaigns have been carried out in this regard, where cup anemometers are used as reference instruments (Kindler et al., 2007; Peña et al., 2009; Smith et al., 2006). Turbulence measurements using lidars is still a subject of research, and an acceptable method is yet to be established. The turbulence measurements that we refer to in this article are the second-order moments of wind speeds. For wind energy, amongst a whole range of applications, turbulence measurements are useful in the load calculations of wind turbines, power curve measurements and validation of wind profile models.

The current standard for the measurement of turbulence for wind energy purposes is the sonic anemometer, which is a compact instrument that can measure all three components of wind velocity in a relatively small sample volume that for all practical purposes can be considered a point. It needs to be mounted on a meteorological mast (met-mast), such that the flow distortion due to the mast itself is kept to a minimum. Despite this there are disadvantages of using sonic anemometers, the most important being that tall met-masts are very expensive, and offshore, the costs increase significantly. We thus have to look for alternatives. Remote sensing methods such as sodars and lidars are viable alternatives. In this article we restrict the discussion to lidars only.

Although lidars have been introduced in wind energy recently, for meteorology they have been investigated previously to measure turbulence using different scanning techniques. A common technique is by conical scanning and using the velocity azimuth display (VAD) technique of processing the data. One of the first remote sensing (Doppler radar) turbulence studies using a full 360° scan in a horizontal plane was carried out by Browning and Wexler (1968), where the limitations of horizontal homogeneity and vertical wind shear are explained in detail. Wilson (1970) modified the technique from Browning and Wexler (1968) and performed turbulence measurements over snow. Kropfli (1986) extended the technique to accommodate turbulence scales of motion larger than those described in Wilson (1970) and showed that these techniques could be used to make reasonable estimates of turbulent kinetic energy and momentum flux by modelling the random errors in the measurements.

Eberhard et al. (1989) studied turbulence using Doppler lidar and using the variances of the radial velocity, where they modelled the random errors using a partial Fourier decomposition method, which gave better estimates of the errors than Wilson (1970) and Kropfli (1986). Gal-Chen et al. (1992) presented a technique to analyse lidar data for turbulence measurements using the scans at two levels, and produced estimates of fluxes in the mixed layer, and spectra of the horizontal velocity at the surface. Banakh et al. (1995) presented an analysis of estimating the random errors in the measurement of the mean wind speed by lidars using the theory

---

[*] The author is affiliated to Risø DTU and TU Delft

of isotropic turbulence. Banta et al. (2002) studied the turbulence characteristics under the conditions of low-level jets, using the vertical-slice scans of radial velocities. Smalikho et al. (2005) presented a method to use lidar data for the estimation of turbulent energy dissipation rate to study wake vortices of an aircraft. A comprehensive review is given in Engelbart et al. (2007) that covers different remote sensing techniques for turbulence measurements including lidars. A review of the use of lidars for wind energy applications is also presented in Emeis et al. (2007). Pichugina et al. (2008) demonstrated the sensitivity of the streamwise velocity variance to the spatial and temporal averaging, also by using the technique of vertical-slice scans of radial velocities. Recently, studies have been carried out to model the spatial averaging effects (Sjöholm et al., 2009) and compare the 3D turbulence measurements using three staring lidars (Mann et al., 2009). Wagner et al. (2009) modelled the systematic errors by approximating the conical scan and the scan time as a length scale, providing first estimates of the variances of the longitudinal component of wind velocity. Mann et al. (2010) estimated the momentum fluxes using lidars and modelled the unfiltered turbulence from the CW lidar, where the model compares reasonably well with the measurements.

In this article an attempt is made to answer the research question, 'Can the available wind lidars measure turbulence?'. Two approaches are investigated to answer this question. The first is the conical scanning and velocity azimuth display (VAD) technique to process the data, under which a theoretical model is developed to estimate the systematic errors in the second-order moments of wind speeds measured by lidars. The approach is similar to Wyngaard (1968), Citriniti and George (1997), where turbulence measured by the hot-wire anemometer probe was modelled. The systematic errors are the errors that arise due to the averaging effect in the line-of-sight and the quite large circle in which lidars measure wind speed. The second is conically scanning at six azimuth angles and using the variances of the radial velocities from these six beams. This approach has been used previously by (Eberhard et al., 1989), (Mann et al., 2010) to measure momentum flux only. Under our approach, lidar beams are shot at five different azimuth angles and one beam is vertical.

Two types of lidars are considered, the ZephIR developed by QinetiQ (Natural Power) as a continuous wave (CW) lidar and the WindCube developed by Leosphere as a pulsed lidar. The verification is carried out by comparing the variances measured by the ZephIR and WindCube with that of the sonic anemometers placed at different heights on a met-mast.

2 APPROACH 1 – CONICAL SCANNING AND VAD TECHNIQUE TO PROCESS LIDAR DATA

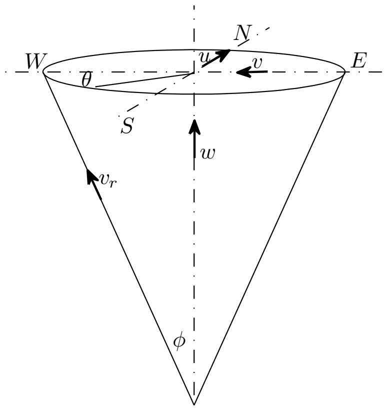

Figure 1: Schematic of the velocity azimuth display scanning

Fig. 1 shows the lidar emitting the laser beam at different azimuth angles θ. The azimuth angles increase from 0°–360° in the clockwise direction as for the geographical convention. The line-of-sight velocity (also called radial velocity v_r) is measured by the lidar at each azimuth angle. The half-opening angle ϕ ($= 90° -$ elevation angle) is kept constant throughout the scan. The CW and pulsed lidars work on the principle of backscattering of the emitted radiation, and subsequent detection of the Doppler shift in the frequency of the received radiation. The Doppler shift in the frequency is related to v_r by,

$$\delta f = 2\frac{v_r}{\lambda}, \tag{1}$$

where f and λ are the frequency and wavelength of the emitted radiation. Mathematically, v_r is given as the dot product of the unit directional vector and the velocity field at the point of focus for a CW lidar, and the center of the range gate (Lindelöw, 2007) for the pulsed lidar,

$$v_r(\theta) = \boldsymbol{n}(\theta) \cdot \mathbf{v}(d_f \boldsymbol{n}(\theta)), \tag{2}$$

where d_f is the focus distance for the CW lidar or the distance to the center of the range gate for the pulsed lidar at which the wind speeds are measured, $\mathbf{v} = (u, v, w)$ is the instantaneous velocity field evaluated at the focus point or the center of the range gate $d_f \boldsymbol{n}(\theta)$, and $\boldsymbol{n}(\theta)$ is the unit directional vector given as,

$$\boldsymbol{n}(\theta) = (\cos\theta \sin\phi, \sin\theta \sin\phi, \cos\phi). \tag{3}$$

In practice it is impossible to obtain the backscattered radiation precisely from only the focus point, and there is always backscattered radiation of different intensities from different regions in space along the line-of-sight. Hence, it is necessary to assign appropriate weights to the backscattered intensity such that the weight corresponding to the focus point or the center of the range gate is the highest. Mathematically, the weighted average radial velocity can be written as,

$$\tilde{v}_r(\theta) = \int_{-\infty}^{\infty} \varphi(s) \boldsymbol{n}(\theta) \cdot \mathbf{v}(s\boldsymbol{n}(\theta) + d_f \boldsymbol{n}(\theta))\, ds, \tag{4}$$

where $\varphi(s)$ is any weighting function, integrating to one, and s is the distance along the beam from the focus. For simplicity we assume that $s = 0$ corresponds to the focus distance. Following are the main assumptions of our model:

1. The terrain is homogeneous
2. The flow field is frozen during the scan
3. Eq. (4) with an appropriately chosen $\varphi(s)$ models the averaging well
4. The spatial structure of the turbulent flow is described well by the spectral tensor model of Mann (1994)

We derive the expressions for the CW lidar (ZephIR) only, since the same approach is used for the pulsed lidar (Windcube). If we assume the coordinate system such that u is aligned to the mean wind direction, v is perpendicular to the mean wind direction, w is the vertical component, and the mean wind comes from the North then $\tilde{v}_r(\theta)$ can be expressed as,

$$\tilde{v}_r(\theta) = A + B\cos\theta + C\sin\theta, \tag{5}$$

where the coefficients $A = w_{qq}\ \cos\phi$, $B = u_{qq}\ \sin\phi$ and $C = v_{qq}\ \sin\phi$ and the sign ambiguity in $\tilde{v}_r(\theta)$ is neglected (see Mann et al. (2010)). We use the subscript qq to denote the velocity components measured by ZephIR, since they are not the true velocity components u, v and w. The assumption that the mean wind comes from the North is only made for simplicity. For a lidar measuring at many points on the azimuth circle the choice of the mean wind direction does not matter since averaging over the entire circle is carried out. The values of the coefficients A, B and C are found using least squares method by fitting Eq. (5) to the measured values of $\tilde{v}_r(\theta)$ at all scanned azimuth angles. The coefficients can be written as Fourier integrals,

$$\begin{aligned} A &= \frac{1}{2\pi}\int_0^{2\pi} \tilde{v}_r(\theta)\, d\theta, && (6)\\ B &= \frac{1}{\pi}\int_0^{2\pi} \tilde{v}_r(\theta)\, \cos\theta\, d\theta, && (7)\\ C &= \frac{1}{\pi}\int_0^{2\pi} \tilde{v}_r(\theta)\, \sin\theta\, d\theta. && (8)\end{aligned}$$

We proceed by deriving expressions for the w_{qq} variance. The expressions for the (co-) variances of the remaining components of wind velocity can be derived in a similar manner.

The variance of A is defined as $\sigma_A^2 = \langle A'^2 \rangle$, where $\langle\rangle$ denotes ensemble averaging of a variable. From the above definition of A we can write,

$$\sigma_A^2 = \langle w'^2_{qq} \rangle \cos^2\phi. \tag{9}$$

Using Eq. (6) we can also write,

$$\sigma_A^2 = \left\langle \left(\frac{1}{2\pi}\int_0^{2\pi} \tilde{v}'_r(\theta)\, d\theta \right)^2 \right\rangle. \tag{10}$$

Lengthy manipulations allow us to express σ_A^2 in terms of the three-dimensional spectral velocity tensor $\Phi_{ij}(\boldsymbol{k})$, which is the Fourier transform of the covariance tensor. Let $\alpha_i(\boldsymbol{k}) = \left(\int_{-\infty}^{\infty} \varphi(s) \left[\frac{1}{2\pi}\int_0^{2\pi} n_i(\theta) e^{\mathrm{i}(s+d_f)\boldsymbol{k}\cdot\boldsymbol{n}(\theta)}\, d\theta\right] ds\right)$, which physically represents the line-of-sight and conical averaging. Eq. (10) can then be written as (using Eq. 9),

$$\langle w'^2_{qq} \rangle \cos^2\phi = \int \Phi_{ij}(\boldsymbol{k}) \alpha_i(\boldsymbol{k}) \alpha_j^*(\boldsymbol{k})\, d\boldsymbol{k}, \tag{11}$$

where $*$ denotes complex conjugation. Thus the integral reduces to evaluating $\alpha_i(\boldsymbol{k})$, since the analytical expressions for $\Phi_{ij}(\boldsymbol{k})$ are given in Mann (1994). Eq. (11) can then be estimated numerically. For a CW lidar, $\varphi(s)$ is well approximated by a Lorentzian function (Sonnenschein and Horrigan, 1971),

$$\varphi(s) = \frac{1}{\pi}\frac{l}{l^2+s^2}, \tag{12}$$

where l is the Rayleigh length ($= \lambda_b d_f^2/\pi r_b^2$, where $\lambda_b = 1.55\ \mu$m is the wavelength of the emitted radiation, and $r_b = 19.5$ mm is the beam radius). The resulting $\langle w'^2_{qq} \rangle$ can now be evaluated and a similar approach is taken for deriving $\langle u'^2_{qq} \rangle$ and $\langle v'^2_{qq} \rangle$ variances, and for the variances measured by the Windcube. An additional complication for the ZephIR is that the beam rotates three times calling for an extra averaging in time, which is included in the theoretical prediction in Fig. (2a), see Sathe et al. (2011) for details. We present the systematic errors as the ratio of the lidar second-order moments and the true second-order moment.

2.1 *Comparison of the models with the measurements*

The measurements were performed at the Danish National Test Center for Large Wind Turbines at Høvsøre, Denmark. The site is about 2 km from the west coast of Denmark. The eastern sector is characterized by flat homogeneous terrain, and to the south is a lagoon. Our reference measurements for this study are the sonic anemometer measurements taken at 40, 60, 80 and

100 m. The measured three-dimensional wind speeds are resolved with a frequency of 20 Hz and then reduced to the respective 10-min statistics (mean values and standard deviations or variances). All sonic anemometers are placed on the North booms of the met-mast, resulting in unusable data when the wind is from the south due to the wake of the mast. In combination with the sonic measurements, wind speeds from a ZephIR and a WindCube are used. Reference and lidar data were collected over two different time periods, for the WindCube between January and April 2009, and for the ZephIR between April and November 2009. In order to further avoid the influence of the wakes from the wind turbines and the met. mast on lidar measurements, and inhomogeneities due to the sudden change of roughness (sea-land transition), only data periods with easterly winds (50°–150°) are analyzed. For the ZephIr 5530 data points were used after using all the filter, whereas for the WindCube 4003 data points were used.

The estimation of Φ_{ij} using the model from Mann (1994) requires three input parameters, $\alpha\varepsilon^{2/3}$, which is a product of the spectral Kolmogorov constant α (Monin and Yaglom, 1975) and the rate of viscous dissipation of specific turbulent kinetic energy $\varepsilon^{2/3}$, a length scale L and an anisotropy parameter Γ. We use these input parameters obtained by fitting the sonic anemometer measurements under different atmospheric stability conditions, at several heights on the meteorological mast in the eastern sector (Peña et al., 2010).

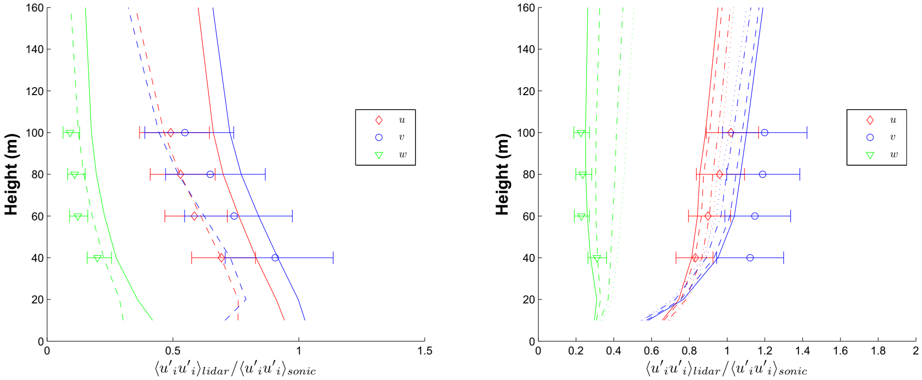

(a) ZephIR (b) WC

Figure 2: ZephIR and WindCube systematic errors under neutral conditions. The markers indicate measurements. For the ZephIR, solid lines are the theoretical plots without the low-pass filter, and the dashed lines are with the low-pass filter. For the WindCube, the model variation with wind direction is plotted as dotted line for 0°, dash-dot line for 15°, dashed line for 30° and solid line for 45°

Fig. 2 shows the comparison between the modelled systematic error and the measurements at flat terrain test site in Denmark. Although the results are obtained under different atmospheric stability conditions we show the results for only the neutral condition. We infer the following:

- For the ZephIR, the systematic errors increase with height. This is due to a quadratic increase in the probe length with height (Lindelöw, 2007). The diameter of the scanning circle also increases with height. This results in a greater attenuation of the second-order moments with increasing height.

  For the WindCube the systematic errors decrease with height for the u and v variances, where the probe length is constant (Lindelöw, 2007), and hence, at lower heights there is a combined averaging effect due to the probe length and the diameter of the scanning circle. Considering that at lower heights the length scales are smaller than at higher heights, it is likely that the variances are attenuated greater at lower heights than at higher heights. For w variance, the systematic error is approximately constant, and is most likely due to the small length scales.

- The systematic errors in w variance is much larger (approximately 3-5 times) than that of the u and v variances for both lidars. This is due to the very small length scales of the w component as compared to those for u and v, resulting in the attenuation of the w variance of up to 90%. The u and v variances are attenuated up to 70%.
- For both lidars there is a significant spread (first and third quartiles) in the systematic errors of u and v variances – These are the random errors and most likely occur due to the disjunct sampling (Lenschow et al., 1994) for the ZephIR. For the WindCube, the spread in the systematic error (first and third quartiles) of the u and v variances is smaller than that of the ZephIR. This is most likely because the WindCube updates the velocity vector approximately every 6.5 seconds, whereas the ZephIR updates every 18 seconds.
- In general, the trend of the systematic errors predicted by the models (low-pass filering for ZephIR) for both lidars is in agreement with the observations at all heights.
- For the WindCube, the systematic error varies significantly with the wind direction relative to the beam direction for w variance, and to a lesser degree for u and v variance under all stability conditions.

2.2 *Summary*

The systematic errors of the second-order moments measured by lidars using the conical scanning and VAD technique to process the data are quite large due to

1. the spatial separation of the data points along the line-of-sight and
2. the spatial separation of the data points in the conical section.

The general lidar equation for the second-order moments using the VAD data processing technique can be written as,

$$\begin{aligned} \langle \mathrm{v}'_m \mathrm{v}'_n \rangle_{lidar} &= \int \Phi_{ij}(\boldsymbol{k}) X_i^m(\boldsymbol{k}) X_j^{*n}(\boldsymbol{k})\, d\boldsymbol{k}; \qquad (13) \\ X_i^m(\boldsymbol{k}) &= \begin{cases} \beta_i(\boldsymbol{k}) \bigwedge b_i(\boldsymbol{k}), & m = 1 \\ \gamma_i(\boldsymbol{k}) \bigwedge c_i(\boldsymbol{k}), & m = 2 \\ \alpha_i(\boldsymbol{k}) \bigwedge a_i(\boldsymbol{k}), & m = 3 \end{cases} \end{aligned}$$

The weighting functions $\alpha_i(\boldsymbol{k})$, $\beta_i(\boldsymbol{k})$, $\gamma_i(\boldsymbol{k})$ are used for the ZephIR and $a_i(\boldsymbol{k})$, $b_i(\boldsymbol{k})$, $c_i(\boldsymbol{k})$ are used for the WindCube. Thus, the measurement of the second-order moment by lidar involves interaction of all components of the spectral velocity tensor $\Phi_{ij}(\boldsymbol{k})$ weighted by the corresponding weighting functions $X_i^m(\boldsymbol{k})$ and $Y_j^{*n}(\boldsymbol{k})$. It is to be noted that Eqn. (13) is given in Einstein summation convention, and hence, in order to explicitly see the contribution of all components of $\Phi_{ij}(\boldsymbol{k})$ on the measurement of the second-order moments by lidar, this equation must be expanded for all values of the subscripts i and j. In most cases, this results in the attenuation of the second-order moments, whereas in some cases this also results in amplification of the second-order moment.

3 APPROACH 2 – A SIX BEAM APPROACH

Having understood that the VAD technique results in large systematic errors in the turbulence measurements, we investigate a new method method to measure turbulence using the same lidars. Following Eberhard et al. (1989); Mann et al. (2010),

$$\begin{aligned}\langle {v'_r}^2\rangle &= \langle u'^2\rangle \sin^2\phi\cos^2\theta + \langle v'^2\rangle \sin^2\phi\sin^2\theta + \langle w'^2\rangle \cos^2\phi \\ &\quad + 2\langle u'v'\rangle \sin^2\phi\sin\theta\cos\theta + 2\langle u'w'\rangle \sin\phi\cos\phi\cos\theta + 2\langle v'w'\rangle \sin\phi\cos\phi\sin\theta\end{aligned} \tag{14}$$

where $\langle {v'_r}^2\rangle$ is the radial velocity variance. Since there are six unknowns, we need six equations to solve for the set of the second-order moments,

$$\Sigma = \Big(\langle u'^2\rangle, \langle v'^2\rangle, \langle w'^2\rangle, \langle u'v'\rangle, \langle u'w'\rangle, \langle v'w'\rangle\Big) \tag{15}$$

Scanning the circle at only one half opening angle, using Eq. (14) there are infinite solutions for the set Σ. Thus, we need more than one value of ϕ to obtain a solution for Σ. The challenge is to obtain the optimum combination of $\boldsymbol{X} = (\theta_i, \phi_i)|_{i..6}$. If we represent Eq. (14) as a system of linear equations then in matrix form we can write,

$$\Sigma = \boldsymbol{M}^{-1}\boldsymbol{S} \tag{16}$$

where, $\boldsymbol{M}$ is a 6×6 matrix of the coefficients of Σ, and $\boldsymbol{S} = \Big(\langle {v'_{r_1}}^2\rangle, \langle {v'_{r_2}}^2\rangle, ..., \langle {v'_{r_6}}^2\rangle\Big)$ is the set of the variances of radial velocities.

3.1 *Formulating the objective function*

The coordinate system for lidars is a left-handed coordinate system. In order to align with the mean wind direction, we need to apply coordinate transformations on any tensors that are defined in the original coordinate system. Thus, the second order tensor $\langle mathrmv'_i mathrmv'_j\rangle$ rotated clockwise in the mean wind direction has to be multiplied by a transformation matrix $\boldsymbol{T}$ given as,

$$\boldsymbol{T} = \begin{bmatrix} \cos\Theta & \sin\Theta & 0 \\ -\sin\Theta & \cos\Theta & 0 \\ 0 & 0 & 1 \end{bmatrix} \tag{17}$$

In the cartesian-tensor suffix notation, for a second-order tensor, we can write,

$$\langle \tilde{\mathrm{v}}'_k \tilde{\mathrm{v}}'_l\rangle = T_{ik}T_{jl}\langle \mathrm{v}'_i \mathrm{v}'_j\rangle \tag{18}$$

where $\langle \tilde{\mathrm{v}}'_i \tilde{\mathrm{v}}'_j\rangle$ are the second-order moments in the coordinate system rotated in the mean wind direction, and $T_{ik}T_{jl}$ are the direction cosines. Since $\langle \mathrm{v}'_i \mathrm{v}'_j\rangle$ is a symmetric second-order tensor, we are only interested in the set Σ given by Eq. 15. Using Einstein's summation, we get for each component of the set $\tilde{\Sigma}$,

$$\begin{aligned}
\langle \tilde{u'^2}\rangle &= \langle u'^2\rangle\cos^2\Theta + \langle v'^2\rangle\sin^2\Theta + \langle u'v'\rangle\sin 2\Theta && (19)\\
\langle \tilde{v'^2}\rangle &= \langle u'^2\rangle\sin^2\Theta + \langle v'^2\rangle\cos^2\Theta - \langle u'v'\rangle\sin 2\Theta && (20)\\
\langle \tilde{w'^2}\rangle &= \langle w'^2\rangle && (21)\\
\langle \widetilde{u'v'}\rangle &= -\frac{1}{2}\sin 2\Theta\langle u'^2\rangle + \frac{1}{2}\sin 2\Theta\langle v'^2\rangle + \langle u'v'\rangle\cos 2\Theta && (22)\\
\langle \widetilde{u'w'}\rangle &= \langle u'w'\rangle\cos\Theta + \langle v'w'\rangle\sin\Theta && (23)\\
\langle \widetilde{v'w'}\rangle &= -\langle u'w'\rangle\sin\Theta + \langle v'w'\rangle\cos\Theta && (24)
\end{aligned}$$

where $\tilde{\Sigma} = \left(\langle \tilde{u'^2}\rangle, \langle \tilde{v'^2}\rangle, \langle \tilde{w'^2}\rangle, \langle \widetilde{u'v'}\rangle, \langle \widetilde{u'w'}\rangle, \langle \widetilde{v'w'}\rangle\right)$ is the set of second-order moments in the coordinate system rotated in the mean wind direction. In matrix form, Eqs. (19–24) can be written as,

$$\begin{aligned}
\begin{bmatrix} \langle \tilde{u'^2}\rangle \\ \langle \tilde{v'^2}\rangle \\ \langle \tilde{w'^2}\rangle \\ \langle \widetilde{u'v'}\rangle \\ \langle \widetilde{u'w'}\rangle \\ \langle \widetilde{v'w'}\rangle \end{bmatrix} &= \begin{bmatrix} \cos^2\Theta & \sin^2\Theta & 0 & \sin 2\Theta & 0 & 0 \\ \sin^2\Theta & \cos^2\Theta & 0 & -\sin 2\Theta & 0 & 0 \\ 0 & 0 & 1 & 0 & 0 & 0 \\ -\frac{1}{2}\sin 2\Theta & \frac{1}{2}\sin 2\Theta & 0 & \cos 2\Theta & 0 & 0 \\ 0 & 0 & 0 & 0 & \cos\Theta & \sin\Theta \\ 0 & 0 & 0 & 0 & -\sin\Theta & \cos\Theta \end{bmatrix} \begin{bmatrix} \langle u'^2\rangle \\ \langle v'^2\rangle \\ \langle w'^2\rangle \\ \langle u'v'\rangle \\ \langle u'w'\rangle \\ \langle v'w'\rangle \end{bmatrix} && (25) \\
\tilde{\Sigma} &= \boldsymbol{R}\Sigma && (26)
\end{aligned}$$

where $\boldsymbol{R}$ is the transformation matrix to be applied on the set Σ to obtain $\tilde{\Sigma}$ in the rotated coordinate system. Using Eq. (16), we can write,

$$\boldsymbol{\delta}\tilde{\boldsymbol{\Sigma}} = \boldsymbol{R}\boldsymbol{M}^{-1}\boldsymbol{\delta S} \tag{27}$$

where $\boldsymbol{\delta}\tilde{\boldsymbol{\Sigma}}$ and $\boldsymbol{\delta S}$ are the random errors in the second-order moments and radial velocity variances respectively. Following lengthy manipulations, we get

$$\frac{\langle \boldsymbol{\delta}\tilde{\boldsymbol{\Sigma}} \cdot \boldsymbol{\delta}\tilde{\boldsymbol{\Sigma}}\rangle}{\langle \varepsilon_s^2\rangle} = Tr(\boldsymbol{RN}(\boldsymbol{RN})^T) \tag{28}$$

where $N = M^{-1}$, Tr denotes trace of a matrix, T denotes matrix transpose, and $\langle \varepsilon_s^2\rangle$ is the error variance of the radial velocities. In deriving Eq. (28) we have assumed that the error variance of the radial velocity is equal for all six beams. Eq. (28) states that the error variance is dependent on the mean wind direction. In order to make it independent of the mean wind direction, we assume a uniform distribution of the mean wind direction, and estimate the averaged ratio of the error variance. Thus,

$$\begin{aligned}
\left\langle \frac{\langle \boldsymbol{\delta}\tilde{\boldsymbol{\Sigma}} \cdot \boldsymbol{\delta}\tilde{\boldsymbol{\Sigma}}\rangle}{\langle \varepsilon_s^2\rangle} \right\rangle &= \frac{1}{2\pi}\int_0^{2\pi} Tr(\boldsymbol{RN}(\boldsymbol{RN})^T)d\Theta \\
&= \frac{1}{2\pi}\int_0^{2\pi} Tr(\boldsymbol{RNN}^T\boldsymbol{R}^T)d\Theta
\end{aligned}$$

Using the property of matrix trace that it is invariant under cyclic permutations we get,

$$\left\langle \frac{\langle \boldsymbol{\delta}\tilde{\boldsymbol{\Sigma}} \cdot \boldsymbol{\delta}\tilde{\boldsymbol{\Sigma}}\rangle}{\langle \varepsilon_s^2\rangle} \right\rangle = \frac{1}{2\pi}\int_0^{2\pi} Tr(\boldsymbol{R}^T\boldsymbol{RNN}^T)d\Theta \tag{29}$$

We can also switch the order between integration and matrix trace, i.e. either we can estimate the trace first and then the integration or vice-versa. Thus,

$$\left\langle \frac{\langle \boldsymbol{\delta}\tilde{\boldsymbol{\Sigma}} \cdot \boldsymbol{\delta}\tilde{\boldsymbol{\Sigma}}\rangle}{\langle \varepsilon_s^2\rangle} \right\rangle = Tr\left(\left[\frac{1}{2\pi}\int_0^{2\pi} \boldsymbol{R}^T\boldsymbol{R}d\Theta\right]\boldsymbol{NN}^T\right) \tag{30}$$

Solving the integral we get,

$$\left\langle \frac{\langle \boldsymbol{\delta}\tilde{\boldsymbol{\Sigma}} \cdot \boldsymbol{\delta}\tilde{\boldsymbol{\Sigma}}\rangle}{\langle \varepsilon_s^2\rangle} \right\rangle = Tr\left(\begin{bmatrix} \frac{7}{8} & \frac{1}{8} & 0 & 0 & 0 & 0 \\ \frac{1}{8} & \frac{7}{8} & 0 & 0 & 0 & 0 \\ 0 & 0 & 1 & 0 & 0 & 0 \\ 0 & 0 & 0 & \frac{3}{2} & 0 & 0 \\ 0 & 0 & 0 & 0 & 1 & 0 \\ 0 & 0 & 0 & 0 & 0 & 1 \end{bmatrix} \boldsymbol{NN}^T\right) \tag{31}$$

3.2 *Optimizing the objective function*

From (Eq. 31), it is clear that we need to optimize for 12 variables, i.e. a set $\boldsymbol{X} = (\theta_i, \phi_i)|_{i=1..6}$. The constraints constitute the range of angles of θ_i and ϕ_i. Thus, the optimization problem can be stated as follows:

$$\text{Minimize } f(\boldsymbol{X}) = Tr\left(\begin{bmatrix} \frac{7}{8} & \frac{1}{8} & 0 & 0 & 0 & 0 \\ \frac{1}{8} & \frac{7}{8} & 0 & 0 & 0 & 0 \\ 0 & 0 & 1 & 0 & 0 & 0 \\ 0 & 0 & 0 & \frac{3}{2} & 0 & 0 \\ 0 & 0 & 0 & 0 & 1 & 0 \\ 0 & 0 & 0 & 0 & 0 & 1 \end{bmatrix} \boldsymbol{N}\boldsymbol{N}^T\right) \tag{32}$$

subject to constraints,
$0^\circ \leq \theta_i|_{i=1..6} \leq 360^\circ$
$0^\circ \leq \phi_i|_{i=1..6} \leq 45^\circ$

We assume that statistical homogeneity in the horizontal direction is valid only for a maximum value of $\phi_i = 45^\circ$. Analytical optimization of Eq. (32) provides a unique design solution set $\boldsymbol{X}$. However, Eq. (32) is a very complicated optimization problem, and hence, analytical solution is not possible[1]. In that case, the simplest method is to solve Eq. (32) for different combinations of $\boldsymbol{X}$. However, this would need very large number of computations. E.g. if we assume that $\boldsymbol{X}$ take only integer values, the number of computations required are $360^6 \times 90^6 \approx O(10^{27})$. It is observed that one computation of $f(\boldsymbol{X})$ takes approximately 0.5 seconds. Thus 10^{27} computations need approximately 10^{17} years. Moreover, if $\boldsymbol{X}$ also take real values then the number of computations, and hence, the time required increase manyfold. Thus, with the current available computer resources it is seen that evaluating $f(\boldsymbol{X})$ by directly substituting for different sets of $\boldsymbol{X}$ is not possible. We are thus forced to use available numerical optimization techniques.

There are two classes of numerical methods to solve a non-linear optimization problem Rao (2009):

1. Direct search methods
2. Gradient methods

For gradient methods, it is essential that the objective function is differentiable, and ∇f is defined at all points, i.e. $f(\boldsymbol{X})$ is not discontinuous Rao (2009). For simplicity we assume that $f(\boldsymbol{X})$ is discontinuous, and hence, we cannot use gradient methods. Thus, we optimize Eq. (32) using direct search methods only. The main advantage of using direct search methods is that they can be used for discontinuous and non-differentiable functions. The main limitation of such methods is that the found optimum may only be a local optimum.

In principle, any direct search algorithm can be used to find an optimum solution. It is generally very cumbersome to write algorithms for all available methods, and hence, we use the already available algorithms in Mathematica. For a global optimization problem, four different algorithms are available in Mathematica:

1. Simplex (NM) Nelder and Mead (1965)
2. Differential Evolution (DE) Storn and Price (1997)
3. Simulated Annealing (SA) Ingber (1993)
4. Random Search (RS) Rao (2009)

Eventually, we have to choose a solution set from one of these algorithms.

---

[1] Corresponding attempt is made in Mathematica

Table 1: Comparison of the optimization methods

	Optimization Methods							
	Nelder-Mead		Differential Evolution		Simulated Annealing		Random Search	
$\langle \boldsymbol{\delta\Sigma} \cdot \boldsymbol{\delta\Sigma} \rangle / \langle \varepsilon_s^2 \rangle$	10.2		11.78		10.2		10.2	
i	θ_i	ϕ_i	θ_i	ϕ_i	θ_i	ϕ_i	θ_i	ϕ_i
1	0	45	0	44.9999	0	45	0	45
2	284.451	1.087e-7	109.771	0.00087255	72	45	216	45
3	144	45	233.185	43.8284	297.23	6.8733e-6	143.035	6.6121e-15
4	288	45	310.453	44.9993	216	45	144	45
5	72	45	144.495	44.9333	288	45	72	45
6	216	45	89.3294	44.9993	144	45	288	45

Table 1 gives a comparison of different optimization methods, when $\boldsymbol{X}$ is constrained to take real values. It is observed that the NM, SA and RS methods give the same optimum $f(\boldsymbol{X}^*)$. The DE method gives a slightly higher value of the optimum. $\boldsymbol{X}$ is evaluated to machine precision. However, in reality it is difficult to orient the laser beam at such precise angles ϕ_i. Hence, we rounded $\boldsymbol{X}^*$ to the nearest integer values and checked its influence on $f(\boldsymbol{X}^*)$. We found that there is no influence of rounding of $\boldsymbol{X}^*$ on $f(\boldsymbol{X}^*)$.

3.3 *Results*

Following section 2 we can estimate the second-order moments using the six beam approach. We choose $\boldsymbol{X}$ from the SA method. Since the NM and RS methods also give the same optimum solution, $\boldsymbol{X}$ could also be chosen from these methods. From Eq. (27) the u variance can be written as,

$$\langle \tilde{u'^2} \rangle = \langle v'^2_{r_1} \rangle - \langle v'^2_{r_3} \rangle - 0.085 \left(\langle v'^2_{r_2} \rangle + \langle v'^2_{r_5} \rangle \right) + 0.585 \left(\langle v'^2_{r_4} \rangle + \langle v'^2_{r_6} \rangle \right) \tag{33}$$

Following section 2 we get,

$$\langle v'^2_{r_1} \rangle = \int \Phi_{ij}(\boldsymbol{k}) \beta_{i1}(\boldsymbol{k}) \beta^*_{j1}(\boldsymbol{k}) d\boldsymbol{k} \tag{34}$$

where $\beta_{i1}(\boldsymbol{k}) = \left(\int_{-\infty}^{\infty} \varphi(s) n_{i1} e^{\mathrm{i}(s+d_f)\boldsymbol{k}\cdot\boldsymbol{n}_1} ds \right)$ and $*$ denotes complex conjugation. We can then use appropriate weighting function $\varphi(s)$ to estimate $\beta_{i1}(\boldsymbol{k})$. We can estimate the variances of the radial velocities in the remaining beam directions in a similar manner and substitute in Eq. (33) to theoretically estimate the u variance measured by the lidar. The remaining second-order moments are estimated in a similar manner.

Fig. (3) shows theoretical comparison of the systematic errors using the six beam approach with that using the VAD technique. Although the results are obtained for all stability conditions, only the neutral conditions are shown. One striking difference between two approaches is that the systematic error in the w variance is reduced significantly using the six beam approach. For the ZephIR, the systematic errors in u and v variances are the same for both approaches. For the Windcube, a significant improvement is obtained for all variances using the six beam approach. Although, fig. (3b) shows that the VAD technique gives lower systematic error, it is mainly due to the addition and subtraction of all second-order moments. This effect is less observed using the six beam approach. The only form of filtering that remains is the line-of-sight averaging. It has been observed that the Windcube systematic errors remain constant for the neutral and unstable conditions (not shown) using the six beam approach. Such is not the case with the VAD technique, where there is an over estimation of the variances.

3.4 *Future work*

The theoretical estimations using the six beam approach will be compared with the measurements. Currently, the experiment is ongoing to measure the second-order moments using the

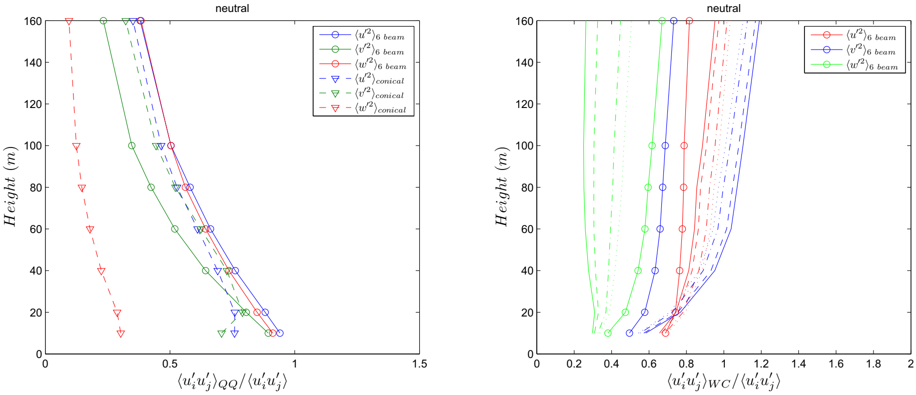

(a) ZephIR

(b) Windcube

Figure 3: Comparison of the ZephIR and Windcube systematic errors under neutral conditions using the six Beam approach and the VAD technique

windscanner developed at Risø DTU. Subsequently, following Mann et al. (2010) a spatial filter model that negates the line-of-sight averaging will be used, which in principle will completely get rid of any filtering of the turbulence.

4 CONCLUSION

Two approaches have been investigated to measure turbulence. Using the VAD technique it is clear that the systematic errors of the second-order moments are quite large, and hence, the ZephIR and WindCube cannot be used to measure turbulence precisely. Using the six beam approach, the theoretical results look promising for the Windcube, whereas there is no improvement for the ZephIR. A final conclusion can only be derived once the measurements are compared with the theoretical results.

ACKNOWLEDGEMENTS

This study is a part of the PhD project under the We@Sea program, BISK-03041, and sponsored by the Dutch Ministry of Economic affairs. The experimental results are all based on data collected at the Høvsøre Test Station under the watchful eyes of Anders Ramsing Vestergaard and Bjarne Sønderskov. Our thanks to them for their highly professional and good-humoured assistance. This paper has been prepared using resources provided by the EU FP6 UpWind project (Project reference 019945 SES6) and by the Center for computational wind turbine aerodynamics and atmospheric turbulence funded by the Danish Council for Strategic Research grant no. 09-067216.We also acknowledge funding for this work under the European Commissions FP7 SafeWind Project, Grant Agreement no. 213740.

References

Banakh, V. A., Smalikho, I. N., Köpp, F., and Werner, C. (1995). Representativeness of wind measurements with a CW Doppler lidar in the atmospheric boundary layer. *Applied optics*, 34(12):2055–2067.

Banta, R. M., Newsom, R. K., Lundquist, J. K., Pichugina, Y. L., Coulter, R. L., and Mahrt, L. (2002). Nocturnal low-level jet characteristics over Kansas during CASES-99. *Boundary-Layer Meteorology*, 105:221–252.

Browning, K. A. and Wexler, R. (1968). The determination of kinematic properties of a wind field using a Doppler radar. *Journal of Applied Meteorology*, 7:105–113.

Citriniti, J. H. and George, W. K. (1997). The reduction of spatial aliasing by long hot-wire anemometer probes. *Experiments in Fluids*, 23:217–224.

Eberhard, W. L., Cupp, R. E., and Healy, K. R. (1989). Doppler lidar measurements of profiles of turbulence and momentum flux. *Journal of Atmospheric and Oceanic Technology*, 6:809–819.

Emeis, S., Harris, M., and Banta, R. M. (2007). Boundary-layer anemometry by optical remote sensing for wind energy applications. *Meteorologische Zeitschrift*, 16(4):337–347.

Engelbart, D. A. M., Kallistratova, M., and Kouznetsov, R. (2007). Determination of the turbulent fluxes of heat and momentum in the ABL by ground-based remote-sensing techniques (a review). *Meteorologische Zeitschrift*, 16(4):325–335.

Gal-Chen, T., Xu, M., and Eberhard, W. L. (1992). Estimation of atmospheric boundary layer fluxes and other turbulence parameters from Doppler lidar data. *Journal of Geophysical Research*, 97(D17):18,409–18,423.

Ingber, L. (1993). Simulated annealing: Practice versus theory. *Mathematical Computer Modelling*, 18(11):29–57.

Kindler, D., Oldroyd, A., Macaskill, A., and Finch, D. (2007). An eight month test campaign of the QinetiQ ZephIR system: Preliminary results. *Meteorologische Zeitschrift*, 16(5):479–489.

Kropfli, R. A. (1986). Single Doppler radar measurement of turbulence profiles in the convective boundary layer. *Journal of Atmospheric and Oceanic Technology*, 3:305–314.

Lenschow, D. H., Mann, J., and Kristensen, L. (1994). How long is long enough when measuring fluxes and other turbulence statistics? *Journal of Atmospheric and Oceanic Technology*, 11:661–673.

Lindelöw, P. (2007). *Fibre Based Coherent Lidars for Remote Wind Sensing*. PhD thesis, Technical University Denmark.

Mann, J. (1994). The spatial structure of neutral atmospheric surface-layer turbulence. *Journal of Fluid Mechanics*, 273:141–168.

Mann, J., Cariou, J., Courtney, M., Parmentier, R., Mikkelsen, T., Wagner, R., Lindelow, P., Sjöholm, M., and Enevoldsen, K. (2009). Comparison of 3D turbulence measurements using three staring wind lidars and a sonic anemometer. *Meteorologische Zeitschrift*, 18(2, Sp. Iss. SI):135–140.

Mann, J., Peña, A., Bingöl, F., Wagner, R., and Courtney, M. S. (2010). Lidar scanning of momentum flux in and above the surface layer. *Journal of Atmospheric and Oceanic Technology*, 27(6):792–806. DOI:10.1175/2010JTECHA1389.1.

Monin, A. S. and Yaglom, A. M. (1975). *Statistical Fluid Mechanics*, volume 2. MIT Press.

Nelder, J. A. and Mead, R. (1965). A simplex method for function minimization. *The computer Journal*, 7:308–313.

Peña, A., Gryning, S.-E., and Mann, J. (2010). On the length scale of the wind profile. *Quarterly Journal of the Royal Meteorological Society*, 136(653):2119–2131.

Peña, A., Hasager, C. B., Gryning, S.-E., Courtney, M., Antoniou, I., and Mikkelsen, T. (2009). Offshore wind profiling using light detection and ranging measurements. *Wind Energy*, 12(2):105–124.

Pichugina, Y. L., Banta, R. M., Kelly, N. D., Jonkman, B. J., Tucker, S. C., Newsom, R. K., and Brewer, W. A. (2008). Horizontal-velocity and variance measurements in the stable boundary layer using Doppler lidar: Sensitivity to averaging procedures. *Journal of Atmospheric and Oceanic Technology*, 25:1307–1327.

Rao, S. (2009). *Engineering Optimization: Theory and Practice*. John Wiley and Sons Inc., Hoboken, New Jersey, fourth edition.

Sathe, A., Mann, J., Gottschall, J., and Courtney, M. S. (2011). Can wind lidars measure turbulence? *Journal of Atmospheric and Oceanic Technology*, 28(7):853–868.

Sjöholm, M., Mikkelsen, T., Mann, J., Enevoldsen, K., and Courtney, M. (2009). Spatial averaging-effects on turbulence measured by a continuous-wave coherent lidar. *Meteorologische Zeitschrift*, 18(3, Sp. Iss. SI):281–287.

Smalikho, I., Kopp, F., and Rahm, S. (2005). Measurement of atmospheric turbulence by 2-μm Doppler lidar. *Journal of Atmospheric and Oceanic Technology*, 22(11):1733–1747.

Smith, D. A., Harris, M., Coffey, A. S., Mikkelsen, T., Jørgensen, H. E., Mann, J., and Danielian, R. (2006). Wind lidar evaluation at the Danish wind test site in Høvsøre. *Wind Energy*, 9:87–93.

Sonnenschein, C. M. and Horrigan, F. A. (1971). Signal-to-noise relationships for coaxial systems that heterodyne backscatter from atmosphere. *Applied optics*, 10(7):1600.

Storn, R. and Price, K. (1997). Differential evolution a simple and efficient heuristic for global optimization over continuous spaces. *Journal of Global Optimization*, 11(4):341–359.

Wagner, R., Mikkelsen, T., and Courtney, M. (2009). Investigation of turbulence measurements with a continuous wave, conically scanning lidar. Technical Report Risø-R-1682(EN), Risø DTU.

Wilson, D. A. (1970). Doppler radar studies of boundary layer wind profiles and turbulence in snow conditions. In *Proc.* 14th *Conf. on Radar Meteorology*, pages 191–196.

Wyngaard, J. C. (1968). Measurement of small-scale turbulence structure with hot wires. *Journal of Scientific Instruments*, 1:1105–1108.

Chapter 8

Conclusions and future work

8.1 Conclusions

Broadly speaking the original goal at the start of this PhD project was to somehow make use of the measurements in analyzing wind turbine loads at an offshore site. If we consider what has been achieved, there has been some digression, mainly due to the opportunities that have been provided to perform research in other interesting topics. In particular research has been carried out in wind profiles, turbulence, wind turbine loads, and measurement of turbulence using wind lidars. The conclusions are based on the answers to the research questions that were posed in section 1.1. At first an overall conclusion is formulated. Then each question is tackled individually and conclusions are drawn accordingly.

8.1.1 Overall conclusions

It is important to quantify the wind conditions as accurately as possible from the perspective of wind turbine loads. This is clearly evident when we compare the loads obtained using the IEC [2005a] defined wind conditions and those obtained using site-specific wind conditions. Especially, the quantification of the wind profiles and turbulence should be carried out as accurately as possible since they have a direct influence on the fatigue loads. A more physical logarithmic wind shear with a diabatic correction term that is valid for the entire boundary layer should be used instead of the power law with a shear exponent as suggested in the IEC [2005a] standard. The description of the Mann [1994] model parameters in quantifying turbulence should also be site-specific. The IEC [2005a] standard assumes that L_M and Γ do not change with the mean wind speed, whereas observations at Høvsøre indicate the contrary. The $\alpha\epsilon^{2/3}$ parameter according to the IEC [2005a] standard is about 4.5 to 1.5 times larger than that observed at Høvsøre. This causes the level of turbulence to increase significantly when the IEC [2005a] standard is used as compared to the site-specific turbulence. The use of diabatic wind conditions as input in load calculations is important for the tower and rotor loads. However, more investigations are necessary to consolidate the understanding.

The use of site-specific wind conditions in load calculations require measurements. Remote-sensing devices like lidars have the potential to measure turbulence, and in the past have already been proven to measure the mean wind profiles with sufficient accuracy. Using the VAD scanning method, lidars cannot measure turbulence precisely. It is unwise to use a simple transfer function in order to correct for the systematic errors in the turbulence statistics measured by lidars, primarily because the distribution of the energy with respect to the wavenumbers is completely different in comparison to what is actually observed in the nature. New methods are required to measure turbulence using lidars, and the six-beam approach has the potential to reduce the systematic errors in the measurements. If lidars are demonstrated to measure turbulence precisely in comparison to the sonic anemometers then it has the potential to displace traditional meteorological mast anemometry, and potentially change the current methods of wind turbine design.

8.1.2 Specific conclusions

How are diabatic wind profiles characterized?

The diabatic wind profiles are characterized using two different wind profile models. Under stable conditions the model that is strictly valid for the surface layer over-predicts the wind shear significantly (particularly at greater heights) as compared to the Gryning et al. [2007] model that is valid for the entire boundary layer. This because for the surface-layer wind profile model the length scale increases infinitely with height. This is a reasonable assumption in the surface layer but is certainly not true for the entire boundary layer [Blackadar, 1962]. The boundary-layer height parameter z_i introduced in the Gryning et al. [2007] model restricts the growth of the length scale beyond the surface layer, which results in achieving good agreement between the model and the measurements at all heights. For unstable conditions both models agree well with the measurements, also observed in an independent study by Peña et al. [2008]. Under unstable conditions z_i is much larger than that under stable conditions, and consequently the surface layer also extends to greater heights. Hence, surface-layer similarity theory is more applicable under these conditions resulting in good agreement of the models and the measurements. Thus we do not need to include z_i parameter in the models under unstable conditions, also observed independently by Peña et al. [2008].

Are wind turbine loads influenced by atmospheric stability?

When diabatic wind profiles are used under steady wind conditions in the load calculations, fatigue loads at the blade root are increased significantly as compared to those obtained by assuming neutral conditions only. This is a result of increased wind shear under stable conditions, and has a direct influence on fatigue damage. Atmospheric stability distribution thus becomes very important. A stable site will induce more loads as compared to unstable sites.

When diabatic wind conditions are used in load calculations the tower loads are mainly influenced by diabatic turbulence, whereas the rotor loads are influenced by diabatic wind profiles. The blade loads are influenced by both, diabatic wind profile and turbulence, that leads to averaging of the loads, i.e. the calculated loads using the diabatic wind conditions are approximately the same as those obtained assuming neutral wind conditions. The distribution of atmospheric stability is quite important in calculating fatigue loads. For a very stable site the calculated tower loads using diabatic wind conditions will decrease significantly, whereas those for the rotor loads will increase. The choice of a wind profile model will also influence the rotor loads significantly. E.g. a surface-layer wind profile model will predict a larger wind shear under stable conditions as compared to the boundary-layer wind profile model, and hence predict larger rotor loads as compared to those obtained using the boundary-layer wind profile.

The IEC [2005a] standard is extremely conservative for calculating the wind turbine loads under normal power production cases. They predict loads which are up to 95% larger than those obtained using diabatic input wind conditions.

Can wind lidars measure turbulence?

With the current measurement configuration that uses the VAD scanning technique to extract wind field components, lidars cannot measure turbulence precisely. Two mechanisms contribute to imprecise turbulence measurements by lidars. One is the averaging effect of turbulence due to a large sample volume in which lidars measure wind speeds. The second is the contribution of all components of the Reynolds stress tensor in the measurement of turbulence that arises due to combining different lidar beams. The systematic errors behave differently for continuous-wave and pulsed lidars. For pulsed lidars the errors are dependent on wind direction and averaging effect reduces with height due to constant length of the sample volume, whereas for a continuous-wave lidar the averaging effect increases with height since the length of the sample volume increases quadratically with height. The systematic errors due to the averaging effect are also influenced by atmospheric stability. Under stable conditons turbulence length scales are smaller. This results in larger volume averaging in comparison to unstable conditions.

How do pulsed wind lidars measure turbulence spectra?

Approximately in the inertial sub-range there is a complete attenuation of turbulent energy, primarily because of the averaging effect in the large sample volume. Close to the inertial sub-range and low frequencies there is a redistribution of the turbulent energy. One of the reasons for this redistribution is the contribution of all components of the Reynolds stress tensor. It is clearly evident that even if the Reynolds stress tensor measured by lidars agrees quite well with that measured by sonics, at least for wind turbine applications it is not recommended to use lidars for turbulence measurements. This is because for wind turbines apart from the Reynolds stress tensor the distribution of energy at various frequencies is also quite important, and evidently the turbulence spectra measured by lidars does not correspond to that observed in the nature.

How would it be possible for wind lidars to measure turbulence?

In principle if we directly use the variances of radial velocity then we can eliminate the systematic errors due to cross-contamination by other components of the Reynolds stress tensor, which requires six lidar beams. The only systematic errors that remain are due to the averaging effect in the large sample volume.

8.2 Recommendations for future work

Several ideas have sprung up as result of working on this PhD project. Each idea is a potential research topic of its own. They are listed as follows:

1. Friction velocity u_* is an important parameter in many meteorological studies, particularly for wind profile and atmospheric turbulence. If we wish to model the wind profile that is valid in the entire boundary layer then we need an accurate estimate of u_*. Gryning et al. [2007] modelled the friction velocity that varied linearly with height, but non-linear expressions for u_* have also been suggested [Panofsky, 1973]. This will have significant influence on the wind profile models in the boundary layer. Thus more work is needed to model or measure u_* profile accurately in the boundary layer. Lidars can be used to measure u_* profiles.

2. Modelling the wind profile for modern wind turbines must include z_i, particularly under stable conditions [Gryning et al., 2007, Peña et al., 2008, Sathe et al., 2011a]. The best method to obtain z_i is to directly measure it but is quite difficult and expensive. If z_i is to be used in the wind profile models it is convenient if we have some model of z_i instead of having to measure it. There are lot of uncertainties in the modelling z_i, particularly under diabatic conditions [Seibert et al., 2000]. Much work is needed to have a robust model for estimating z_i.

3. The wind profile model by Gryning et al. [2007] uses the very uncertain resistance law constants A and B under diabatic conditions. In this PhD study A and B vary only with the stability parameters. Zilitinkevich and Esau [2005] observed that A and B are functions of stability parameters, baroclinicity and boundary layer height. More experimental work is needed to verify the findings.

4. In chapter 4 we performed load simulations to investigate the influence of atmospheric stability. As a next obvious step, comparison of the simulated and measured loads should be carried out.

5. A comparison of the load simulations under diabatic conditions should be made between onshore and offshore sites. It is well known that wind speeds at offshore sites are higher than at onshore sites. This affects the turbulent structure and consequently will have an influence on the loads.

6. The 6-beam approach as described in chapter 7 has in principle the potential to counter the challenges faced by the VAD technique. The theoretical results obtained in chapter 7 need to be verified using measurements. This requires

significant hardware changes to the existing lidar technology.

7. From Mann et al. [2009] it is observed that at small turbulence scales the radial velocity spectra measured by lidars coincide with that measured by a sonic anemometer. This means that at large turbulence scales the averaging effect due to lidar sampling volume and the influence of the contamination by the cross-components is negligible. There is thus a potential to fit a three-dimensional spectral tensor model, e.g. [Mann, 1994] to only the low frequency part and deduce the entire turbulent structure. We can thus make use of lidar measurements and turbulence spectral tensor models to measure turbulence.

8. The model of the turbulence spectra as measured by a pulsed wind lidar in chapter 6 is in principle only valid when the mean wind direction is aligned with the measurement beams. As an obvious next step this model should be extended to arbitrary wind directions.

9. The model in chapter 6 was derived with a view to modelling gusts as measured by lidars, since the gust factor is a function of turbulence spectral moments. A detailed gust modelling should be carried out using the model developed in chapter 6 in order to understand theoretically how lidars measure gusts.

10. In chapters 5 – 7, for theoretically modelling the turbulence as measured by lidars we used the Mann [1994] model under all atmospheric stabilities. However, the Mann [1994] model is strictly valid only under neutral conditions. Barring the model by Hanazaki and Hunt [2004], which is valid only under stable conditions there is no diabatic spectral tensor model of turbulence. A diabatic three-dimensional turbulent structure model is thus required.

Appendix A

Appendices

A.1 Uncertainty analysis of Obukhov length

L is estimated using the $\mathrm{Ri_b}$ method Grachev and Fairall [1996],

$$L = \begin{cases} \frac{z}{10\mathrm{Ri_b}} & \text{for } L < 0; \\ \\ \frac{z(1-5\mathrm{Ri_b})}{10\mathrm{Ri_b}} & \text{for } L > 0. \end{cases} \tag{A.1}$$

Mathematically, $\mathrm{Ri_b}$ is given as,

$$\mathrm{Ri_b} = \frac{-gz(T_{vsea} - \theta_v)}{\theta_v u^2} \tag{A.2}$$

where T_{vsea} is the virtual temperature at the sea surface. θ_v is defined as,

$$\theta_v = T_v \left(\frac{P_0}{P}\right)^{\left(\frac{R_{air}}{C_p}\right)} \tag{A.3}$$

where P is the air pressure at z, T_v is the virtual temperature of air at z, P_0 is the reference air pressure, R_{air} is the gas constant for dry air, and C_p is the specific heat at constant pressure. T_v is defined as,

$$T_v = \frac{T}{1 - \frac{esRH}{P}(1 - \epsilon_a)} \tag{A.4}$$

where RH and e_s are the relative humidity and saturation vapour pressure at z, and ϵ_a is the ratio of the gas constant of dry air to moist air. T_{vsea} is obtained by substituting T by SST, RH by RH_{sea}, e_s by e_{ssea}, and P by P_0 in Eq. A.4. e_s is estimated following Flatau et al. [1992],

$$\begin{aligned} e_s = {} & 6.1117675 + 0.4439860 62T + 1.43053301 \times 10^{-2}T^2 \\ & + 2.65027242 \times 10^{-4}T^3 + 3.02246994 \times 10^{-6}T^4 \\ & + 2.03886313 \times 10^{-8}T^5 + 6.38780966 \times 10^{-11}T^6 \end{aligned} \tag{A.5}$$

e_{ssea} is estimated by substituting T by SST in Eq. A.5. P is defined as,

$$P = P_0 \exp\left(\frac{-Mgz}{RT}\right) \tag{A.6}$$

where M is the molar mass of air and R is the universal gas constant. Table A.1 gives the values of the constants that are used in this analysis. From Eqs. A.1–A.6

Table A.1: *Constants used in the uncertainty analysis*

$g = 9.81$ m/s^2
$Cp = 1005$ J/kg-K
$\epsilon_a = 0.622$
$z = 21$ m
$P_0 = 1.01325 \times 10^5$ N/m^2
$M = 0.02896$ kg/mol
$R = 8.314$ J/mol-K
$R_{air} = 287$ J/kg-K
$RH_{sea} = 100\%$

and table A.1, it is clear that

$$L = f(T, T_{sea}, RH, u) \tag{A.7}$$

where $f()$ denotes a function. Since L is a function of multiple variables, using the law of propagation of uncertainty ISO [1995],

$$u_c(L) = \sum_{i=1}^{N} \left(\frac{\partial L}{\partial X_i}\right)^2 u_i(X_i)^2 + \sum_{i=1}^{N-1} \sum_{j=i+1}^{N} \frac{\partial L}{\partial X_i} \frac{\partial L}{\partial X_j} \overline{X_i X_j} \tag{A.8}$$

where $u_c(L)$ is the combined uncertainty in the estimation of L, N are the number of variables (equal to 4 in this analysis), X_i are the variables (T, T_{sea}, RH, u), $\partial/\partial X_i$ denotes the partial derivative with respect to X_i, $u_i(X_i)$ is the standard individual uncertainty of X_i and $\overline{X_i X_j}$ is the covariance of X_i and X_j. Since the high frequency raw measurements of X_i are unavailable, we assume that they are uncorrelated, and hence, the second term in Eq. A.8 vanishes. Thus,

$$u_c(L) = \sum_{i=1}^{N} \left(\frac{\partial L}{\partial X_i}\right)^2 u_i(X_i)^2 \tag{A.9}$$

Since 10-min mean measurements are used to estimate L, the partial derivatives are evaluated for each 10–min observation. Eq. A.1 is used to obtain partial derivatives for unstable and stable condition. $u_i(X_i)$ is obtained using a Type B evaluation, where the use of calibration reports is made. Table A.2 gives the standard uncertainties at OWEZ and Horns Rev,

Fig. A.1a and A.1b (top figure) show the combined uncertainty in the estimation of L. It is observed that $u_c(L)$ increases rapidly (top figure) as the difference in θ_v and T_{vsea} is reduced (middle figure), in accordance with Vincent et al. [2010]. Thus,

Table A.2: *Standard individual uncertainty at OWEZ and Horns Rev*

	OWEZ	Horns Rev
$u_1(T)$ [°C]	0.1	0.354
$u_2(T_{sea})$ [°C]	0.1	0.354
$u_3(RH)$ [%]	3.5	1
$u_4(u)$ [m/s]	0.1	0.076

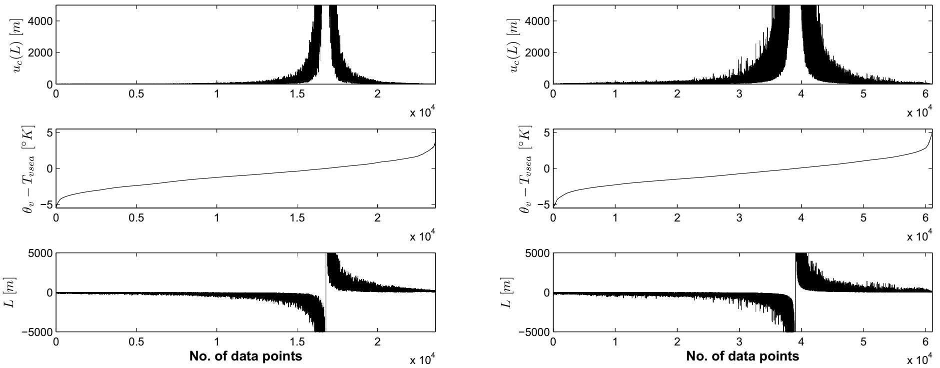

(a) *OWEZ* **(b)** *Horns Rev*

Figure A.1: *Combined uncertainty in the estimation of L*

L is most uncertain in the neutral conditions, whereas as the atmosphere becomes more stable or unstable the uncertainty in L is reduced significantly (top and bottom figures). Also, the spread in $u_c(L)$ at Horns Rev is greater than at OWEZ, likely because the uncertainty in temperature measurements is greater at Horns Rev than at OWEZ (see table A.2).

A.2 Derivation of the radial velocity coefficients in a CW lidar

The coefficients A, B and C are estimated using the least squares method. The residual for the radial velocity is given as,

$$r = \tilde{v}_r(\theta) - (A + B\ \cos\theta + C\ \sin\theta) \tag{A.10}$$

In order to estimate A, B and C, sum of the squared residuals should be minimum, and hence, derivatives are taken with respect to the coefficients and equated to zero.

Thus,

$$\frac{\partial r}{\partial A} = \sum_{\theta=0}^{2\pi} -2[\tilde{v}_r(\theta) - (A + B\ \cos\theta + C\ \sin\theta)] = 0 \tag{A.11}$$

$$\frac{\partial r}{\partial B} = \sum_{\theta=0}^{2\pi} -2\cos\theta[\tilde{v}_r(\theta) - (A + B\ \cos\theta + C\ \sin\theta)] = 0 \tag{A.12}$$

$$\frac{\partial r}{\partial C} = \sum_{\theta=0}^{2\pi} -2\sin\theta[\tilde{v}_r(\theta) - (A + B\ \cos\theta + C\ \sin\theta)] = 0 \tag{A.13}$$

Rearranging the above equations,

$$\sum_{\theta=0}^{2\pi} \tilde{v}_r(\theta) = A\sum_{\theta=0}^{2\pi} + B\sum_{\theta=0}^{2\pi}\cos\theta + C\sum_{\theta=0}^{2\pi}\sin\theta \tag{A.14}$$

$$\sum_{\theta=0}^{2\pi} \tilde{v}_r(\theta)\cos\theta = A\sum_{\theta=0}^{2\pi}\cos\theta + B\sum_{\theta=0}^{2\pi}\cos^2\theta + C\sum_{\theta=0}^{2\pi}\sin\theta\cos\theta \tag{A.15}$$

$$\sum_{\theta=0}^{2\pi} \tilde{v}_r(\theta)\sin\theta = A\sum_{\theta=0}^{2\pi}\sin\theta + B\sum_{\theta=0}^{2\pi}\cos\theta\sin\theta + C\sum_{\theta=0}^{2\pi}\sin^2\theta \tag{A.16}$$

Multiplying both sides by $d\theta$ and replacing the summation by integrals the above equations can be written as,

$$\int_0^{2\pi} \tilde{v}_r(\theta)\ d\theta = A\int_0^{2\pi} d\theta + B\int_0^{2\pi}\cos\theta\ d\theta + C\int_0^{2\pi}\sin\theta\ d\theta \tag{A.17}$$

$$\begin{aligned}\int_0^{2\pi} \tilde{v}_r(\theta)\cos\theta\ d\theta = A\int_0^{2\pi}\cos\theta\ d\theta + B\int_0^{2\pi}\cos^2\theta\ d\theta \\ + C\int_0^{2\pi}\sin\theta\cos\theta\ d\theta\end{aligned} \tag{A.18}$$

$$\begin{aligned}\int_0^{2\pi} \tilde{v}_r(\theta)\sin\theta\ d\theta = A\int_0^{2\pi}\sin\theta\ d\theta + B\int_0^{2\pi}\cos\theta\sin\theta\ d\theta \\ + C\int_0^{2\pi}\sin^2\theta\ d\theta\end{aligned} \tag{A.19}$$

To estimate the coefficients the integrals are estimated; $\int_0^{2\pi}\cos^2\theta\ d\theta = \pi$, $\int_0^{2\pi}\sin\theta\cos\theta\ d\theta = 0$, $\int_0^{2\pi}\cos\theta\ d\theta = 0$, $\int_0^{2\pi}\sin^2\theta\ d\theta = \pi$, $\int_0^{2\pi}\sin\theta\ d\theta = 0$ and $\int_0^{2\pi} d\theta = 2\pi$. Substituting the integrals in the above equation we get,

$$A = \frac{1}{2\pi}\int_0^{2\pi}\tilde{v}_r(\theta)\ d\theta \tag{A.20}$$

$$B = \frac{1}{\pi}\int_0^{2\pi}\tilde{v}_r(\theta)\ \cos\theta\ d\theta \tag{A.21}$$

$$C = \frac{1}{\pi}\int_0^{2\pi}\tilde{v}_r(\theta)\ \sin\theta\ d\theta \tag{A.22}$$

Bibliography

A K. Blackadar. The vertical distribution of wind and turbulent exchange in a neutral atmosphere. *Journal of Geophysical Research*, 67(8):3095–3102, 1962. doi: {10.1029/JZ067i008p03095}.

T. Burton, D. Sharpe, N. Jenkins, and E. Bossanyi. *Wind Energy Handbook*. John Wiley and Sons, LTD, 2001.

M. Courtney, R. Wagner, and P. Lindelow. Testing and comparison of lidars for profile and turbulence measurements in wind energy. In J. Mann et al., editor, 14^{th} *International Symposium for the Advancement of Boudary Layer Remote Sensing*, volume 1 of *IOP Conference Series Earth and Environmental Science*, page 012021. IOP Publishing LTD., 2008. doi: 10.1088/1755-1315/1/1/012021.

A G. Davenport. The spectrum of horizntal gustiness near the ground in high winds. *Quarterly Journal of the Royal Meteorological Society*, 87:194–211, 1961.

W L. Eberhard, R E. Cupp, and K R. Healy. Doppler lidar measurements of profiles of turbulence and momentum flux. *Journal of Atmospheric and Oceanic Technology*, 6:809–819, 1989. doi: 10.1175/1520-0426(1989)006$⟨$0809:DLMOPO$⟩$2.0.CO;2.

P J. Flatau, R L. Walko, and W R. Cotton. Polynomial fits to saturation vapour pressure. *Journal of Applied Meteorology*, 31:1507–1513, 1992.

A A. Grachev and C W. Fairall. Dependence of the Monin-Obukhov stability parameter on the bulk Richardson number over the ocean. *Journal of Applied Meteorology*, 36:406–414, 1996.

S-E. Gryning, E. Batchvarova, B. Brümmer, H. Jørgensen, and S. Larsen. On the extension of the wind profile over homogeneous terrain beyond the surface layer. *Boundary-Layer Meteorology*, 124(2):251–268, 2007. doi: 10.1007/s10546-007-9166-9.

H. Hanazaki and J C R. Hunt. Structure of unsteady stably stratified turbulence with mean shear. *Journal of Fluid Mechanics*, 507:1–42, 2004. doi: 10.1017/S0022112004007888.

IEC. IEC 61400-1. Wind turbines – Part 1: Design Requirements. 2005a.

IEC. IEC 61400-3. Offshore wind turbines-part 1: Design Requirements. 2005b.

ISO. Guide to the Expression of Uncertainty in Measurement. Technical report, International Organisation for Standardization, 1995.

J C. Kaimal, J C. Wyngaard, Y. Izumi, and O R. Coté. Spectral characteristics of surface-layer turbulence. *Quarterly Journal of the Royal Meteorological Society*, 98 (417):563–589, 1972. doi: 10.1002/qj.49709841707.

H J. Kouwenhoven. *User manual data files meteorological mast NoordzeeWind*. NoordzeeWind, 2.0 edition, October 2007.

J. Mann. The spatial structure of neutral atmospheric surface-layer turbulence. *Journal of Fluid Mechanics*, 273:141–168, 1994. ISSN 0022-1120. doi: 10.1017/S0022112094001886.

J. Mann, J. Cariou, M. Courtney, R. Parmentier, T. Mikkelsen, R. Wagner, P. Lindelow, M. Sjöholm, and K. Enevoldsen. Comparison of 3D turbulence measurements using three staring wind lidars and a sonic anemometer. *Meteorologische Zeitschrift*, 18(2, Sp. Iss. SI):135–140, 2009. doi: 10.1127/0941-2948/2009/0370.

J. Mann, A. Peña, F. Bingöl, R. Wagner, and M S. Courtney. Lidar scanning of momentum flux in and above the surface layer. *Journal of Atmospheric and Oceanic Technology*, 27(6):792–806, 2010. doi: 10.1175/2010JTECHA1389.1.

A S. Monin and A M. Obukhov. Basic laws of turbulent mixing in the atmosphere near the ground. *Tr. Akad. Nauk. SSR, Geofiz. Inst.*, 151:163–187, 1954.

Hans A. Panofsky. *Workshop on Micrometeorology*, chapter Tower Micrometeorology, pages 151–176. American Meteorological Society, 1973.

A. Peña, S-E. Gryning, and C B. Hasager. Measurement and modelling of the wind speed profile in the marine atmospheric boundary layer. *Boundary-Layer Meteorology*, 129(3):479–495, 2008. doi: 10.1007/s10546-008-9323-9.

A. Peña, C B. Hasager, S-E. Gryning, M. Courtney, I. Antoniou, and T. Mikkelsen. Offshore wind profiling using light detection and ranging measurements. *Wind Energy*, 12(2):105–124, 2009. doi: 10.1002/we.283.

L. Prandtl. Meteorologische Anwendung der Strömungslehre. *Beiträge zur Physik der Atmosphäre*, 19:188–202, 1932.

S O. Rice. Mathematical analysis of random noise. *Bell System Tech. J.*, 23(3): 282–332, 1944.

S O. Rice. Mathematical analysis of random noise. *Bell System Tech. J.*, 24(1): 46–156, 1945.

A. Sathe and W. Bierbooms. The influence of different wind profiles due to varying atmospheric stability on the fatigue life of wind turbines. In M O L. Hansen and K S. Hansen, editors, *The Science of Making Torque from Wind*, volume 75 of *Journal of Physics: Conference Series*, pages 12056–12062, 2007. doi: 10.1088/1742-6596/75/1/012056.

A. Sathe and J. Mann. Measurement of turbulence spectra using scanning pulsed wind lidars. 2011. Submitted to Journal of Geophysical Research.

A. Sathe, S-E. Gryning, and A. Peña. Comparison of the atmospheric stability and wind profiles at two wind farm sites over a long marine fetch in the North Sea. *Wind Energy*, 14(6):767–780, 2011a. doi: 10.1002/we.456.

A. Sathe, J. Mann, T. Barlas, and W. Bierbooms. Influence of atmospheric stability on wind turbine loads. 2011b. Submitted to Wind Energy.

A. Sathe, J. Mann, J. Gottschall, and M S. Courtney. Can wind lidars measure turbulence? *Journal of Atmospheric and Oceanic Technology*, 28(7):853–868, 2011c. doi: 10.1175/JTECH-D-10-05004.1.

A. Sathe, J. Mann, J. Gottschall, and M S. Courtney. Can the available wind lidars measure turbulence? In *ICWE13 Scientific Proceedings*, Amsterdam, The Netherlands, 11-15 July 2011d.

P. Seibert, F. Beyrich, S-E. Gryning, S. Joffre, A. Rasmussen, and P. Tercier. Review and intercomparison of operational methods for the determination of the mixing height. *Atmospheric Environment*, 34(7):1001–1027, 2000.

M. Sjöholm, T. Mikkelsen, J. Mann, K. Enevoldsen, and M. Courtney. Spatial averaging-effects on turbulence measured by a continuous-wave coherent lidar. *Meteorologische Zeitschrift*, 18(3, Sp. Iss. SI):281–287, 2009. doi: 10.1127/0941-2948/2009/0379.

D A. Smith, M. Harris, A S. Coffey, T. Mikkelsen, H E. Jørgensen, J. Mann, and R. Danielian. Wind lidar evaluation at the Danish wind test site in Høvsøre. *Wind Energy*, 9:87–93, 2006. doi: 10.1002/we.193.

C L. Vincent, P. Pinson, and G. Giebel. Wind fluctuations over the North Sea. *International Journal of Climatology*, 2010. doi: 10.1002/joc.2175.

T. von Kármán. Progress in the statistical theory of turbulence. In *Proceedings of National Academy of Sciences, USA*, volume 34, pages 530–539. California Institute of Technology, Pasadena, June 1948.

S S. Zilitinkevich and I N. Esau. Resistance and heat-transfer laws for stable and neutral planetary boundary layers: Old theory advanced and re-evaluated. *Quarterly Journal of the Royal Meteorological Society*, 131(609):1863–1892, 2005. doi: 10.1256/qj.04.143.

Curriculum-vitae

Ameya Sathe was born on 17^{th} June 1981 in Mumbai, India.

He completed his Bachelor of Engineering degree in Mechanical engineering from Mumbai University in 2002. He then competed in the GATE entrance examination in 2003 and secured admission for a Masters course in Hydrology at the Indian Institute of Technology, Roorkee, India. During his Masters he was awarded the DAAD-IIT scholarship to pursue his Masters thesis in University of Stuttgart, Germany. He finished Master of Technology from IIT Roorkee in 2005 with highest grades. He then worked at TATA consultancy services as assistant systems engineer until August 2006.

From October 2006, he began his PhD studies at Delft University of Technology, The Netherlands. During his PhD he closely collaborated with Risø DTU, Denmark, in the EU UPWIND project that concerned turbulence measurements using wind lidars. In October 2010 he ended his contract at TU Delft and started working at Risø DTU as a Research Assistant in the EU Safewind project. The goals of this project coincided very nicely with his PhD, where he continued working on lidar turbulence measurements. In November 2011, his research work culminated into a PhD thesis.